Loss Analysis of the Power Conversion Efficiency of Organic Bulk Heterojunction Solar Cells

Von der Fakultät für Mathematik und Naturwissenschaften der
Carl von Ossietzky Universität Oldenburg zur Erlangung des
Grades und Titels eines

Doktors der Naturwissenschaften
(Dr. rer. nat)
angenommene Dissertation von

Herrn **Pavel Schilinsky**

geboren am 28.05.1974
in Hamburg

`Schilinsky@ivopavel.de`

Gutachter: Prof. Dr. Vladimir Dyakonov
Zweitgutachter: Prof. Dr. Jürgen Parisi
Drittgutachter: Dr. habil. Christoph Brabec

Tag der Disputation: 11.3.2005

Contents

Abstract

Plastic solar cells have attracted enormous attention due to their potential in attributing to the energy production, being light weighted, flexible and produced in a cheap and environmentally friendly way. Especially the bulk-heterojunction solar cells, consisting of blends of conjugated polymers or of conjugated polymers and small molecules, are promising for this purpose.

In this thesis the power conversion efficiency and lifetime of bulk heterojunction solar cells are analyzed. The electrical and optical losses are investigated for one representative material combination using two models for the bulk heterojunction solar cells. These models allow the simulation of current-voltage characteristics of the solar cells. The deficiencies of the bulk heterojunction are analyzed and experiments for enhancing the efficiency are tested. The lifetime of bulk heterojunction solar cells is analyzed under working condition using elevated temperature for accelerating the degradation. The degradation mechanisms are analyzed using the two models.

Zusammenfassung

Plastiksolarzellen können zu einer sauberen Energieproduktion beitragen. Die Vision ist, daß Plasiksolarzellen die direkte Umwandlung von Sonnenlicht in Strom ermöglichen, wobei sie günstig und großflächig produziert werden können, ohne daß die Produktion selbst einen negativen Einfluß auf die Umwelt hätte. Besonders die Bulk Heterojunction Solarzellen, bei denen die aktive Schicht aus einer Mischung von konjugierten Poylmeren oder konjugierten Poylmeren mit organischen Molekülen besteht, versprechen schnell die Anforderungen für eine Kommerzialisierung zu erfüllen.

In dieser Arbeit werden zwei Kriterien der Kommerzialisierung untersucht: die Effizienz der Energieumwandlung und die Lebenszeit der Solarzellen. Für die Untersuchungen werden zwei Modelle benutzt, die die Simulation der Strom-Spannungs-Kennlinie erlauben und einen Zusammenhang zwischen Produktionsparametern und Effizenz herzustellen ermöglichen. Diese Zusammenhänge werden in verschiedenen Experimenten geprüft und Versuche unternommen, die Effizienz zu steigern. Die Lebenszeit der Bulk Heterojunction Solarzellen wird im Betrieb und bei erhöhter Temperatur ermittelt und die Mechanismen der Degradation werden mit den Modellen analysiert.

Chapter 1

Introduction to Plastic Solar Cells

1.1 Motivation

Solar cells may contribute to renewable and environmentally friendly energy conversion, without emission of the carbon dioxide. Since the discovery of solar cell in 1954 [1, 2], the photovoltaic research is focused on crystalline silicon solar cells, but so far the photovoltaic energy is limited to niche markets in comparison with other energy production techniques. The relative high cost of solar energy, converted by silicon solar cells, hinders a breakthrough of the photovoltaics, so far. Polymeric bulk heterojunction solar cells have attracted a lot of attention due to their high potential in cost reduction for large area elements. Conjugated polymer based solar cells (blends of conjugated polymers or of conjugated polymers and small molecules) have the potential to be significantly cheaper produced, than conventional semiconductor solar cells, while offering at the same time high environmental compatibility of the production process.

In contrast to classical bilayer junction devices, a bulk heterojunction device consists of a more or less homogeneous mixture of donor and acceptor materials. Most times, and also in this thesis, the donor is a conjugated polymer and the acceptor a fullerene.

In this thesis, the losses in the power conversion efficiency of organic bulk heterojunction solar cells are analyzed, for one representive semiconductor combination. Based on the findings of this loss analysis, improvements of the power conversion efficiency are suggested, tested and evaluated. Further, the operational stability of bulk heterojunction solar cells, which is one of the key parameters for solar cells, being decisive for the rentability, is investigated.

1.2 Outline of the Thesis

In the introduction, an overview on the working principle of organic bulk heterojunction solar cells will be given. In chapter 2 the materials used for the bulk heterojunction solar cell, the layout of the bulk heterojunction and the technologies used for the preparation of the bulk heterojunction are discussed. The measurement setups are introduced in chapter 3. In chapter 3.1 the processes and efficiencies of the photon to electron conversion and the power conversion are explained and discussed. The physics of these conversion efficiencies and parameters, influencing these efficiencies are discussed.

Two models, which allow the simulation of bulk heterojunction solar cells are discussed in chapter 4. The first model describes the bulk heterojunction solar cells on a microscopic level with the numeric solution of the transport, rate and Poisson equations. The second model is an extended equivalent circuit, where a standard 1-diode model is expanded for the particularities of the bulk heterojunction.

The efficiencies, deficiencies and potentials of the power conversion efficiency are analyzed in chapter 5.

In chapter 6 the degradation of an organic bulk heterojunction is analyzed. Possibilities for accelerating the degradation measurement are evaluated and the degradation mechanisms of the accelerated degradation are discussed.

1.3 Working Principle of Organic Bulk Heterojunction Solar Cells

In 1977 the conductivity and semi-conductivity of polymers were discovered [3]. This opened the research on organic molecules and polymers for classical semiconductor application like transistors, light emitting diodes and also solar cells. Solar cells were first designed as Schottky diodes, where the charge separation was due to the band bending on the metal-semiconductor interface. Here the light is absorbed in the polymer and an exciton is generated. An exciton is a bound electron hole pair. As the binding energy of excitons is high [4], the approximation of free carriers, as it is done for inorganic materials, is no longer valid for organic materials. The diffusion length of the excitons is measured to be about $10nm$ [5, 6, 7]. The exciton diffusion length is small in comparison to diffusion lengths of charge carriers in inorganic semiconductors ($\gtrsim 1\mu m$) or in comparison to layer thicknesses of polymer films usually used ($\gtrsim 0.1\mu m$). Only carriers generated close to the Schottky-junction are split into free carriers and contribute to the photogenerated current.

This limitation can be overcome with the bulk heterojunction. The concept of bulk heterojunctions is based on the photo induced charge transfer between a donor and an acceptor [8]. Most time the donor is a conjugated polymer. And as acceptor a C_{60} or a C_{60} - derivate is used. At the interface of the polymer and the C_{60} - derivate the photo induced charge transfer takes place in a fs time range [9]. The bulk heterojunction is an intimate mixture of the materials on the nm-scale (Figure 1.1). In the optimal case, this should guarantee an efficient charge separation and charge transport via percolation at the same time. The splitting of quasi Fermi levels due to the illumination produces the photo-voltage.

For a real bulk heterojunction deviations from the ideal case are observed. The morphology, the actual mixing of the two materials in the active layer has a large influence on the charge separation, the photogenerated current and on the total power conversion efficiency [10, 11, 12]. If the domains are too large, separation will not be efficient. If the domains are too small, recombination of free charges may be favored and charge transport hindered.

The photon to electron conversion consists of several succeeding single steps, which will be explained with a special look at the particularities of the organic bulk heterojunction. The photon to electron conversion can be described by almost the same processes for the organic bulk heterojunction solar cell, as for the classical pn-junction solar cell. These processes are photon absorption and charge generation, charge separation, charge transportation and

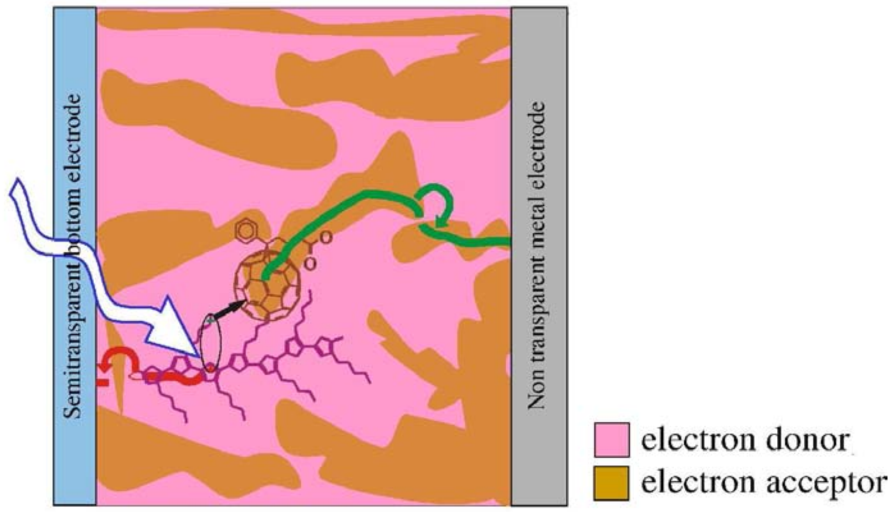

Figure 1.1: Scheme of the working principle of bulk heterojunction solar cells. The bulk heterojunction is depicted as a mixture of the two materials electron donor (pink) and electron acceptor (brown). The two materials are distributed randomly in the layer. The chemical structures of a typical representative are drawn. The bulk heterojunction is sandwiched between two electrodes. On the left is a semitransparent electrode and on the right is a non-transparent electrode. Through the semitransparent electrode the solar cell can be illuminated (white arrow). The light can be absorbed and charges are generated. At the interface the charges are separated. The separated charges are transported via conduction paths (represented by red and green lines) formed by the respective material phase to their respective electrodes.

extraction. The main difference to pn-junction solar cells is that the charge separation takes place all over the active layer and not just in a small fraction of the space charge region and therefore the carrier transport is governed by the majority carrier transport. The minority carrier diffusion length is about $10nm$.

The first step in the photon to electron conversion is the photon absorption. The bulk heterojunction is an intimate mixture of the electron donor with the electron acceptor, as depicted in Figure 1.1 and Figure 1.2. Both materials have different absorption spectra. The photons are absorbed according to the absorption spectrum on the respective material (Figure 1.2a). Here we consider the polymer a photoactive counterpart of the blend, however the same is valid for absorption on the electron acceptor. With the absorption of photons with an energy larger than the band gap E_g, excitons are formed. Photons with energy smaller than the band gap will not be absorbed and will not lead to a charge generation.

Excitons are bound electron-hole-pairs. For organic material this binding energy is relatively high [4, 13, 14] and therefore the approximation of free carriers, which is normally done for inorganic materials, can not be done for organic materials. As the binding energy is high, the exciton lifetime is short and therefore the exciton diffusion length, which is the distance the electron-hole-pairs can cover prior recombination, is in the order of $10nm$ [5,6,7]. The exciton diffusion length corresponds to the minority carrier diffusion length of inorganic semiconductors, which is usually several orders of magnitude larger than the exciton diffu-

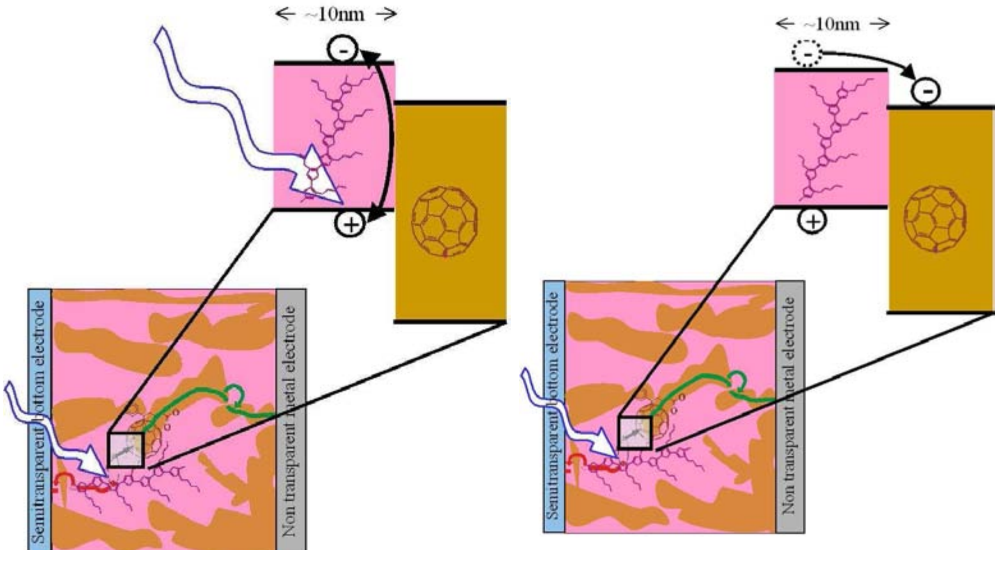

(a) charge generation

(b) charge seperation

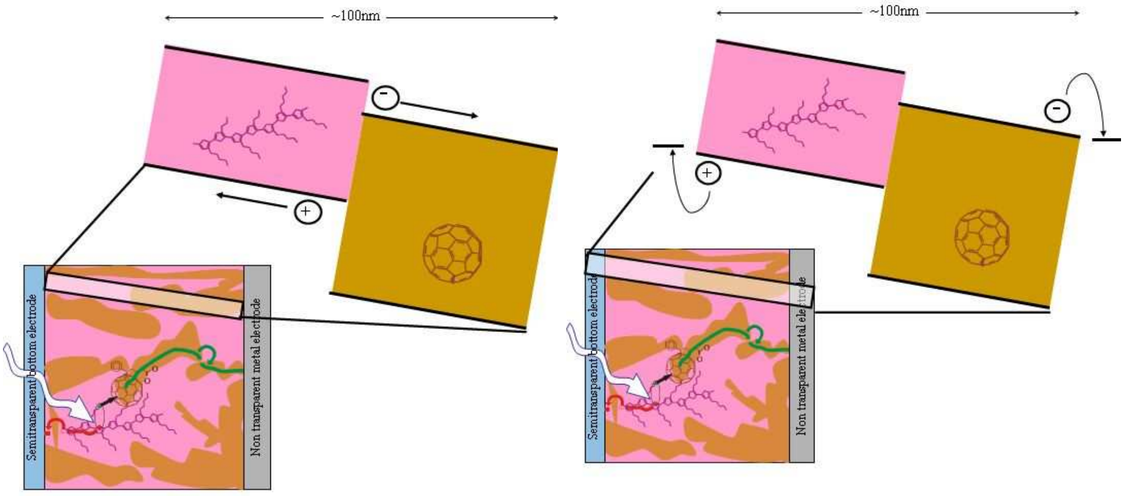

(c) charge transport

(d) charge collection

Figure 1.2: Scheme of processes of photon to electron conversion. Shown is the scheme of the bulk heterojunction, with the polymer (red) and the fullerene (brown) forming an interpenetrating network. For each step an enlargement to the respective process with the band diagram of the donor and acceptor material is shown. (a) Photons are absorbed by the polymer, forming an exciton. (b) The exciton is split at the interface between the donor and acceptor. The interface has to be reached within the exciton diffusion length, which is typical in the order of some tens of nm. (c) The separated charges are transported to the respective electrodes. The field is assumed as the driving force. The transport is along the interpenetrating network from one molecule to the other via a hopping process. (d) The charges are collected on the electrodes and are fed into the outer circuit.

sion length of organic semiconductors. For an efficient charge separation the pn-interface has to be reached within the exciton diffusion length by the excitons and the interface has to be distributed all over the active layer, like in the bulk heterojunction. On this interface the light induced charge transfer takes place (Figure 1.2b) [8] and the electron is transfered from the polymer to the electron acceptor. This charge separation is due to an energetic difference of the LUMO (Lowest Unoccupied Molecular Orbit or π^* orbital) levels of the polymer and the electron acceptor, respectively, and is a fast process [9]. With this step the exciton is separated into a free hole on the polymer and a free electron on the electron acceptor. These charges are now majority charge carriers with a relatively long lifetime [15, 16].

The possibility for recombination is lowered, but not excluded for the separated charges. The charge transport, as shown in figure 1.2(c), is in competition with recombination of charge carriers. On the boundaries between the p-type and n-type semiconductor the charges may encounter an opposite charged carrier and recombine with this carrier. This is called direct recombination, second order recombination or bimolecular recombination. The rate of this recombination is proportional to the carrier density of electrons and holes and therefore quadratic with the total carrier density and therefore quadratic with the illumination intensity [17]. Charges may get trapped and then recombine with the opposite carrier of a generated electron-hole-pair. The rate of this trap assisted recombination is proportional to the carrier density, which is proportional to the illumination intensity [18, 19]. The charge transport is field driven (as discussed in chapter 4.1) and the relevant transport parameters are the carrier mobility μ, carrier lifetime τ and internal electric field E. The mobility is a measure for the speed of the carriers in the electric field. The lifetime is the average time the charge carriers survive prior recombination and therefore the inversion of the recombination rate, normed to the carrier density. The internal field E is the sum of the applied field and the internal field E_{bi} due to the internal built-in voltage V_{bi} or flat-band-voltage V_{FB}.

On the contacts the carriers are collected. Ideally the contact should be ohmic for one material and form an energetic barrier to the other material. At the same time both materials should have one ohmic contact and one blocking contact. If a contact builds a barrier to both materials, the internal field will be reduced from V_{bi} to the flat-band voltage V_{FB}. Surface recombination may also take place, which would lower the number of extracted carriers.

The total photon to electron conversion efficiency, also called the external quantum efficiency (EQE), is the product of the single efficiencies for photon absorption (exciton generation) $\eta_{absorption}$, generation of free charge carriers (exciton splitting) $\eta_{generation}$, charge transport and collection $\eta_{transport}$ (equation (1.1)).

$$EQE = \eta_{absorption} \cdot \eta_{generation} \cdot \eta_{transport} \tag{1.1}$$

The origin of the open circuit voltage, which is the voltage of the solar cell, when no current flows, is a matter of controversial discussions. The upper limit of the open circuit voltage is the difference of the conduction band edge of the acceptor to the valence band edge (also called HOMO: Highest Occupied Molecular Orbit or π orbital) of the donor (Figure 1.3 a). The quasi-Fermi levels can split up to these bands and determine the open circuit voltage. Limitation may arise due to the contacts. In the model of a metal-insulator-metal (MIM) - diode [20], the work functions of the electrodes are limiting the open circuit voltage (Figure 1.3 b). Alternatively, the open circuit voltage is given by the difference of the LUMO of the C_{60} - derivative and the work function of the semitransparent electrode (Figure 1.3 c). This takes into account, that the fullerene pins the Fermi level of the metal. If the

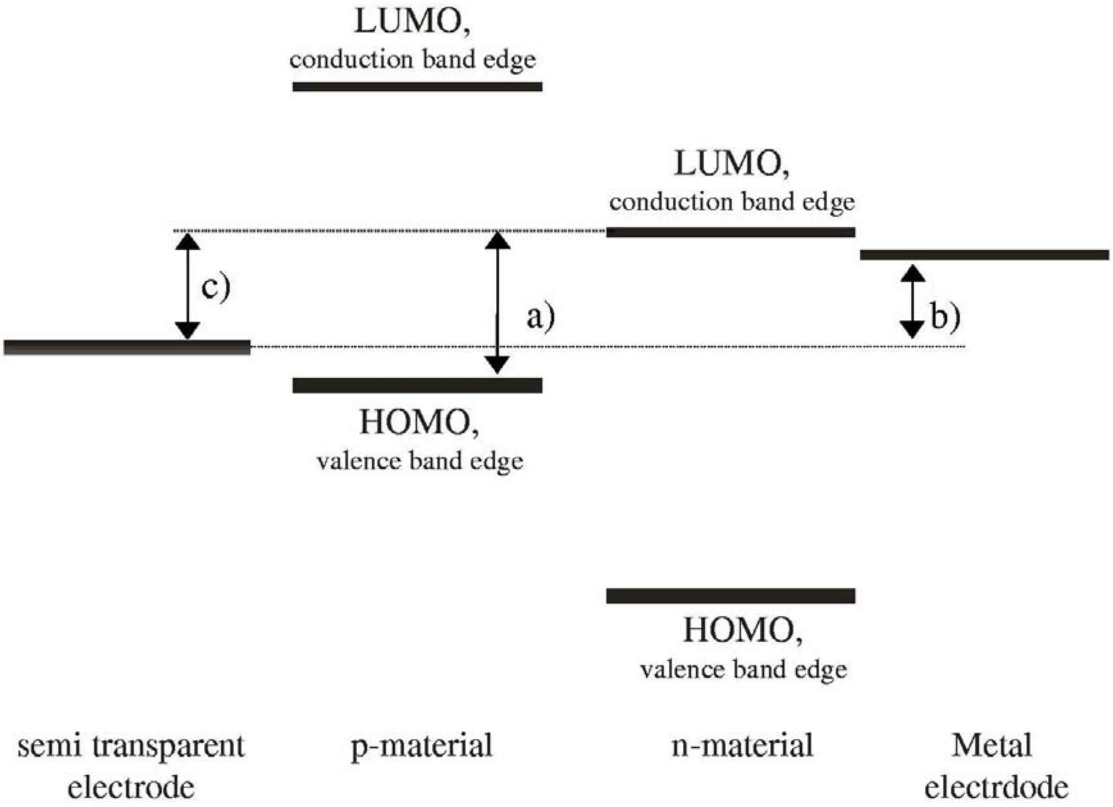

Figure 1.3: Energy band scheme of a bulk heterojunction solar cell. The limitations for the open circuit voltage, as discussed in the text are depicted with a), b) and c).

valence band of the p-material is above the work function of the semitransparent electrode the open circuit voltage may be reduced to the difference of the conduction band edge of the C_{60} - derivative to the valence band edge of the p-material [21,22,23]. Another model takes into account the morphology of the bulk heterojunction [24].

Chapter 2

Fabrication of Bulk Heterojunction Solar Cells

In this chapter I will discuss the layout of organic bulk heterojunction solar cells. The materials, processing as well as the function of the single layers, the solar cell is made of, are discussed. An overview of the variations in the sample fabrication, used for the experiments in this thesis, is given.

2.1 Layout of Bulk Heterojunction Solar Cells

The schematic layout of a bulk heterojunction solar cell is shown in Figure 2.1. The active layer, the bulk heterojunction itself, is sandwiched between the two electrodes.

The bulk heterojunction is a homogeneous mixture of the donor and acceptor. One material is a p-type semiconductor the other one is a n-type semiconductor. The materials typically form a morphology with phase separation in the nm-scale. This leads to an increase of the interface area between the p- and n-type semiconductor. At the same time the bulk heterojunction should allow the percolation of both materials from anywhere in the bulk to their respective electrode. The morphology has a large influence on the solar cell performance [10, 24, 12] and will be discussed later in this thesis (chapter 4 and 5).

For the substrate glass is used. On the glass substrates the transparent electrode indium-tin-oxide (ITO) and an interfacial layer of poly(ethylene dioxythiophene) doped with polystyrene sulphonic acid (PEDOT:PSS) are deposited. This electrode is the high work function electrode for the collection of holes. The second contact is an evaporated metal layer, which is typically a low work function electrode for the electron collection. The bulk heterojunction solar cells are illuminated through the ITO contact.

2.2 Materials

In this section an overview of the materials used is given. First the p-type and n-type semiconductors are discussed in terms of electrical and optical properties. Then the electrodes and the interface layer are discussed.

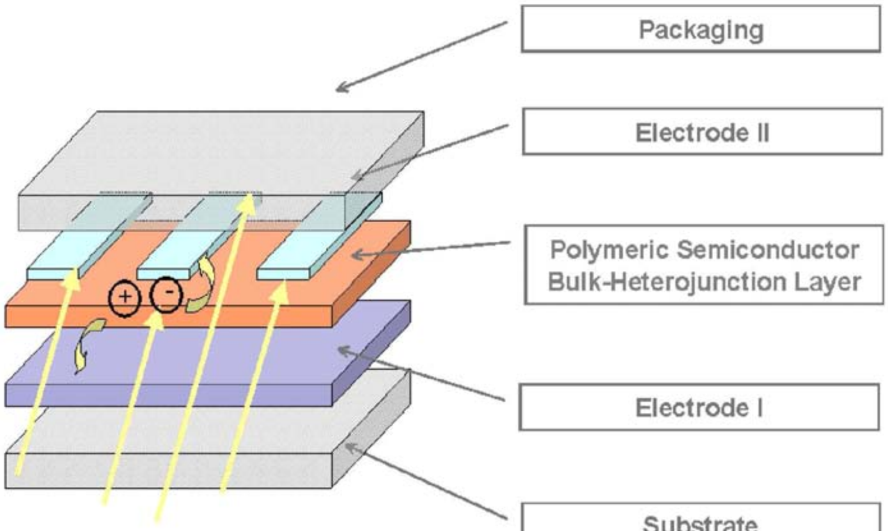

Figure 2.1: Layout of a bulk heterojunction solar cell. The active layer is sandwiched between the semi transparent bottom electrode, consisting of the glass substrate, ITO electrode and PEDOT interface layer and the top metal electrode.

2.2.1 The Hole Transporter

Polymeric semiconductors are usually hole conductors. In this thesis poly alkyl thiophene (PAT) is used as p-type semiconductor and electron donor. The chemical structure of PAT is given in Figure 2.2, where the alkyl group is hexyl ($poly3\,hexyl\,thiophene$ or P3HT). For pure films of P3HT a value of the hole mobility in the range of $\mu_p = 0.2$ to $10^{-3} cm^2V^{-1}s^{-1}$ [29, 30] was measured. The absorption of P3HT is shown in Figure 2.3. The band gap is about $1.9eV$ and the Fermi level lies in the middle of the gap [31]. The valence band edge is about $4.9..5.2eV$ below the vacuum level (Figure 2.2) [25, 26, 27]. The conduction band edge is at about $2.9..3.3eV$ below the vacuum level [25, 26, 27]. The value for the HOMO and LUMO energies are calculated either electrochemically or via the Fermi level and band gap determination [27] or relative to the work function of a metal [25].

2.2.2 The Electron Transporter

As electron transporting material, the fullerene [6,6] - phenyl C_{61} - butyric acid methyl ester (PCBM) is used. The chemical structure and the energy diagram are given in Figure 2.4. The HOMO is about $6.1..6.8eV$ [26,32,33] below the vacuum level and the LUMO is about $3.7..4.1eV$ [26, 32, 33] below the vacuum level. The values for $PCBM$ and C_{60} are often supposed to be the same [34, 20]. Variations in the literature values of the HOMO and LUMO arise due to the different measurement methods. For pure films of PCBM a value of the electron mobility in the range of $10^{-3}cm^2V^{-1}s^{-1}$ [35] was measured. The absorption spectrum is shown in Figure 2.3.

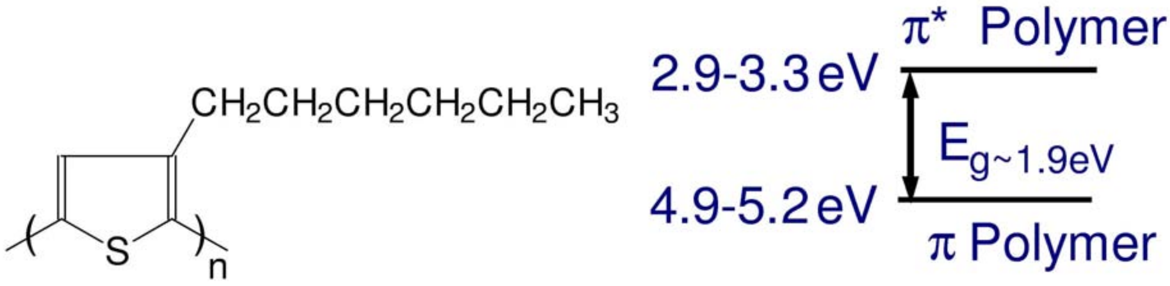

(a)

(b)

Figure 2.2: (a) Chemical structure of poly3hexyl thiophene (P3HT) and (b) the energy scheme of P3HT. The values for the HOMO and LUMO change for different measurements. The value for the HOMO level varies from $4.9eV$ to $5.2eV$ [25, 26, 27, 28]. The band gap is measured to $1.9eV$ (see Figure 2.3). The value for the LUMO level ranges from $2.9eV$ to $3.3eV$ [25, 26, 27, 28].

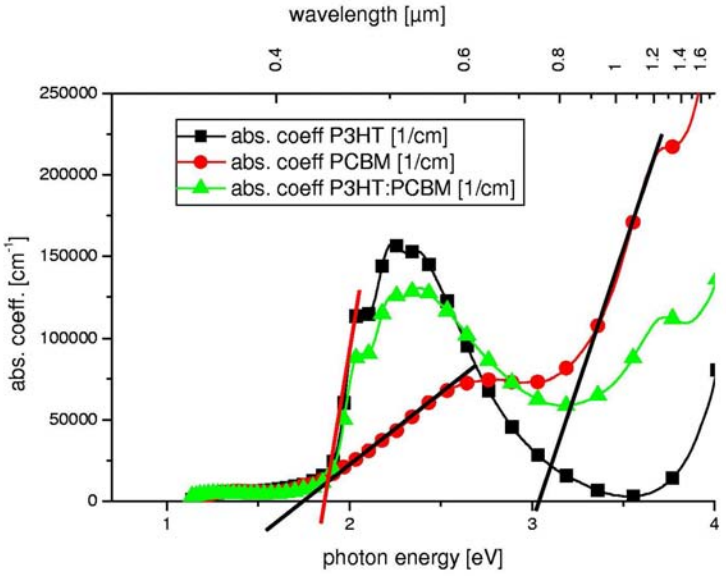

Figure 2.3: Absorption coefficient of P3HT (green triangles), PCBM (red circles) and blend of P3HT with PCBM (black squares) vs. the photon energy. At the onset of the absorption spectra a straight line can be fitted. From the intercept of this line with the x-axis, the bandgap can be calculated.

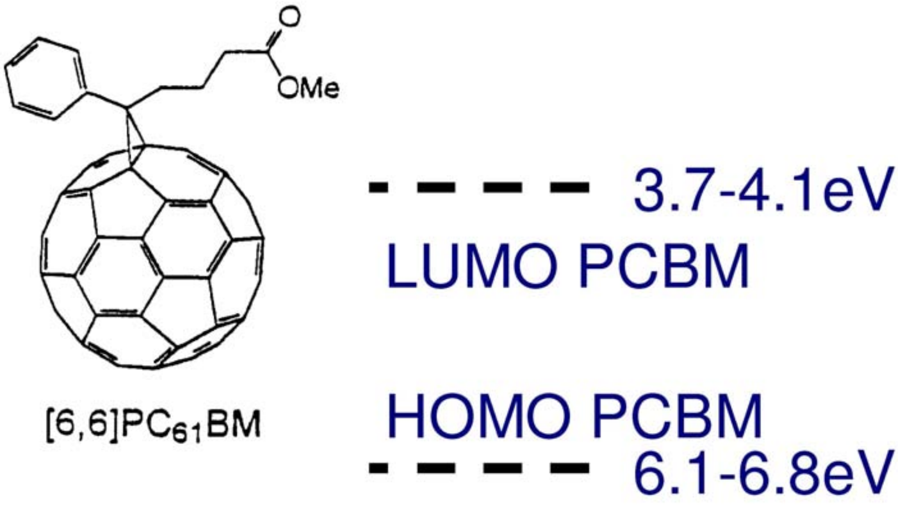

(a) (b)

Figure 2.4: (a) The chemical structure of [6,6]-phenyl C61-butyric acid methyl ester (the fullerene PCBM). (b) Energy scheme of PCBM. The values for the HOMO and LUMO change for different measurements and are often supposed to be the same as for C_{60} [20, 34]. The value for the HOMO level is given from 6.1 eV [33, 26] to 6.8 eV [32]. The value for the LUMO level is given from 3.7 eV [33, 26] to 4.1 eV [32].

2.2.3 Blends of the Electron Transporter with the Hole Transporter

Blends of P3HT with PCBM form a bulk heterojunction. Blends are produced by casting a solution of both materials on a substrate. The solvent is usually aromatic (chlorobenzene, xylene, toluene) or non aromatic (chloroform, tetrahydrofuran). The absorption spectrum is shown in Figure 2.3 and is a superposition of the absorption spectra of the pure materials. Upon illumination a photoinduced charge transfer takes place [36, 37].

Blending of the two materials influences the hole and electron mobility. For films, where one component is below the percolation threshold of about 17% [38, 39, 40], the mobility of the highly concentrated component is nearly unchanged and the mobility of the other one is lower, than for the pristine film [41]. For comparable concentrations of the electron and hole transporting material, where both materials are above the percolation threshold, the value of the n-mobility is given by the n-material and the value of the p-mobility is in the range of the p-material. The lower mobility is limiting the charge extraction, because differences between the p- and n- mobility lead to the formation of space charge. As the mobilities of both materials used are in the same magnitude, the mobility is in the same order of magnitude ($\mu_{n,p} \sim 10^{-3} cm^2 V^{-1} s^{-1}$) [35, 29, 30] .

The difference of the LUMO of the PCBM and the HOMO of the P3HT limits the maximum photo-voltage [22, 21], while this maximum photo-voltage may be lowered due to the given morphology [24]. If the contacts are non ohmic, the work function of the contact may also have an influence of the photo voltage [33].

2.2.4 High Workfunction Electrode

The bottom electrode is indium-tin-oxide (ITO) sputtered on glass substrate. ITO is a highly doped n-type semiconductor with a band gap of $\sim 3.8eV$ and therefore semi transparent for visible light. The exact parameters, like work function, surface roughness, of the ITO may change from one batch to the other [42].

2.2.5 Interfacial Layer

An interfacial layer is introduced between the ITO and the bulk heterojunction, in order to compensate for the variation in the ITO parameters, like work function and roughness. The interfacial layer is $poly(ethylene\, dioxythiophene)$ (PEDOT) doped with polystyrene sulphonic acid (PSS), a highly doped organic semiconductor. The chemical structure is given in Figure 2.5. The work function of PEDOT can be tuned to form an ohmic contact to the polymer [23, 43].

2.2.6 Low Workfunction Electrode

The top electrode is an evaporated low work function metal layer, such as aluminum, calcium, magnesium.

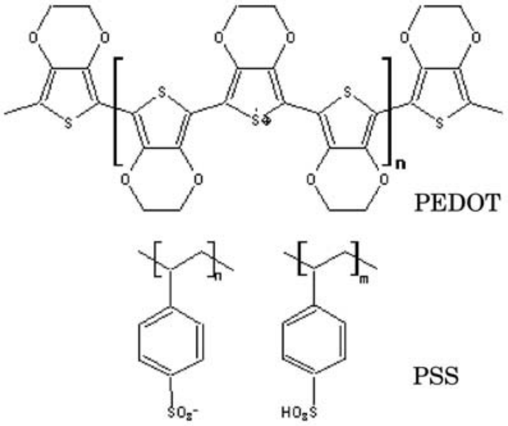

Figure 2.5: The chemical structure of PEDOT and PSS.

2.3 Coating Techniques for Bulk Heterojunctions

The particularity of bulk heterojunction solar cells is that the layers can be deposited from solution. The semiconductors are solved in a common organic solvent. The semiconductor solution is cast on the substrate or underlying film in order to form a homogeneous wet film of the semiconductor solution. The solvent is then dried and the semiconductor film is formed. The two casting methods used will be discussed in this section.

2.3.1 Doctor Blading

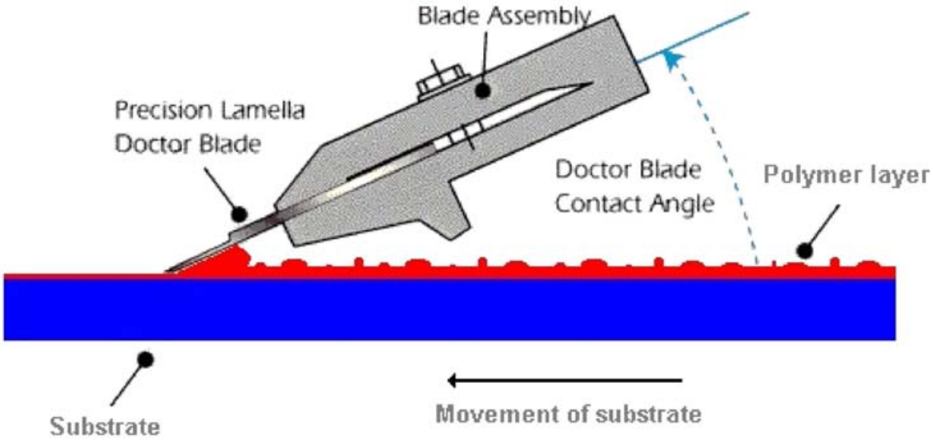

Figure 2.6: Scheme of the working principle of the coating done by doctor blading. On the substrate (blue) the solution (red) is placed in front of the blade. The blade is moved over the substrate with a defined slit height and blading speed. Picture after [44]

The doctor blading process is mostly compatible with common printing techniques for a role-to-role production. With the doctor blading technique, the solution is spread over the substrate with a doctor blade. The principle of this technique is shown in Figure 2.6. The blade is placed with a distance in the order of several tens of micrometers over the substrate. The solution is placed in front of the blade. The casting is done by moving the blade relative to the substrate. The thickness of the film is governed by the concentration and viscosity of the solution and can be influenced by the blading parameters, such as speed of the blade, distance of the blade to the substrate, angle of the blade or shape of the blade. The blading parameters have to be optimized in order to get a homogeneous layer.

2.3.2 Spin Coating

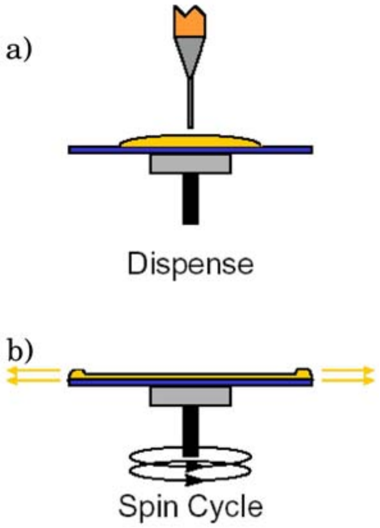

Figure 2.7: Scheme of the working principle of the spin coating technique. a) The solution (orange) is dispensed on the substrate (blue). b) The substrate is rotated and due to the spinning the wet film is formed.

The spin coating process is a process for discrete production of single samples. With the spin coating technique the solution is spread over the substrate by rotation of the substrate. The principle of this technique is shown in Figure 2.7. A certain amount of solution is dropped on the substrate. The substrate starts to rotate and due to the rotation the solution forms a homogeneous film on the substrate. Both, during and after the spinning the solvent is evaporated. Parameters of the technique are the rotation speed and acceleration, the duration of the spinning and the possible combination of several spinning steps with different rotation parameters. The choice of solvent and concentration have a large influence on the film thickness and quality.

2.4 Overview of the Variations in the Preparation

Throughout the thesis different polymers, coating techniques, solvents were used. Table 2.1 summarizes the different variations. In the following chapters a reference to this table will be done either on the process number or name of the process.

Name	Process#	Solvent	donor	acceptor	
Reference	1	non-aromatic-solvent	PAT	PCBM	spin-coating
Optimized	2	aromatic solvent	PAT	PCBM	blading
Purified	3	non-aromatic-solvent	purified PAT	PCBM	spin-coating

Table 2.1: Overview of the parameters, used for the sample preparation.

In this thesis two different process variations are discussed and compared to the reference process#1: the change of the solvent and a usage of different polymers. The two polymers discussed are both poly-thiophenes, one with a larger impurity content (process#1) and the other with low impurity content (process#3). The impurity content arises due to the chemical synthesis and is mainly due to ionic, inorganic elements, like Zn and Br. The change of the solvent in process#2 is accompanied with a change in the coating technique.

Chapter 3

Measurement Methods

In this chapter the methods of measurement are shown. The setups for the measurements are described. Possible sources for uncertainties in the measurements and the evaluation methods are discussed. These measurement methods will later be used for the analyses of the organic bulk heterojunction solar cells.

3.1 Current-Voltage Measurement

The standard measurement is the measurement of the current-voltage behavior. This measurement is done by doing a voltage sweep and for every voltage V applied to the sample the current density I through the sample is measured. The experimental scheme is shown in Figure 3.1(a). The IV-curve is measured using a Keithley2400 Source-Measure-Unit, controlled by a LabView program. For the IV-measurement under illumination, a solar simulator (Fa. Steuernagel) is used, which provides a homogeneous illumination close to the spectrum of the sun (AM1.5 simulated spectrum). The light intensity is measured using a calibrated Si-solar cell. As the spectral sensitivity of the Si-solar cell and the sample are different, the mismatch between the solar simulator spectrum and the true solar spectrum, may result in an over- or underestimation of the photon flux.

Very informative is the variation of the I-V measurement with the illumination intensity and the temperature. The illumination intensity can be varied by inserting neutral density filters between the solar simulator and the sample. The temperature of the sample can be controlled with a Peltier element, which is thermally coupled to the sample via a block of copper or with the samples placed in a temperature controlled cryostat.

The power conversion efficiency is one of the most critical parameters of a solar cell. The power, a power source is producing, is the product of the current density, discussed above (1.3), with the applied voltage and can be determined out of the current - voltage - curve.

A typical IV-curve is given in Figure 3.2 in the dark and under illumination. The dark IV-curve shows diode behavior, with low current densities for reverse voltages (negative bias on ITO) and an opening, with high current densities, for forward voltages (positive bias on ITO).

Under illumination the photogenerated current is added to the dark IV-curve. In a first approximation this added photocurrent can be assumed as constant. In the 4th quadrant the product of voltage and current is negative and the solar cell generates power, while in the 1st

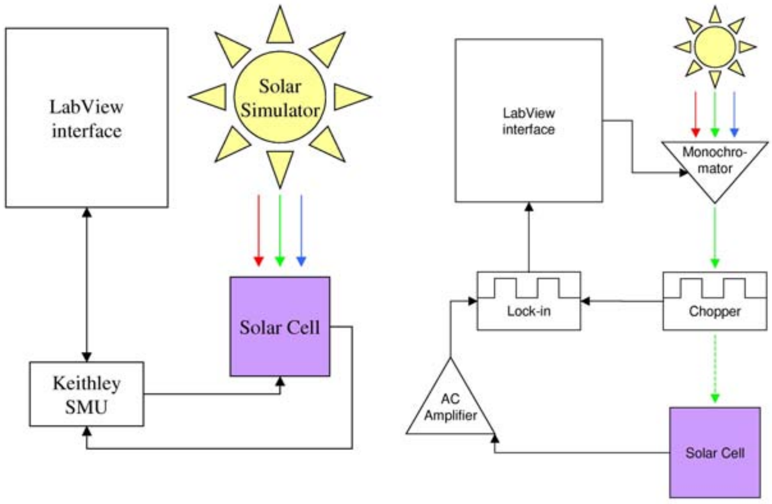

(a) (b)

Figure 3.1: (a) Scheme of the IV-measurement setup. The sample (solar cell) can be illuminated via a solar simulator. A voltage is applied on the sample and the current through the sample is measured. (b) Scheme of the setup for measuring the external quantum efficiency. The incident light passes through a monochromator and a chopper wheel. The photocurrent is measured using lock-in technique in respect to the chopper frequency and recorded with a LabView Program.

and 3rd quadrant it consumes power. The photogenerated current under condition $V = 0V$ applied bias is the short circuit current density I_{SC}. The dependence of the photogenerated current with the voltage is discussed in chapter 4.2 and chapter 5.1.1.3.

The intercept of the illuminated IV-curve with the x-axis is the open circuit voltage V_{OC}. At the V_{OC} the photogenerated current compensates the dark current and therefore the total current is zero.

For an ideal solar cell, the IV-curve would be perpendicular and forming a rectangle together with the x- and the y-axis. Then the maximum power would be the product of the I_{SC} with the V_{OC}, as depicted with the yellow rectangle in Figure 3.2. In reality, the IV-curve deviates from this ideal behavior and therefore the maximum power is lower than this product. The maximum power of a real solar cell is determined by multiplying the measured current with each applied voltage and taking the maximum of the produced power in the 4th quadrant. The maximum power point m_{pp} is shown in Figure 3.2 and the area of the green square is representing this m_{pp}. A measure for the ideality of the solar cell is the ratio of the m_{pp} to the ideal power given by the product of the I_{SC} and V_{OC} and is called the fill factor ff (equation (3.1)).

$$ff = \frac{m_{pp}}{I_{sc} \cdot V_{oc}} \tag{3.1}$$

The power conversion efficiency is the ratio of the maximum power extracted from the solar cell to the incident light power P_{light} and can be expressed with the I_{SC}, V_{OC} and ff, as shown in equation (3.2).

$$\eta = \frac{m_{pp}}{P_{light}} = \frac{I_{SC} \cdot V_{OC} \cdot ff}{P_{light}} \tag{3.2}$$

The short circuit current represents the photon to electron conversion efficiency as discussed above (chapter 1.3). The shape of the dark IV-curve governs the open circuit voltage and the fill factor and as the dark IV-curve is a diode curve, the parameters of the diode determine the ff and V_{OC}. On the other hand the diode parameters will represent the layout of the solar cell, like junctions, morphology, carrier density. This will be discussed in more detail in the next chapters 4 and 5.

The power conversion efficiency of solar cells can be represented by the solar cell parameters open circuit voltage V_{OC}, short circuit current I_{SC} and fill factor ff. For an increase of the efficiency the single parameters should be increased. The examination of these parameters and their improvement will be discussed in the following chapters.

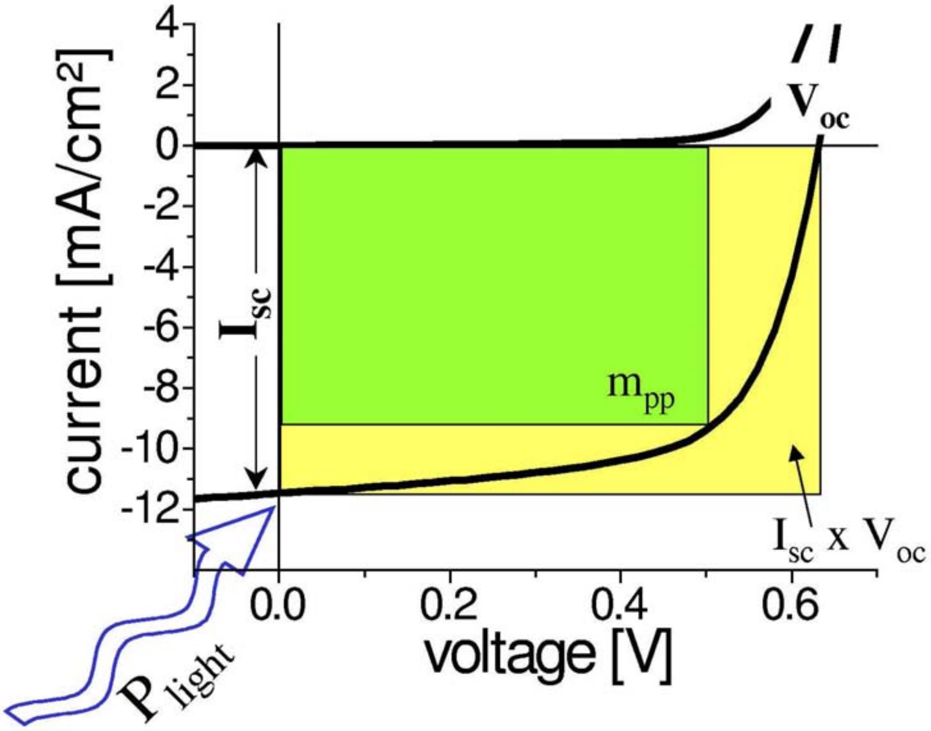

Figure 3.2: Characteristic IV-curve of a solar cell in the dark (upper curve) and under illumination (lower curve). The parameters I_{SC}, V_{OC}, m_{PP} and the power of the incident light P_{light} are depicted. The ideal power of a solar cell is represented by the area of the yellow square. The real maximum power is represented by the green square.

3.2 Absorption and Transmission

The absorption is measured in reflection geometry or in transmission geometry. The measurement in reflection geometry uses an integrating sphere and corrects reflection on interfaces.

For the measurement of the transmission coefficient of a single layer, the absorption of the sample (substrate + layer) is measured in reflection geometry. First a baseline is taken with a white reflecting teflon piece instead of the sample. Then the sample is measured with a light trap, which is reflecting no light, behind the sample, to measure just the reflection on the interfaces. Finally, the sample with a mirror behind the sample is measured. With these three curves the transmission spectra T_{sample} can be calculated according to equation (3.3)

$$T_{sample} = 1 - \frac{R_{sample} - R_{light-trap}}{R_{baseline} - R_{light-trap}} . \tag{3.3}$$

If reflections on layer interfaces are expected to be low, these measurements can also be done in transmission geometry, using a reference measurement of the substrate.

For the measurement of the part of absorbed photons in the device, the measurement of the baseline is done as before. The measurement of $R_{light-trap}$ is done with the light trap and no sample. For the measurement of the device the metal electrode is used as reflecting mirror. The percentage of absorbed photons in the whole device is then calculated as given in equation (3.4).

$$A_{device} = \frac{R_{device} - R_{light-trap}}{R_{baseline} - R_{light-trap}} \tag{3.4}$$

3.3 External and Internal Quantum Efficiency

The external quantum efficiency (EQE) is a spectral measurement of the percentage of the number of electrons extracted out of a solar cell per incident photon.

The measurement setup is shown in Figure 3.1(b). The photocurrent spectrum is measured. The light is spectrally dispersed by a monochromator. The light intensity is modulated by using a chopper wheel with a frequency around $200Hz$. The chopped, monochromatic light illuminates the solar cell and the current of the solar cell is measured. With lock-in technique the current produced by the chopped, monochromatic light can be calculated and any background current due to noise or bias light is corrected.

This photocurrent spectrum is measured twice, first for a calibrated Si-solar cell with known photocurrent spectrum. With this measurement the spectrum of the lamp is calculated. Then the photocurrent spectrum of the sample is measured. With these two measurements the EQE can be calculated. The first calibration scan can be repeated to cross-check if the spectrum of the lamp is changed during the measurement.

The internal quantum efficiency (IQE) is the spectral measurement of the number of electrons extracted out of a solar cell, normalized on the number of photons absorbed within the active layer. For this measurements the optical losses have to be known. The number of photons absorbed within the active layer are calculated according to equation (3.3). The IQE is the EQE corrected for optical losses, as given in equation (3.5)

$$IQE = EQE/A_{device} , \tag{3.5}$$

with A_{device} being the ratio of absorbed photons in the active layer. With an interfacial layer in between the substrate and the active layer, this absorption has to be corrected, as will be discussed later in section 5.1.2 and section 5.1.3.

3.4 Measurement of the Illumination Intensity Dependence of the Photocurrent

In the ideal case, a solar cell should have a linear response of the photogenerated current I_{light} on the incident illumination intensity P_{light}. In the real case the response is in the form of equation (3.6)

$$I_{light} \sim P_{light}^{\alpha}\,. \tag{3.6}$$

The scaling exponent α can be determined by measuring the photogenerated current I_{light} for different light intensities either using grey filters as discussed above in section 3.1, or with a more accurate linearity measurement.

The measurement using neutral density filters is straightforward, but have a quite high uncertainty, because two measurements are necessary for each light intensity. First the light intensity has to be determined using a calibrated Si-solar cell and then second the photogenerated current of the sample has to be measured. If the calibrated solar cell and the sample have different spectral sensitivities, these reference measurements will lead to an over- or underestimation of the light intensity, especially if the absorbance spectra of the grey filter is not flat and/or changing the relative absorption spectra from one filter to another.

To overcome this uncertainty, we measure the response of the sample on a small chopped illumination with various bias light intensity, as depicted in Figure 3.3(a) and called *linearity measurement*. A chopped light beam, either monochromatic, or white light is used to probe the sample. The photocurrent, generated by this chopped light is measured via a lock-in amplifier, while the sample is illuminated with a bias light of changing intensity. At the same time the bias light is measured. The light intensity of the chopped light should be small in respect to the bias light intensity.

The sample gives a response according to equation (3.6). A small change in the light intensity is then the deviation of equation (3.6) and measured by the lock-in (equation. (3.7)), where $Lockin$ is the value, measured by the lock-in amplifier.

$$Lockin = \frac{\Delta I_{light}}{\Delta P_{light}} \sim \alpha \cdot P_{lilght}^{\alpha-1} \tag{3.7}$$

In a double logarithmic representation of the lock-in value vs. the measured bias current I_{light}, a slope m can be evaluated, using equation 3.8. This leads to the dependence of the the scaling exponent $\alpha = -\frac{1}{m-1}$.

$$log\left(Lockin\right) \sim log\left(P_{lilght}^{\alpha-1}\right) = (\alpha-1)\cdot log\left(P_{lilght}\right) \tag{3.8}$$

$$log\left(Lockin\right) \sim \frac{(\alpha-1)}{\alpha}\cdot log\left(I_{lilght}\right) = \left(1-\frac{1}{\alpha}\right) log\left(I_{lilght}\right)$$

$$\Rightarrow \alpha = -\frac{1}{m-1}\, with\, slope\, m = \frac{\Delta\left[log\left(Lockin\right)\right]}{\Delta\left[log\left(I_{light}\right)\right]}$$

With this linearity measurement the scaling exponent α can be determined without any uncertainties from neutral density filters. This measurement can be done as a function of the chopping frequency or the wavelength of the chopped or bias illumination, but no influence of these parameters are detected for the samples measured.

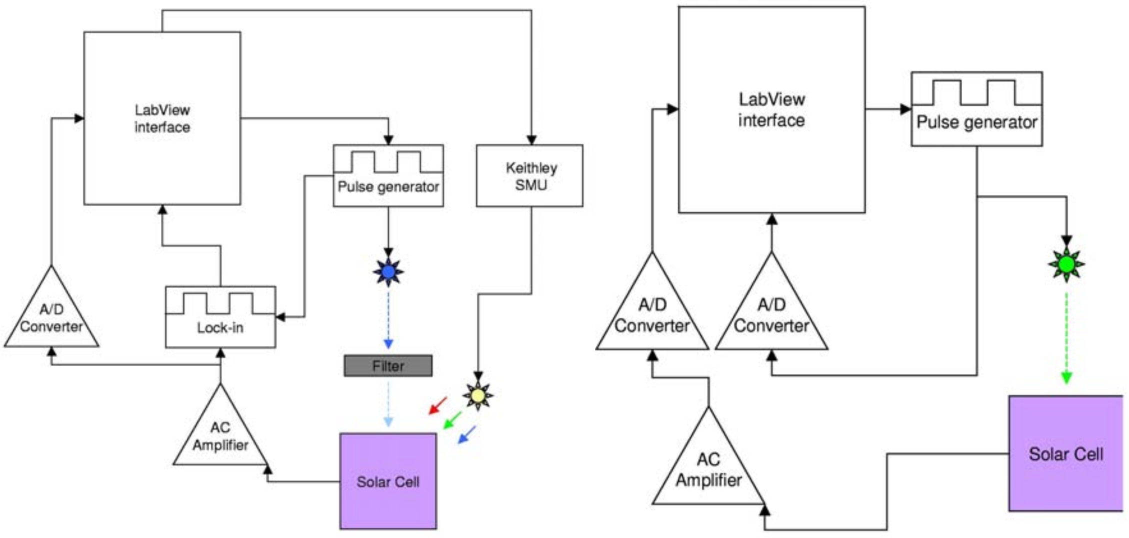

(a) (b)

Figure 3.3: (a) Scheme of the linearity measurement setup. An additional current due to a chopped light beam is measured as a function of the bias light intensity using lock-in technique. (b) Scheme of the setup for measuring the transient photocurrent decay. A light pulse of a LED excites the sample and the current of the sample is recorded by an A/D-converter card.

3.5 Transient-Photocurrent Decay Measurement

The measurement of the transient photocurrent decay is aimed to study the response time of solar cells. The measurement setup is depicted in Figure 3.3(b). The sample is exposed to a pulsed light beam of monochromatic or white light. The current is recorded as a function of the time. The measurement is done either with a 16bit resolution A/D-converter card with a sample frequency of 200kHz, or with an oscilloscope with a 8bit current resolution and a sample frequency of 60MHz. The measurement curve is an integration over at least 100 single measurements.

Possible parameters of this measurement are the duration, wavelength and intensity of the light pulse. Further the voltage applied to the sample during the current measurement, the temperature of the sample and the bias light can be a function of this measurement.

3.6 Measurement of the Accelerated Degradation

Temperature accelerated life time measurements were performed on organic bulk heterojunction solar cells. The current - voltage - behavior of these samples under white light illumination is monitored over time for different elevated temperatures T, ranging from $T = 40..95^{\circ}C$. Illumination is provided by standard halogen lamps. The illumination intensity is kept to approximate $P_{light} \approx 40 \pm 20\,mWcm^{-2}$. No control of the humidity is done.

Up to nine samples with eight single solar cells each can be monitored at the same time. The current - voltage - curve is measured once per hour. In-between the measurements the samples are short cut, so the photogenerated current is flowing through the samples.

The measurements are done on encapsulated samples. The devices are sandwiched between two glass substrates, so the influence of oxygen or water vapor should be low.

Chapter 4

Models of the Bulk Heterojunction Solar Cell

For an understanding of the bulk heterojunction solar cells, two models are introduced and discussed, which allows a simulation of the measured IV-curves. In the first model, called the microscopic model, the bulk heterojunction solar cell is described on a microscopic level, where the transport equations are numerically solved in one dimension for one virtual semiconductor, representing the relevant parameters of both materials used for the bulk heterojunction. The second model, called the macroscopic model, describes the bulk heterojunction solar cell with an extended one-diode equivalent circuit[1].

4.1 Microscopic Model

In this section a one dimensional model is reviewed [47,46], based on solving the transport equations numerically. This model allows a numerical simulation of the current - voltage characteristic, which is compared to the measured IV-curves. Further, the energy levels, carrier density, current density and recombination rates are calculated by the model, which will be discussed in this section.

In contrast to p-n-junction solar cells, the bulk heterojunction has no spatially separated p- and n- region, but a mixture of the p - type and n - type semiconductor on a nanometer scale. Under the assumption that charge separation and generation is uniform all over the bulk, the blend of two unipolar semiconductors can be described as one *virtual* semiconductor representing the properties of both single materials, where the properties of the valence band is given by the polymer and the properties of the conduction band is given by the properties of the acceptor material.

It is assumed, that the virtual semiconductor is essentially un-doped and is in thermal equilibrium without illumination, represented by one Fermi level in the middle of the band gap. Under illumination, the thermal equilibrium is disturbed and the quasi Fermi levels for electrons ϕ_n and holes ϕ_p are splitting from the equilibrium Fermi level E_f according to equation (4.1) and equation (4.2),

$$\phi_n = E_f - \frac{kT}{q} \ln\left(\frac{n}{n_i}\right) \tag{4.1}$$

---

[1] Part of this work is published in [45,46]

$$\phi_p = E_f + \frac{kT}{q} \ln\left(\frac{p}{n_i}\right) \tag{4.2}$$

with n_i the intrinsic carrier concentration and n and p as the total carrier concentrations of the fullerene and polymer respectively. The difference of the quasi Fermi levels is the upper limit for the potential difference $V_{bi} = \phi_n - \phi_p$ across the active layer.

With this simple model for the bulk heterojunction, the solar cell can be described by a geometric model, where the virtual semiconductor is sandwiched between two contacts. Figure 4.1(a) shows the scheme of the device. The semitransparent contact is a two layer contact of the ITO and the PEDOT:PSS, which are assumed as highly doped semiconductors. For the virtual semiconductor the parameters listed in Table 4.1 are assumed. The Fermi level pinning is taken into account for the top metal contact [22, 21].

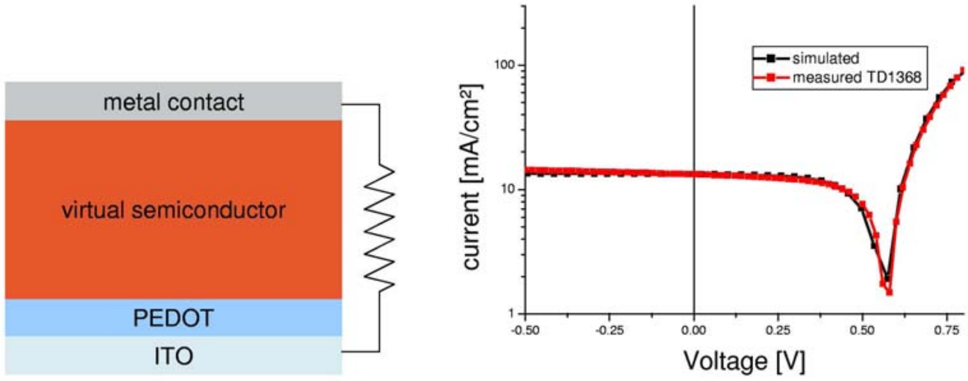

(a) (b)

Figure 4.1: (a) The schematic layout of the bulk heterojunction solar cell. As a semitransparent contact (anode), the ITO, followed by the PEDOT:PSS layer is used. The virtual semiconductor is sandwiched between the PEDOT:PSS layer and the top metal contact. (b) Comparison of a measured (red) and simulated (black) IV-curves. The simulation was done by solving the transport equations self-consistently.

The analysis of the organic bulk heterojunction solar cell on this microscopic level requires the simultaneous solution of two carrier semiconductor transport equations: the hole and electron continuity equations, the Poisson equation and the current transport equation [48] in the one dimensional case, as given in equation (4.3), with the mobility μ of the electrons and holes, the generation rate G, the recombination rate R, the electrical field E, and the densities of negative and positive charge carriers n and p, respectively, the current densities of electrons and holes $I_{n,p}$, respectively, the net charge ρ, the elementary charge q and the dielectric constant ε.

$$I_n = q\mu_n \left(nE + \frac{kT}{q}\frac{\partial n}{\partial x}\right)$$

	polymer	virtual semiconductor	fullerene
valence band $[eV]$	5	5	6.5
conduction band $[eV]$	3.2	4	4
band gap $[eV]$		1	
optical band gap $[eV]$	1.8	1.8	2.5
absorption coefficient α_0 $[cm^{-1}]$		70000	
Fermi level		intrinsic: $4.5eV$	
p-mobility $[cm^2V^{-1}s^{-1}]$	10^{-3}	10^{-3}	$\ll 5 \cdot 10^{-5}$
n-mobility $[cm^2V^{-1}s^{-1}]$	$\ll 5 \cdot 10^{-7}$	10^{-3}	10^{-3}
carrier life time $[\mu s]$		1	
Doping $[cm^{-3}]$		10^{14}	
layer thickness		$200nm$	

Table 4.1: Shown are the values for the virtual semiconductor and the corresponding values of the p- and n-type semiconductor, which the virtual semiconductor is composed of.

$$I_p = q\mu_p \left(nE + \frac{kT}{q}\frac{\partial p}{\partial x} \right)$$

$$\frac{\partial n}{\partial t} = G - R\left(p, n\right) + \frac{1}{q}\frac{\partial I_n}{\partial x} \tag{4.3}$$

$$\frac{\partial p}{\partial t} = G - R\left(p, n\right) + \frac{1}{q}\frac{\partial I_p}{\partial x}$$

$$\frac{\partial E}{\partial x} = \frac{q}{\varepsilon}\rho\left(x\right)$$

The absorption is assumed to be the classical direct absorption, with the absorption coefficient $\alpha = \alpha_0\sqrt{\hbar\nu - E_{opt.gap}}$, where $E_{opt.gap}$ is the onset of the optical absorption. The band gap of the real semiconductors have a larger band gap than the virtual one.

With this model the IV-curve under illumination can be reproduced correctly, as shown in Figure 4.1. The parameters used for the virtual semiconductor are measured values, given in Table 4.1.

Figure 4.2 shows the characteristics of the energy bands, namely the conduction and the valence band and as well as of the quasi Fermi levels, under zero bias, (a) & (c), and under bias compensating the built-in voltage, (b) & (d). Figure 4.2 shows that the electric field is constant over the active layer and no or negligible deviation from this behavior is observed under illumination for all relevant voltages. This shows that the field is the driving force of the carriers. No or negligible influence of the diffusion of carriers can be seen, otherwise a band bending would be expected.

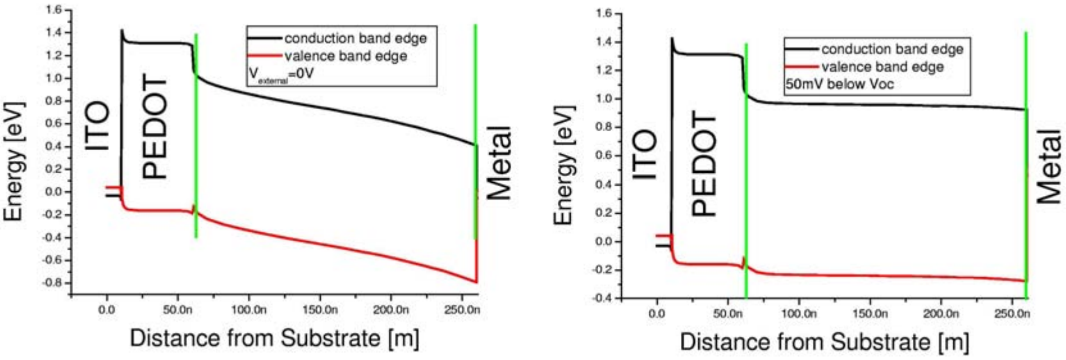

(a) band edges at Isc (b) band edges at Voc

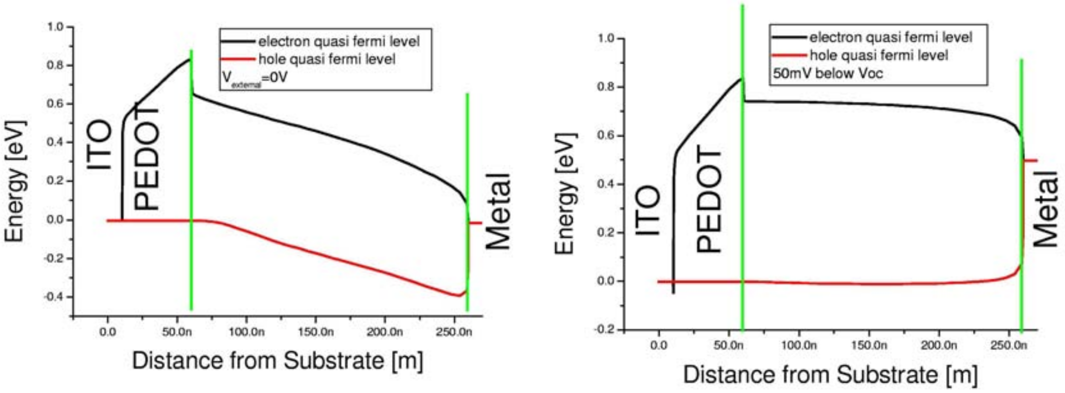

(c) quasi Fermi level at Isc (d) quasi Fermi level at Voc

Figure 4.2: Dependence of the electrical potentials (a)&(b) and the quasi Fermi levels (c)&(d) on the applied voltage as calculated by the microscopic simulation. Shown are (a)&(b) the conduction band edge (black) and the valence band edge (red) and (c)&(d) the quasi Fermi levels for electrons (black) and holes(red) over the distance from the ITO electrode. The PEDOT layer is up to $60nm$ and assumed as a p-type semiconductor. The bulk heterojunction layer is between $60..260nm$ distance from the ITO electrode and assumed as an ambipolar semiconductor. The metal electrode is more than $260nm$ away from the ITO electrode. The potential within the bulk of the solar cell is nearly flat for voltages near V_{OC} (b) and shows a constant decrease, which can be clearly seen under short circuit condition (a) without band-bending.

In summary, this one dimensional model allows to predict the current-voltage-behavior of bulk-heterojunction solar cells. The blend of a polymeric p-type semiconductor with a molecular n-type semiconductor on a nm scale is treated as one virtual, ambipolar semiconductor with the conduction band given by the n-type semiconductor and the valence band given by the p-type semiconductor. A constant field and no band-bending across the $200nm$ photoactive layer is observed. The driving force for the photogenerated carriers is found to be the field and no or negligible influence of the diffusion could be detected.

4.2 Macroscopic Model

An extended equivalent circuit describing the current-voltage characteristics of bulk heterojunction polymer solar cells at different light bias levels is discussed. This extended equivalent circuit was developed together with C. Waldauf and is further described in his thesis [49] and in [45]. This model consists of a one diode-model, which is extended by an extraction model for photogenerated carriers taking into account the effective reduction of the mean distance which the charge carriers cover when sweeping the electrical bias through the 4th quadrant of the solar cell. The model properly describes the current - voltage behavior of bulk heterojunction solar cells over more than three orders in light intensity with one set of parameters.

In the previous section, the current voltage characteristics of bulk heterojunction solar cells were described by solving the transport equations self consistently with the electrical field. These simulations showed that a bulk heterojunction composite can be successfully described by a single intrinsic semiconductor layer with the energy levels of the valence and conduction band as the HOMO of the polymer and the LUMO of the fullerene, respectively. The electrical field is found to be constant over the active layer and no or negligible deviation from this behavior is observed under intense illumination (Figure 4.2). Based on this finding, a macroscopic equivalent circuit is suggested, capable of describing the current - voltage characteristics of bulk heterojunction solar cells under different illumination densities with a single set of parameters. Such an equivalent circuit takes into account the field dependence of the photocurrent.

Before describing the expanded replacement circuit, the deficiencies of the standard one diode model are discussed when applied to describe the current - voltage characteristics of bulk heterojunction solar cells. The model is schematically depicted in Figure 4.3 and equation (4.4) describes the current balance in this circuit. Here, the photo-induced current $I_{photogenerated}$ is added as a current source.

$$I - I_0 \cdot \left(exp\left(\frac{e \cdot (V - I \cdot R_s)}{nk_B T} \right) - 1 \right) - \frac{V - I \cdot R_s}{R_p} + I_{photogenerated} = 0\,, \tag{4.4}$$

where I is the current through the diode, I_0 is the saturation current, k_B is the Boltzmann constant, T the temperature, V is the external bias applied to the diode, n the ideality factor of the diode, R_s is the serial resistance and R_p is the parallel resistance. The dependence of the parallel resistance R_p on the illumination intensity is taken into account by adding a photoconductive part to the dark shunt $R_{p,dark}$ as discussed later (chapter 5.3). This is done by adding a second photoconductive parallel resistor $R_{p_{photoshunt}}$, whose photoconductivity is proportional to the light intensity P_{light}.

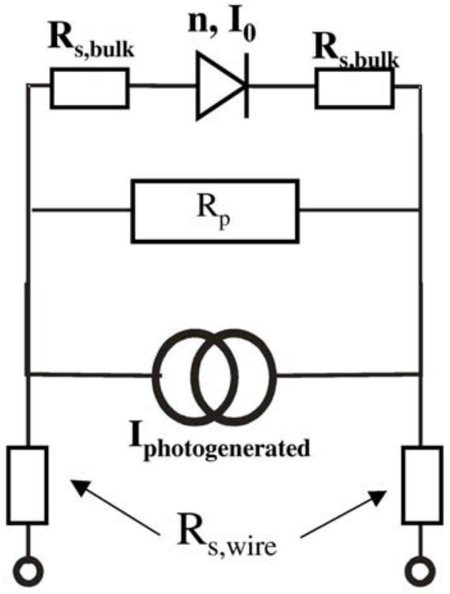

Figure 4.3: Equivalent circuit diagram representing the macroscopic model for describing a solar cell with one diode. The total current at a given voltage V is the sum of single currents: the current through the diode, which is represented by the parameters n and I_0, the current due to the shunt resistance R_P, the limiting series resistance $R_{s,bulk}$ of the active layer and $R_{s,wire}$ of the feed-lines and the light current $I_{photogenerated}$.

Figure 4.4 shows typical current - voltage characteristics of bulk heterojunction solar cells, measured under different illumination intensities together with the optimal fit, by using equation (4.4). The fit parameters are listed in Table 4.2, where R_p is calculated with $R_{p,dark}$ and $R_{p_{photoshunt}}$ via the light intensity.

The general quality of the fits is satisfying. The shunt (characteristic in the voltage regime around $0\,V$, where the IV-curve is linear) and the diode turn on (characteristic in the voltage regime between $0.3\,V$ and $0.6\,V$) of the dark IV-curve is correctly reproduced with a meaningful set of parameters. The slope of the I/V characteristic in the turn on regime is dominantly influenced by the ideality factor n. Also the illuminated IV-curves can be reproduced correctly, however, in order to properly describe the open circuit voltage under increasing illumination density, a continuous increase of the saturation current I_0 is necessary. The variation of I_0 by a factor of two is significant and gives an equivalent shift of the open circuit voltage by nearly $50\,mV$. The variation of diode parameters under illumination can not be justified, since it would correspond to a change of the diode itself under illumination. This is in conflict with equation (4.4), where $I_{photogenerated}$ is the only parameter sensitive to illumination. A fixed set of parameters I_0 and n does not reproduce the illumination dependence of V_{OC} correctly (see Figure 4.5): the higher the light intensity the larger the error in V_{OC}. Also a two diode model, where the second diode is implemented as a Shockley-Read-Hall (SRH) recombination diode [18, 19], could not explain the illumination intensity of the V_{OC}, independent on the ideality factors of these two diodes.

The discrepancy discussed above brings up the deficiencies of the one diode model given

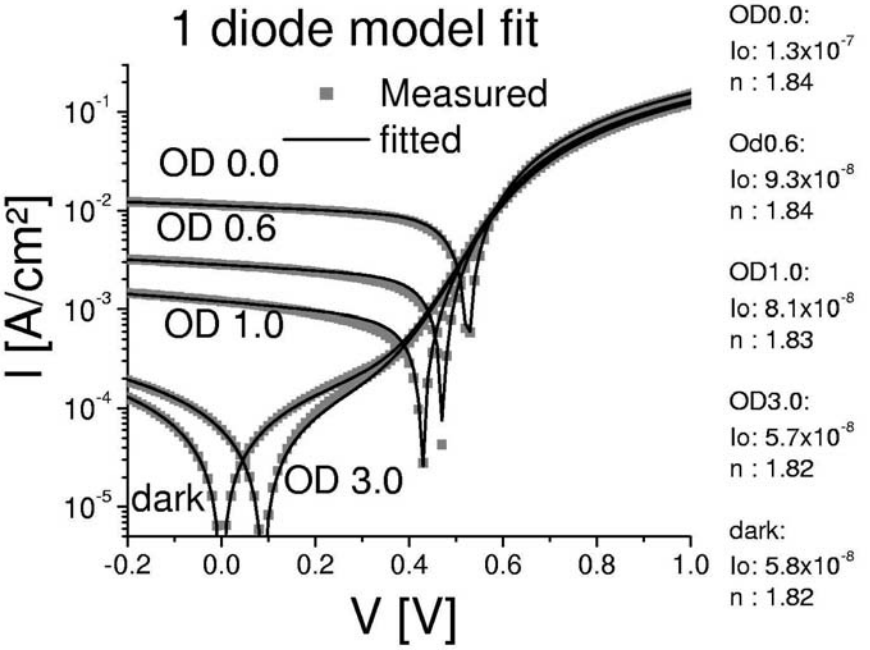

Figure 4.4: IV-curves of a bulk heterojunction solar cell (process# 1) measured under different illumination intensities (boxes) with fitted curves using the standard 1-diode-model (lines). Values for the parameters n and I_0 are given for each light intensity in the legend. The light intensity is given by the value of the optical density (OD) of the various grey filters and the light intensity of $110mWcm^{-2}$ @ $OD0.0$.

in equation (4.4). In order to remove this discrepancy, a more sophisticated model can be used. It was shown above (section 4.1) that the photoinduced current of bulk heterojunction solar cells is driven by the internal electrical field. This is not further surprising for devices with active layers in the $100\,nm$ range, and a constant electric field (as seen in Figure 4.2) further supports these findings. Applying an external bias close to the built-in voltage V_{bi} will compensate this field. Consequently, a decrease of the the average mean carrier distance or drift length d_{drift}, given in equation (4.5), is expected, where τ is the average lifetime of the carriers, μ the carrier mobility and L the thickness of the sample.

$$d_{drift} = \mu\tau\frac{V_{bi}}{L} \tag{4.5}$$

If losses due to the contacts or diffusion are present, the built-in voltage has to be replaced by the flat-band voltage V_{FB}, which takes these losses into account. Equation (4.5) suggests that $I_{photogenerated}$ should not be considered as constant with voltage. If the drift length is smaller than the thickness of the sample, just the fraction $\frac{d_{drift}}{L}$ will reach the contacts and can be extracted from the solar cell. Therefore in the expansion of the one diode model, the dependence of $I_{photogenerated}$ on the voltage should be taken into account. Similar models have been used to describe IV-curves of amorphous silicon (a-Si) - solar cells [50,51], when transport is limited by the field driven average mean-carrier-distance.

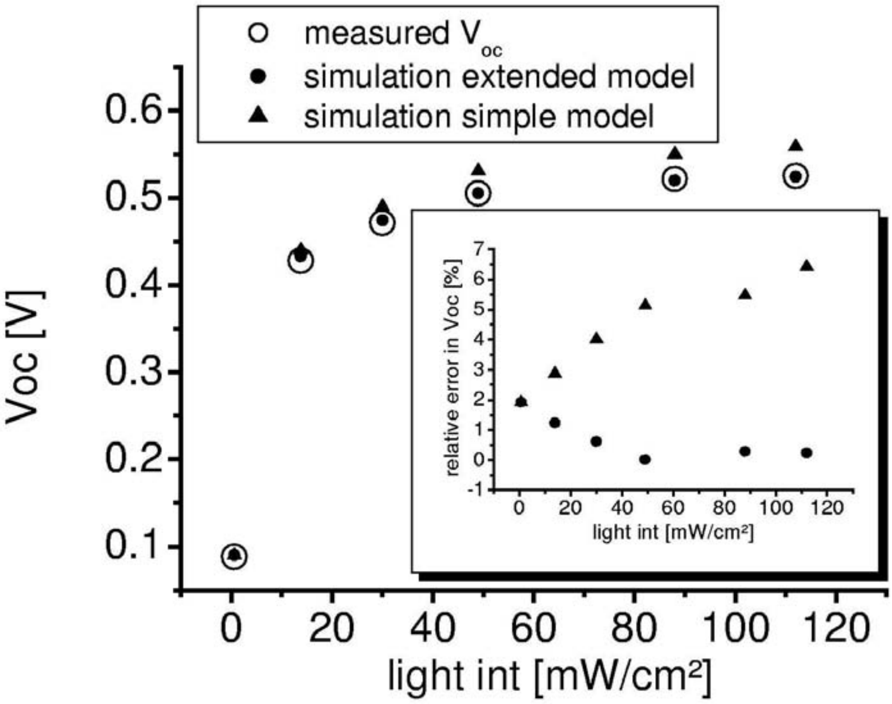

Figure 4.5: The open circuit voltage (V_{OC}) vs. light intensity (open circles ○), fitted with the standard one-diode-model (closed triangle ▲) and fitted with the extended model (closed circle ●). The inset shows the relative error of the V_{OC}-value calculated within the standard model and the extended model to the measured value. Data taken from devices fabricated by using the process#1.

First, the current density of the photogenerated charge carriers is calculated. Since the solar cells discussed here show no or only negligible carrier losses (an internal quantum efficiency of $\approx 100\,\%$ and an external quantum efficiency of $\approx 80\,\%$ was measured [52], as discussed later in 5.13), the current density of the photogenerated carriers can be estimated directly from the short circuit current I_{SC} which is equivalent to $I_{photogenerated}\,(V = 0)$. The photogenerated charge carriers are now driven by the field due to the difference between the internal built-in voltage V_{bi} [21, 22] and the applied voltage V. The number of carriers which can be extracted from the device equals the total number of carriers multiplied by the ratio of the drift length and the thickness of the sample, whereas this factor is at maximum 1. The overall photogenerated current $I_{photogenerated}$ can be rewritten as given in equation (4.6).

$$I_{photogenerated} = \begin{cases} -\left|I_{sc}\right| & if\ \mu\tau \cdot \frac{(V_{bi}-V)}{L} > L \\ \left|I_{sc}\right| & if\ \mu\tau \cdot \frac{(V-V_{bi})}{L} > L \\ \left|I_{sc}\right| \cdot \mu\tau \cdot \frac{(-V+V_{bi})}{L^2} & else \end{cases} \tag{4.6}$$

Here the assumptions are made, that the charge carriers are generated homogeneously over the whole bulk heterojunction layer and the all carriers have the same carrier mobility and lifetime.

Reversal of the photocurrent between the 4th and the 1st quadrant is a consequence of a

OD filter	n	saturation current I_0 $[A/cm^2]$	R_s $[\Omega cm^2]$
0	1.84	$1.3 \cdot 10^{-7}$	2.2
0.6	1.84	$9.3 \cdot 10^{-8}$	2.5
1.0	1.81	$8.1 \cdot 10^{-8}$	2.5
3	1.82	$5.7 \cdot 10^{-8}$	2.6
dark	1.82	$5.7 \cdot 10^{-8}$	2.4

Table 4.2: Fit parameters n, I_0 and R_s for IV-curves (process#1) measured under various light intensities, fitted using standard 1-Diode-Model. The light intensity is given by the value of the optical density (OD) of the various grey filters and the light intensity of $110mWcm^{-2}$ @ $OD0.0$. R_p is calculated with the dark shunt $R_{p,dark} = 1540\Omega cm^2$ parallel to a photo conductive resistor with the photo conductivity $R^{-1}_{photoshunt} = 5.3 \cdot 10^{-5}\Omega^{-1}cm^{-2}mW^{-1}$.

field driven light generated current. In forward direction the photocurrent contributes to the total current, e.g. due to photoconductivity. Equation (4.6) does not contain direct carrier recombination. In the case of recombination losses, I_{SC} in equation (4.6) has to be replaced by $I_{SC,0}$, the maximum possible (optically limited) primary photocurrent which can be extracted under high reverse bias. Alternatively, more sophisticated models can be taken into account. Such models, regarding the influence of direct recombination processes have been discussed for a-Si devices [50,51]. These models were applied to fit the bulk heterojunction data presented in Figures 4.4 and 4.6 and it turned out, that direct recombination processes are not relevant for the bulk heterojunction data presented. However, the relevance of these more sophisticated models [50,51] for other bulk heterojunction materials or material combinations, can not be excluded.

The extended one diode model composed of the standard one diode model (equation (4.4)) and the field depended photo current extraction (equation (4.6)) will now be tested on the experimental data set shown in Figure 4.4. The fitting of IV-curves is done by iteratively minimizing the mean least error χ, which is given by the sum over the differences between the measured and fitted currents at each voltage, as shown in equation (4.7).

$$\chi^2 = \sum_V \left[I_{measured}(V) - I_{fitted}(V)\right]^2 + \left[log\left(I_{measured}(V)\right) - log\left(I_{fitted}(V)\right)\right]^2 \quad (4.7)$$

With this iterative method, the parameters of the dark diode I_0, n, R_s and $R_{p,dark}$ are determined first. Then, keeping the dark diode parameters constant, the built-in voltage, the mobility μ and the carrier life time τ are determined by fitting the illuminated IV-curves. The set of fitted parameters is listed in Table 4.3. The mobility was kept constant at $10^{-3}cm^2V^{-1}s^{-1}$ in accordance to literature values for P3HT [53,54] and PCBM [53,35]. Figure 4.6 shows again the experimental data compared to the fitted data as calculated from equation (4.3). Again, excellent agreement is observed, but, in contrast to the simple one diode model, the expanded model can reach this high quality of the fit with one and the same set of parameters. Most importantly, the open circuit voltage is fitted correctly over more than three orders of magnitude of variation of illumination intensity with one set of parameters (Figure 4.5).

Plotting the IV-curve in a linear scale reveals a small deviation in the fourth quadrant just before the open circuit voltage is observed (Figure 4.6). This deviation is supposed

n	I_0	R_s	$R_{p,dark}$	μ	τ	V_{bi}
1.791	$4.8 \cdot 10^{-8} Acm^{-2}$	$2.1 \Omega cm^2$	$1540 \Omega cm^2$	$10^{-3} cm^2 V^{-1} s^{-1}$	$7.1 \cdot 10^{-6} s$	$0.61V$

Table 4.3: Fit parameters n, I_0, R_s, $R_{p,dark}$, $R^{-1}_{photoshunt}$, μ, τ and V_{bi} for IV-curves (process#1) measured under various light intensities, fitted using the expanded 1-Diode-Model with non constant I_{light}. R_p is calculated with the dark shunt $R_{p,dark}$ parallel to a photo conductive resistor with the photo conductivity $R^{-1}_{photoshunt} = 5.3 \cdot 10^{-5} \Omega^{-1} cm^{-2} mW^{-1}$.

to originate from the rather crude assumption in the model that all photogenerated carriers have identical mobility and lifetime. Due to the neglection of a distribution of mobility and life time values, the photocurrent at the opening of the diode and, therefore, the fill factor are slightly overestimated.

As a benefit of the expanded model, a mean carrier life time $\tau = 7.1\,\mu s$ is estimated, which is elaborate to obtain with other methods. The value for τ of several microseconds determined by fitting experimental data with the expanded diode model is similar to the carrier lifetimes determined from transient absorption measurements on polymer bulk heterojunction films [55]. The value of the built-in voltage of $V_{bi} = 0.61\,V$, as gained by the expanded 1-diode model, is also in good agreement with the measured open circuit voltage.

The $\mu\tau$ - product can also be calculated without doing the whole fitting procedure as described above. The photogenerated current can be extracted from the measured IV-curves. The current under illumination $I_{light}(V)$ is the sum of the dark current $I_{dark}(V)$ and the photogenerated current $I_{photogenerated}$ (equation (4.4)). Therefore the photogenerated current is $I_{photogenerated} = I_{light} - I_{dark}$. The voltage has to be corrected for the voltage drop over the series resistance R_S. For small values of R_S or for small currents, this can be neglected. From the difference $I_{light} - I_{dark}$, the intercept with the x-axis and the slope around this intercept can be determined and the $\mu\tau$ - product and the built-in voltage, according to Equation 4.6 can be calculated. Similar values for the mobility and charge carrier lifetime are obtained by this method of calculating and evaluation the photogenerated current $I_{photogenerated}$ and by fitting equation (4.4) and (4.6).

A modified one diode model is suggested to describe the illumination dependence of current-voltage characteristics of polymeric bulk heterojunction solar cells. This expanded one-diode-model takes into account the field dependence of the photo generated current. Excellent results are obtained for the expanded model. IV-curves of bulk heterojunction solar cells are properly described with one set of parameters, especially the dependence of the open circuit voltage on the light intensity can be reproduced very exactly. Moreover, the model allows an estimation of the built-in voltage V_{bi} and of the mean carrier life time τ or of the $\mu\tau$ - product, if the mobility μ of the tested material is unknown. Small deviations in the fourth quadrant are due to the fact, that the model does not take into account the statistical distribution of the mobility and lifetime. All in all, the new model provides a new insight into the working mechanisms of bulk heterojunction solar cells and helps to identify the critical parameters for further improvements of these cells.

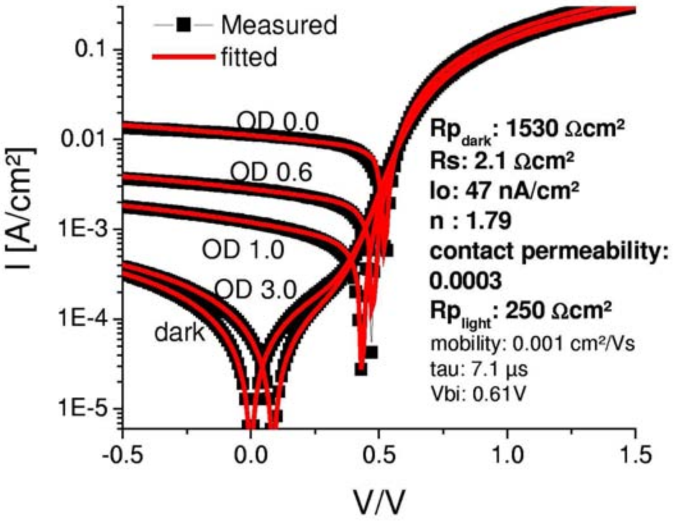

(a) IV-curves for different illumination intensities

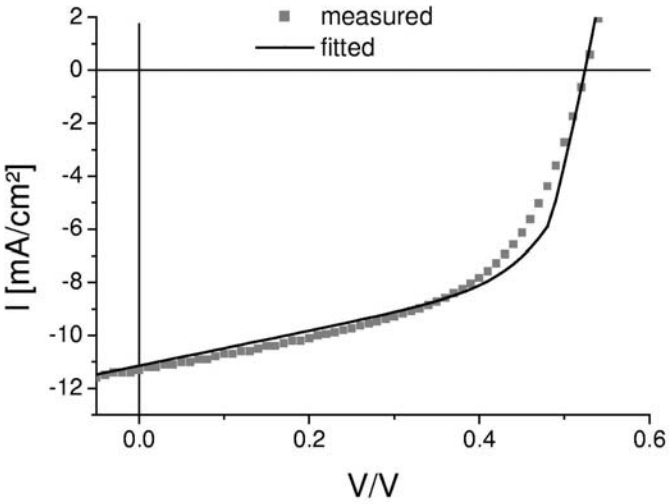

(b) comparison measurement - simulation under full illumination

Figure 4.6: a) IV-characteristics of bulk heterojunction solar cells (process# 1) measured under various light intensities (boxes) as indicated in the legend. The fitted curves (solid lines) are obtained by using the 1-Diode-Model with field dependent light generated current $I_{photogenerated}$. Values for the model parameters are given in table 4.3 and are the same for each light intensity. The light intensity is given by the value of optical density of the various gray filters and the light intensity of $110mWcm^{-2}$ @ OD0. b). The measured (boxes) and fitted (line) IV-curves in the fourth quadrant in a linear scale for $110mWcm^{-2}$ show a deviation from each other.

Chapter 5

Analysis of the Losses in the Power Conversion Efficiency

In this chapter the losses in the power conversion efficiency are discussed by evaluating losses in the single parameters short circuit current, open circuit voltage and fill factor. Based on the loss evaluation, suggestions for improvement of the single parameters and the total efficiency are made and tested[1].

Under zero voltage the efficiency of the photon to electron conversion can be tested without any influence of losses due to resistances or the diode. The shape of the IV-curve has no influence on the photon to electron conversion at I_{SC}. For an examination of the single processes of the photon to electron conversion efficiency of the bulk heterojunction solar cell the samples are measured under short-circuit condition. The short-circuit current summarizes the efficiency of the single processes: photon absorption, charge generation, charge transport and collection. The efficiencies and losses of these single processes are investigated in the first part of this chapter. With these results, improvements are proposed and investigated.

The shape of the curve, described by the macroscopic model determines the parameters V_{OC} and ff. In the second part of this chapter the V_{OC} is examined. The dependences of the V_{OC} with the parameters of the macroscopic model are shown and the relevant parameters are discussed. The relevance of these parameters is tested with experiments, in which these parameters are changed intentionally and the influence on the V_{OC} is tested. Possible improvements are proposed and investigated.

The same is done for the fill factor in the third part of this chapter. The dependence of the parallel resistance with illumination intensity, its origin and its influence on the fill factor are discussed.

5.1 Processes of the Photon to Electron Conversion

In this section, the losses in the I_{SC}, the efficiencies of the single steps of the photon to electron conversion are investigated. The efficiency of the charge transport and collection efficiency are measured by measuring the transport parameters μ and τ and recombination (section 5.1.1). Losses in the photon absorption are examined by optical measurements

---

[1] Part of this work is published in [52, 45, 56, 57]

in 5.1.2. With the external quantum efficiency (EQE), the calculated internal quantum efficiency (IQE) and a comparison of the measurements done so far, the efficiency of the charge generation can be estimated for different photon wavelengths (5.1.3). With this results the main loss factors are determined and a possible efficiency enhancement is suggested in 5.1.4.

5.1.1 Charge Carrier Transport and Recombination

In this subsection the transport and the recombination of separated charge carriers are investigated. Once free charge carriers are generated, these carriers have to be transported to the electrodes in order to extract current out of the solar cells.

The transport mechanism in organic material is supposed to be either by hopping or influenced by trapping and trap-release as discussed in 5.1.1.2. The parameters of these transport mechanisms are influencing the mobility of the carriers [58]. The driving force for the carriers may be either diffusion, drift or a combination of both. The microscopic simulation shows, that the carriers are mainly field driven. On their way to the electrodes the carriers may recombine.

The main recombination mechanisms are supposed to be direct recombination of free electrons with holes and the trap-assisted recombination. The average time, the carriers survive, prior recombination is the carrier lifetime τ. The recombination will be a loss in the photocurrent $I_{photogenerated}\left(V, P_{light}\right)$.

Direct recombination is a recombination, where one carrier gets into the capture cross-section of a carrier with opposite charge [48]. Therefore the rate of the direct recombination is proportional to the density of both types of carriers $n_{p,e}$ and the recombination rate will be proportional to the square of the photogenerated carrier density. The rate equation is

$$\frac{dn_{photo}}{dt} = G\left(t\right) - \frac{n_{photo}(t)}{\tau} - \beta n_{photo}^{2}\left(t\right) \tag{5.1}$$

[59, 17, 48, 60], with n_{photo} representing the photogenerated carrier density, G the generation rate which is proportional to the light intensity, τ the monomolecular lifetime and β the bimolecular recombination rate coefficient. In the steady state the change of the carrier density $\frac{dn_{photo}}{dt} = 0$ and the carrier density and thus the photogenerated current is proportional to the square of the light intensity

$$I_{photogenerated} \sim n_{photo} \sim G^{0.5} \sim P_{light}^{0.5}\,. \tag{5.2}$$

The recombination for trap assisted recombination or Shockley-Read-Hall-recombination is a two step process [18, 19]. First, one carrier is caught by a trap. From this trap the carrier may be released or it can recombine with a carrier of opposite charge. The recombination rate will be proportional to the light intensity $R_{SRH-recombination} \sim n \sim P_{light}$ and the photogenerated current will be also proportional to the light intensity $I_{photogenerated}\left(V, P_{light}\right) \sim P_{light}$. For this recombination mechanism the carrier lifetime will be independent in the light intensity.

As the carrier transport is field driven, the relevant value for the charge transport is the drift length $d_{drift} = \mu\tau E$, with the carrier mobility μ, the carrier lifetime τ and the driving field E. The field E is given by $E = \frac{V_{FB}-V}{L}$, where V_{FB} is the internal flat-band voltage, driving the carriers and V the external applied voltage, as discussed in 4.2. The drift length is the average length the carrier cover, before they recombine. If the drift length is larger

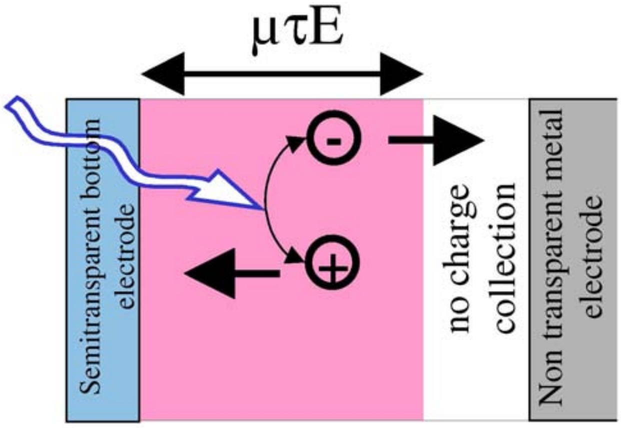

Figure 5.1: Scheme of charge extraction, influence of μ,τ and E. The carriers are driven by the electric field E and cover the distance $\mu\tau E$, which is the drift length. From this drift length the carriers can be extracted. Carriers more far away from the contacts than the drift length do not reach the contacts prior recombination.

than the thickness of the sample L, each carrier will reach the contact, prior recombination. If the drift length is smaller than the sample thickness, just the fraction $\frac{d_{drift}}{L}$ will reach the contact (see Fig 5.1). The drift length d_{drift} can be changed either by a change of one of the values μ, τ or E. The effect of changing the drift length via internal field E is described in section 4.2 and 5.1.1.3. In 5.1.1.1 the drift length is changed via the temperature dependence of the $\mu\tau$ - product. In 5.1.1.3 the drift length is changed via the applied external bias V.

5.1.1.1 Low Temperature Measurements for the Drift Length Determination

Several transport parameters are temperature dependent [35, 58, 61, 62]. The temperature dependence of the mobility μ is expected to be larger than of the carrier lifetime, therefore the $\mu\tau$ - product can be influenced via a change of the temperature. The $\mu\tau$ - product decreases with decreasing temperature.

Figure 5.2 shows the result of a measurement, where the short circuit current I_{SC} is measured for temperature T ranging from $T = 120..350K$ for two different sample thicknesses, as described in chapter 3. For both samples two temperature dependences can be observed: a saturation regime, where the current is nearly constant with temperature and a regime, where the current is temperature dependent, with a monotonic rising of the current with temperature. The temperature where the current starts to saturate is the point, where the drift length is equal to the sample thickness. For the 70nm thick sample the drift length starts to saturate at $T \approx 150K$, i.e. far below the room-temperature. For the 350nm sample the saturation point is at about room-temperature.

The rise of the saturation temperature with rising thickness is clear from equation (4.6), where the sample thickness is quadratic in the formula, for the value of the drift length, when the photogenerated current starts to saturate.

The slight increase of the current in the saturation regime is possible due to reduced second order recombination.

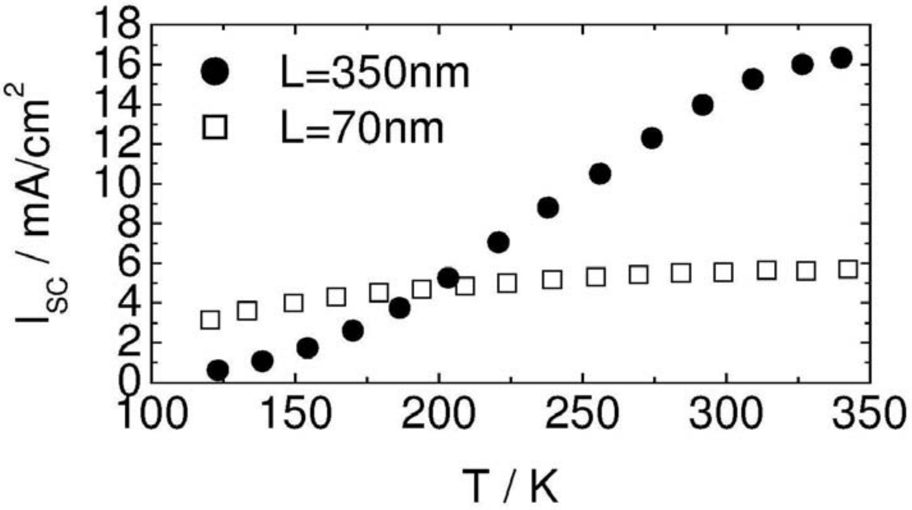

Figure 5.2: I_{SC} vs. T for different thicknesses. Results are taken from [56, 63]. Shown are the temperature profiles of the short circuit current density for a 350nm (closed circles) and 70nm(open squares) thick sample.

The temperature and layer thickness dependent IV-measurement shows a saturation and a temperature dependent regime, where the turnover between these regimes is the temperature, where the drift length reaches the sample thickness. From this measurement the drift length can be evaluated at room-temperature to $d_{drift} = 350nm$. Up to this thickness no first order recombination occurs, which is then also the maximum thickness for recombination free transport of bulk heterojunction solar cells made of this material combination. The influence of second order recombination will be discussed later in 5.1.1.4. With the drift length, the estimated internal voltage $V_{FB} = 0.6V$ (Table 4.3) and the measured value for the mobility $\mu = 0.001\frac{cm^2}{Vs}$, the carrier lifetime τ can be estimated to $\tau = 2\mu s$.

5.1.1.2 Measurement of the Transient Photocurrent Decay

In order to determine the charge carrier lifetime independently of the mobility, another approach is discussed in this subsection. For a:Si-solar cells and photodetectors transient photocurrent measurements were used for determination of the carrier lifetime τ [64, 65, 66]. For a:Si an exponential decay is observed with long residual currents, which can be correlated to trap states in the band gap. If this method would work also for the measurement of the carrier lifetime in bulk heterojunction solar cells it would be an easy and powerful tool for the determination of recombination velocities.

For bulk heterojunction solar cells the transient absorption spectroscopy is often used in order to get information on the formation and recombination of charge carriers [67, 68, 69]. With the transient absorption spectroscopy the change in the absorption of the polymer is measured, which is a measure of the carrier density on the polymer.

These transient absorption measurements give a power law-dependence of the carrier density $n \sim t^{-\gamma}$ with time t, which can be understood by a model, where transport of the carriers is limited by trapping and de-trapping of the carriers, as described in [68]. Trapping

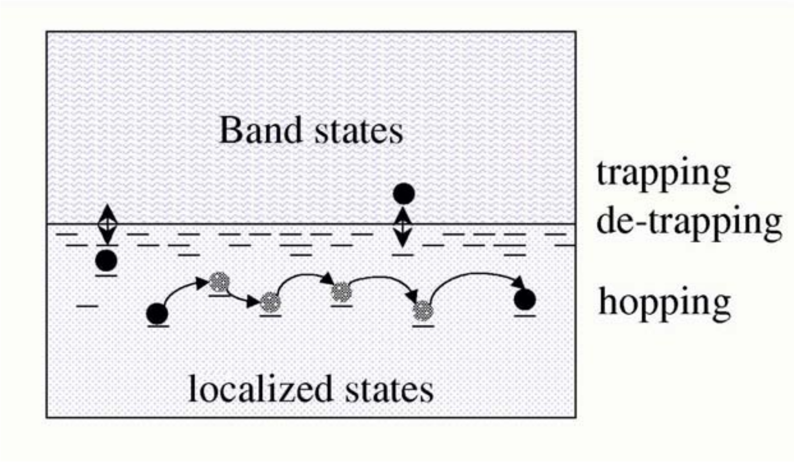

Figure 5.3: Scheme of different transport mechanisms in disordered systems. Carrier transport may derive from trapping and de-trapping or by hopping from one site to another. Picture after [70]

and de-trapping of carriers is one common picture of transport in disordered systems. During the movement of a charge carrier in the blend it may be trapped, will remain for a certain time, depending on the trap-energy, before it is de-trapped again and move further through (Figure 5.3) [70]. The energetic distribution of the traps is assumed to be exponential or the tail of a Gaussian. Another possible transport mechanism is hopping transport, where every step from one site to another needs a certain time, depending on the energetic and spatial distance of these two sites (Figure 5.3) [**?**].

These transient absorption measurements are usually done under open circuit conditions or even without any electrodes. Under external bias the measured current $I(t)$ should follow a similar power law dependence $I(t) \sim t^{-(1-\gamma)}$ [70] for times smaller than the transit time t_r and $I(t) \sim t^{-(1+\gamma)}$ [70] for times larger than the transit time t_r, where the transit time t_r is the time the fastest carriers need to cross the whole sample [70]. This is valid for both types of dispersive transport, the trapping-de-trapping and the hopping type.

The measurement is described in section 3.5. The measurements are done on bulk heterojunction cells (process#1) with an absorber thickness $L \approx 300nm$. Measurements were taken and evaluated on two different time scales: one with a low resolution in time (0.1ms) and a high resolution in the current signal and another one with a high resolution in time (100ns) and a low resolution in the current signal. The RC-constant of the device is in the order of 10ns below the resolution of the setup and should therefore not influence the measurements.

Figure 5.4 shows a measurement with the fast and the slow time resolution. For the transient photocurrent decay, a fast drop at the beginning can be seen, followed by a long residual current up to several tens of ms. The measurement shows no exponential decay, as it was observed for a:Si, but a power law decay (Figure 5.5). Therfore the analysis done for a:Si-solar cells can not be used here for the bulk heterojunction cells, but the analysis done for dispersive transport has to be tested.

With the mobilities of the single components in the order of $10^{-3}cm^2V^{-1}s^{-1}$, the sweep out time of the carriers will be in the range of 1μs, much lower than the resolution of the

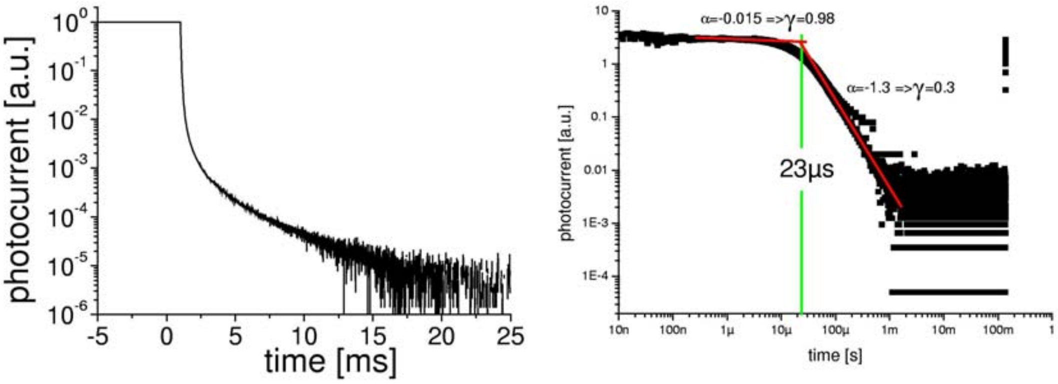

(a) slow decay

(b) fast decay

Figure 5.4: Measurement of the transient photocurrent decay, a) low time resolution, high current resolution and b) high time resolution and low current resolution. Here the slope of the two visible regimes are given and the time is noted, when the one regime turns over into the other. Samples prepared with process#1, according to Table 2.1.

measurement with the low resolution in time. Therefore the evidence of this measurement will be minor. With this measurement carriers are measured, which are remaining orders of magnitude longer in the bulk heterojunction than the majority of the carriers. To distinguish between hopping transport or transport limited by trapping and release for this long persisting charge carriers, the measurements were repeated under different voltage bias applied and with different temperatures. Figure 5.5 shows the variation of the temperature during the measurement. The slope of the curves is independent of the temperature. So there is no sign of a thermally activated process for the transient photocurrent on this long time scale. This would have been expected for a trapping-de-trapping process. The variation of the applied bias also shows no visible effect. Hence, the hopping transport can not be recognized with this measurement.

The only dependence the measurement of the transient photocurrent decay of bulk heterojunction shows is with the illumination intensity used for the pulsed illumination. This dependence is not conform with neither hopping, nor with trapping-de-trapping, but this measurement can be a hint that an accumulation of carriers occurs and therefore the transport is limited by space charge due to the carrier accumulation. This can be avoided by using a shorter light pulse, but is not tested in this thesis.

It is not possible to get clear results out of the photocurrent decay measurements with the low time resolution.

The timescale of the fast measurement of the transient photocurrent decay is within the expected sweep out time of the carriers. So the question is, if the signal (Figure 5.4) is representing the sweep out of carriers or the recombination of the carriers. The measurement of the $\mu\tau$-product in 5.1.1.1 suggests that the transportation at room-temperature for a 200nm thick device is recombination free and therefore the sweep out of carriers is measured. The recombination free transport is later proven in 5.1.3

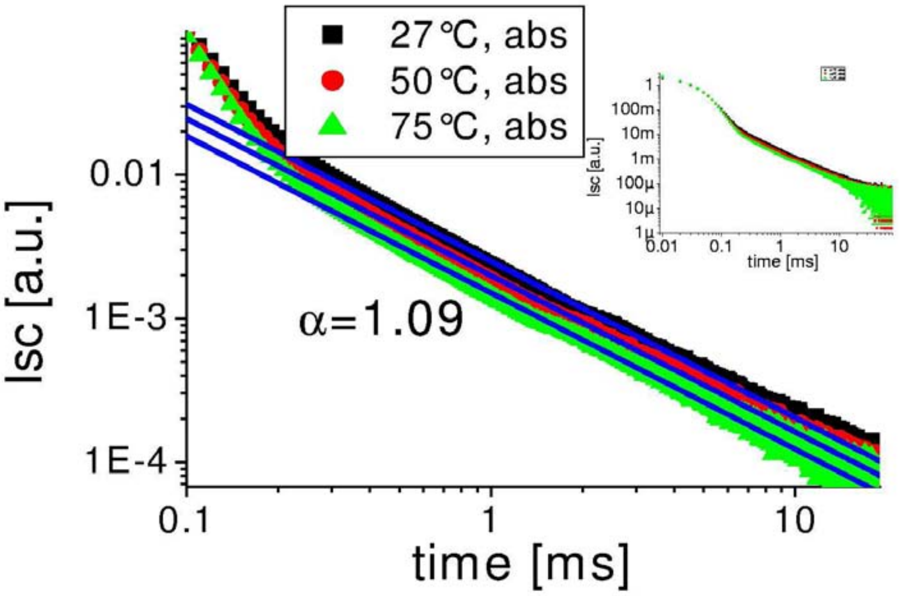

Figure 5.5: Transient photocurrent decay measured for different temperatures in double logarithmic representation. The inset shows the whole timescale of this measurement. Samples prepared with process 1, according to Table 2.1

In the fast measurement of the transient photocurrent decay the two regimes, proposed by [70], can be detected (Figure 5.4). The time, where the slope is changing, is supposed to be the transient time t_r, the time the carriers need to traverse the whole sample. For times smaller $t < t_r$ the current is given by carriers of equal velocity but different spatial distribution within the sample. Therefore the current is nearly constant in this time scale. For dispersive transport, the slope in the double logarithmic plot should change from $(1-\gamma)$ to $(1+\gamma)$ [70]. The evaluation reveals that this is not true for this measurement: for times smaller t_r, a different γ is revealed than for times larger t_r. This measurement is not suitable to detect the expected fingerprint for disordered transport.

If the interpretation of the transition time as the time, the fastest carriers need cross the sample, the value for the mobility can be calculated to be as

$$\mu = \frac{l^2}{V_{bi} t_r} \approx 5 * 10^{-5} cm^2 V^{-1} s^{-1} ,$$

with the thickness of the layer $l = 300nm$, the built-in voltage V_{bi} estimated as $V_{bi} = 0.6V$. This value is about 2 orders of magnitude lower than expected from the mobility values for the used polymer and fullerene.

In summary the measurement of the transient photocurrent decay gives no clear results and helps not determining the charge carrier lifetime τ.

5.1.1.3 Determination of the $\mu\tau$ Product with the Model of Field Dependent Charge Extraction

In this subsection, the determination of the $\mu\tau$ product via the macroscopic simulation, as described in section 4.2 will be shown. The macroscopic simulation shows that by adding the voltage-dependent photogenerated current $I_{photogenerated}$ to the dark current I_{dark} the IV-curves (see equation (5.3)) can be simulated with one set of parameters for different illumination intensities. The photogenerated current can be calculated by subtracting the dark IV-curve from the illuminated IV-curve (Equation (5.3)).

$$I_{light}\left(V\right)=I_{dark}\left(V\right)+I_{photogenerated}\left(V\right) \tag{5.3}$$

$$I_{photogenerated}\left(V\right)=I_{light}\left(V\right)-I_{dark}\left(V\right)$$

The voltage has to be corrected for the voltage drop over the series resistance R_S. For small values of R_S or for small currents, this can be neglected. The photogenerated current is constant as long as the drift length d_{drift} is larger than the sample thickness L (equation (4.6)) . For voltages, where the drift length is smaller than the sample thickness a constant slope is expected. From this slope the $\mu\tau$ product and the flat band voltage V_{FB}, which is the driving voltage for the carriers, can be calculated.

The photogenerated current $I_{photogenerated}\left(V\right)=I_{light}\left(V\right)-I_{dark}\left(V\right)$ is plotted in Figure 5.6 for illumination with 1 sun ($100mWcm^{-2}$) and for different illumination levels. From the curve illuminated under 1 sun three different regions can be distinguished. For voltages $V\lesssim 0.4V$ $I_{photogenerated}$ is nearly constant. The small slope is attributed to an increased current via a lowered shunt resistance under illumination, as discussed later (section 5.3). For voltages $0.4V\lesssim V\lesssim 1V$, a monotonic increase of $I_{photogenerated}$ can be seen until the curve changes the slope again. When comparing the curves of the photogenerated currents for different illumination intensities a similar behavior can be seen for all curves. All curves have nearly the same intercept with the x-axis and the shape of the curves is the same for voltages smaller than this intercept. In contrast, the values in forward direction, after the first intercept with the x-axis show a decrease for small illumination intensities. This means that a negative-photoconduction occurs for low light intensities, the current in forward direction is lower for small illumination than without illumination. The origin of this negative photoconduction is supposed to be an artefact of the measurement, where either the temperature of the samples changed or the cell changes the injection properties during the measurement.

Around the intercept of $I_{photogenerated}$ with the x-axis the solar cell is in the drift length limited regime. A straight line can be extrapolated in this regime. With the slope and the intercept of this line, the $\mu\tau$ product and the flat-band voltage V_{FB} for the different illumination intensities is calculated. The results in Figure 5.7 show a small variation of the lifetime τ and a slight increase of V_{FB} with increasing light intensity. The small variation in the carrier lifetime shows no trend and, as the variation is smaller than 5% of the average value, this is interpreted as a statistical variation and τ is taken as constant with light intensity. The flat band voltage shows also just a small change, but a clear trend can be seen. With increasing light intensity the flat band voltage is increasing.

The independence of τ with the light intensity is a hint that the recombination mechanism is first order and no second order recombination can be detected. If bimolecular

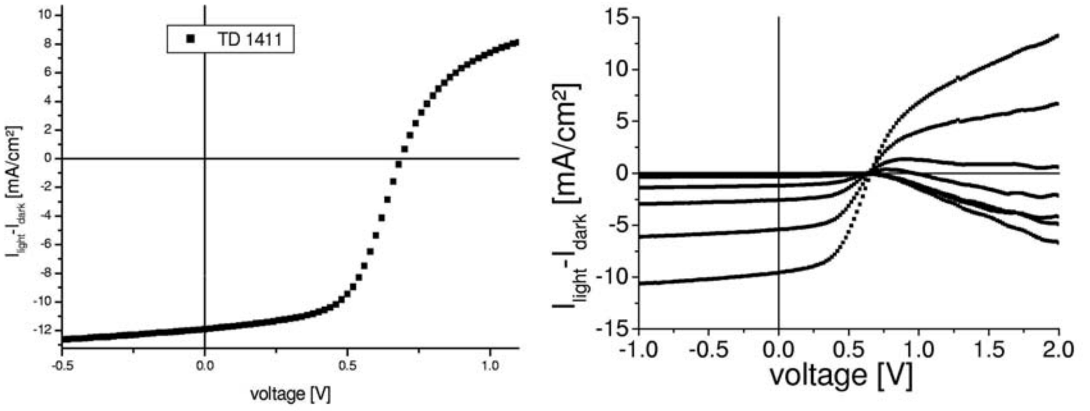

(a) 1 sun

(b) different light intensities

Figure 5.6: The photogenerated current $I_{light} - I_{dark}$ vs voltage V for a) illumination with $100mWcm^{-2}$ and b) for different illumination intensities, for samples prepared with process 2, according to Table 2.1.

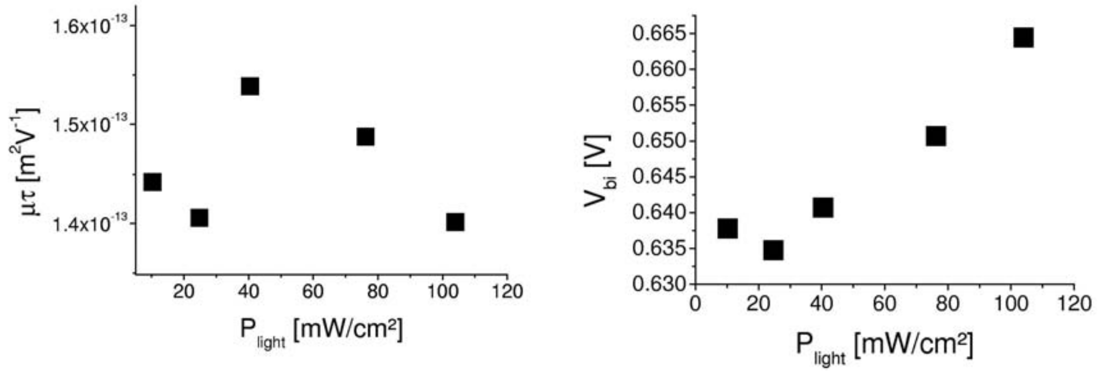

(a)

(b)

Figure 5.7: (a) The carrier lifetime - mobility product $\mu\tau$ and (b) the flat band voltage V_{FB} for different illumination intensities P_{light}, as calculated from the slope and intercept of $I_{light} - I_{dark}$ as shown in Figure 5.6 using equation (4.6) and (5.3).

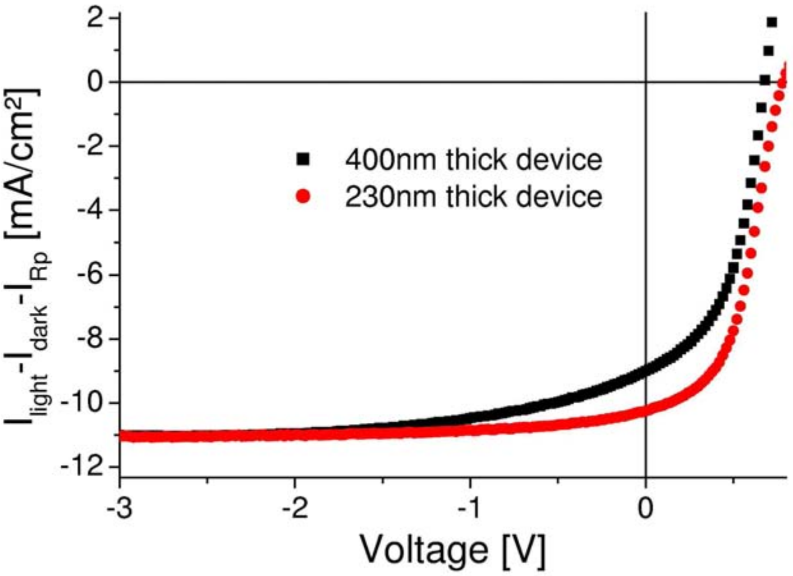

Figure 5.8: The photogenerated current in dependence of the applied external voltage for a 400nm (squares) and for a 220nm (circles) thick device (process#2, according to Table 2.1).

recombination would be a significant recombination mechanism, the lifetime τ would decrease with increasing illumination intensity, because the recombination probability of one carrier would depend on the carrier density and therefore the lifetime of the carrier would decrease with increasing carrier density. The carriers recombine via traps, which are always filled up due to the incident illumination and no direct carrier recombination could be detected.

The slight increase of the flat band voltage with light intensity could reflect the increasing quasi Fermi level splitting with increasing photogenerated carrier density n_{photo}. The splitting of the quasi Fermi levels is $E_{f,n,p} \sim \log{(n_{photo})}$ [48]. The driving field for the carriers will depend on the difference of the quasi Fermi levels and therefore increase with increasing carrier density or light intensity.

With this method, the $\mu\tau$ - product, the flat-band voltage and the drift length can be determined. The drift length is calculated to $d_{drift} \approx 500nm$. This is comparable to the value determined by the low temperature measurement.

The influence of the drift length can also be seen when comparing IV curves in reverse for devices with different thickness. In Fig 5.8 the photogenerated current is shown for devices with 400nm and 220nm sample thickness. The current at $0\,V$ for the thicker device is lower than the current of the thin device and shows a larger slope than the thinner device. For voltages below$-2\,V$, both curves saturate at the same current density. The thin sample needs a lower voltage, the internal built-in voltage is sufficient, for extracting all carriers. For the thicker sample an external bias has to be applied to extract all photogenerated carriers. Under external voltage of $-2\,V$, the field is high enough for extraction of all photogenerated carriers.

5.1.1.4 Second Order Recombination

So far, no hint of bimolecular recombination could be detected. Here the results of the measurements of the bimolecular recombination are evaluated.

Second order or bimolecular recombination is a direct recombination of free carriers with carriers of the opposite charge. In contrast to first order recombination, where charges are first trapped and then recombine, the rate of the second order recombination is dependent on the carrier density of both, electrons and holes. Therefore the number of lost carriers is quadratic with the carrier density. The current, representing the extracted carrier number per time-unit is not linear with light intensity anymore. If the recombination is second order, a dependency of the short circuit current $I_{SC} \sim P_{light}^{0.5}$ with the illumination intensity P_{light} would be measured. When both types of recombination occurs, a dependency $I_{SC} \sim P_{light}^{\alpha}$ will be measured, with the scaling exponent α, ranging from $\alpha = 0.5$ (only second order recombination) to $\alpha = 1$ (only first order recombination).

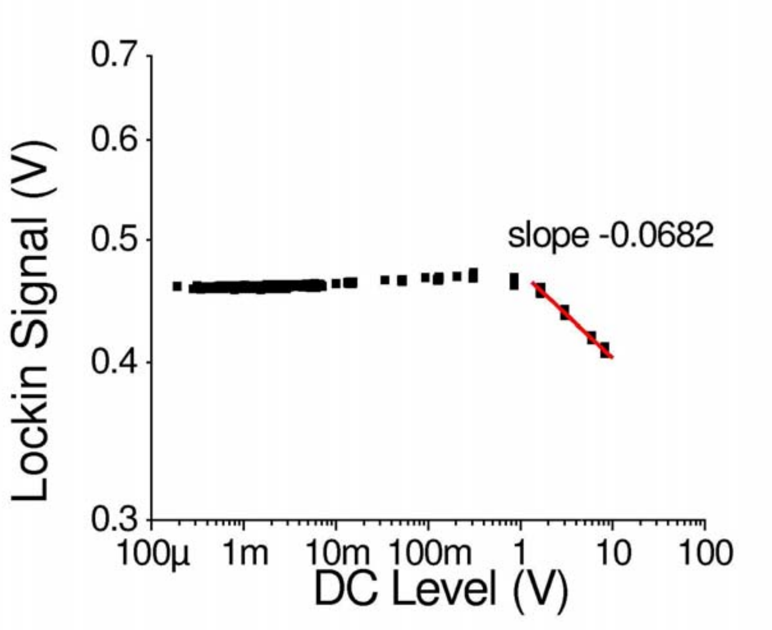

Figure 5.9: Linearity measurement for a sample, made by process#1. Given are the values of the lock-in amplifier vs. the values of the bias level, in a double logarithmic representation. A constant decrease can be seen for high bias values. A fit with a straight line is done for this decrease, and the value of the slope is given in the Figure.

Samples (process #1) are tested with the two methods for measuring the light intensity dependence of the short circuit current, as described in 3.4. The results of the linearity measurement are shown in Figure 5.9. For low bias signal, at low bias light intensity, a constant or even a slight increase of the lock-in signal, with increasing light intensity, can be seen. For higher bias signals, a negative slope is present.

The positive slope for low light intensities represents a scaling exponent α larger than 1. This can be explained by trap-filling due to the bias light, leading to a slight increase in mobility and a better transport therefore. The negative slope for higher light bias, represents the second order recombination. The scaling exponent α is determined from the value of

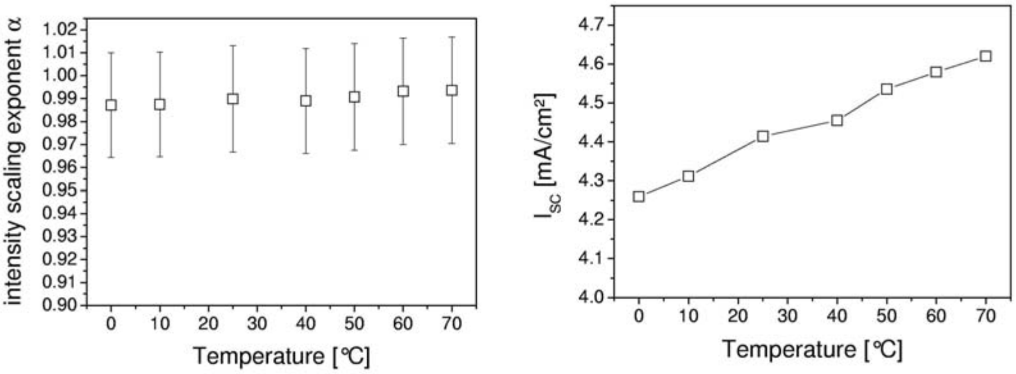

(a) (b)

Figure 5.10: (a) The scaling exponent α for different temperatures T and (b) the short circuit current I_{SC} vs. temperature, measured on samples prepared with process 1, according to Table 2.1. Illumination is done with approximately a) 0.1 to $50\,mWcm^{-2}$ and b) $50\,mWcm^{-2}$.

the slope to $\alpha = 0.936$. For high light intensities, bimolecular recombination is present. Unfortunately the corresponding illumination intensity for the bias level, when second order recombination becomes relevant is not measured with this method.

The results for the measurement, using the method using different optical density filters, as described in section 3.4, are shown in Figure 5.10(a). Here the illumination intensity is varied from 0.05 to $50\,mWcm^{-2}$. The mean value of the scaling exponent α of these samples is slightly below 1, while the uncertainty of the measurement is larger than the deviation from 1. A small increase of the mean value of α with increasing temperature can be observed.

For these samples, no or negligible bimolecular recombination can be detected with this measurement. The mean value of the measurement is just below 1, which is a hint that a small fraction of second order recombination is present. The increase of the mean value of the scaling exponent with temperature (Figure 5.10 b) fits to an expected reduction of the recombination, due to increased mobility with increasing temperature, and also with the observed increase of the I_{SC} with the temperature.

5.1.1.5 Summary of Transport and Recombination Measurements

In this section, different possibilities for measuring the drift length, as well as the mobility-lifetime-product were investigated. The temperature dependent IV-measurement, which is based on the change of the drift length via the temperature dependence of the $\mu\tau$ - product and the analysis of the field dependence of the drift length via the voltage dependent measurement of the photogenerated current reveals a similar drift length of $d_{drift} \approx 0.4..0.5\mu m$.

The measurement of the photogenerated current under different applied voltage shows the characteristics expected from the macroscopic simulation model. The field dependence of the carrier extraction can be seen from this measurement and the $\mu\tau$ - product can be calculated. The $\mu\tau$ - product shows no dependence on the light intensity. The flat band voltage increases slightly with illumination intensity.

The linearity measurement allows to distinguish between recombination mechanisms with high accuracy. The recombination mechanism is predominantly of monomolecular type. The carriers recombine via traps and not with carriers of the opposite charge.

The measurement of the transient photocurrent decay are not directly related to the $\mu\tau$ - product. The measurements do not show the expected characteristics of either hopping nor trapping-limited transport. The interpretation of these measurements is not clear and direct comparison with transient absorption measurements under different bias would be helpful.

5.1.2 Optical Losses

The number of generated charge carriers is limited by the number of absorbed photons in the active layer with the photon energy higher than the band gap of one of the components. Therefore the optical losses due to reflection at an interface or absorption in the substrate have to be derived. The photons, which are not absorbed in the active layer or reflected at an interface or absorbed in the substrate, are lost for the charge generation. Measured is the reflection of the total device R_{device} and the absorption of the ITO-PEDOT-substrate $T_{substrate}$ (Figure 5.11) according to section 3.2. The reflection R_{device} measures every photon which is not reflected and detected by the absorption spectrometer, but absorbed within the device, as shown in equation (5.4)

$$R_{device} = 1 - A_{device} = T_{substrate} \cdot T_{BHJ} \cdot T_{substrate}\ , \tag{5.4}$$

with the absorption of the device A_{device} and the transmission of the bulk heterojunction T_{BHJ}. The reflection can be at any interface. The largest amount of reflection will be at the air-substrate interface and at the metal-interface. For photon energies larger than the band gap, the percentage of photons absorbed in the active layer $\#p$ is the efficiency of photon absorption $\eta\left(\lambda\right)_{absorption}$ and is calculated by $T_{substrate}$ and R_{device} according to equation (5.5) and shown in Figure 5.11(b).

$$R_{device} = T_{substrate} \cdot T_{BHJ} \cdot T_{substrate}$$

$$\Rightarrow T_{BHJ} = R_{device} \cdot T_{substrate}^{-2} \tag{5.5}$$

$$\Rightarrow \#p = \eta\left(\lambda\right)_{absorption} = T_{substrate} \cdot \left(1 - T_{BHJ}\right)$$

The optical losses due to absorption and reflection of the semitransparent electrode is about 10%, each. The spectrum of absorption within the active layer is broad and relatively flat for $\lambda \lesssim 650nm$. The onset of this spectrum at $\lambda = 650nm$ is sharp. About 80% of the incident photons with $\lambda \lesssim 650nm\ (h\nu \gtrsim 1.9eV)$ are absorbed and converted to excitons.

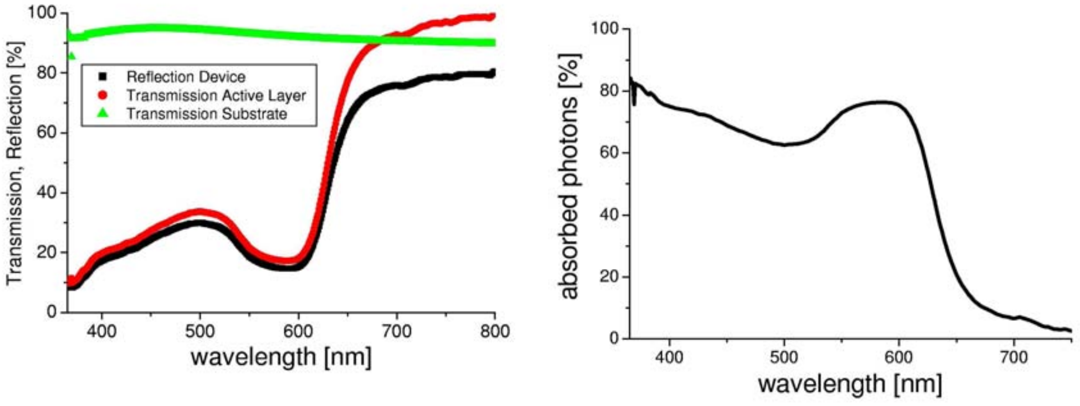

(a) (b)

Figure 5.11: (a) Reflection and transmission coefficient of the whole device (black), the substrate (green) and the active layer (red) and (b) the percentage of absorbed to incident photons.

5.1.3 Efficiency of the Generation of Free Charge Carriers

The efficiency of the charge generation $\eta_{generation}$ is the efficiency of the conversion of absorbed photons to free charge carriers and can be evaluated with the measurement of the external quantum efficiency (EQE), the calculation of the internal quantum efficiency (IQE) and the knowledge of the losses in the charge transport. The measurement and calculation of the IQE also provides information on the influence of recombination on charge transport.

The EQE is the ratio of the number of electrons extracted from the device to the number of incident photons. The EQE is measured according to section 3.3. The EQE summarizes the efficiencies of the processes of photon absorption $\eta\left(\lambda\right)_{absorption}$ charge generation $\eta\left(\lambda\right)_{generation}$, transportation and extraction $\eta_{transport}$:

$$EQE = \eta\left(\lambda\right)_{absorption} \cdot \eta\left(\lambda\right)_{generation} \cdot \eta_{transport} \,. \tag{5.6}$$

The EQE for a bulk heterojunction device is given in Figure 5.12. The spectrum is sharp with a maximum value of 76%, measured at $\lambda_{max} = 550nm$. The onset at $\lambda_{onset} \approx 650nm$ is steep. For a wavelength smaller than λ_{max} the EQE drops again to about 40%. With the EQE the expected short circuit current can be calculated, by folding the EQE spectrum with the spectrum of the photon density of the sun, to be $I_{SC} = 8mAcm^{-2}$.

In order to distinguish between absorption losses and internal losses the IQE is calculated. The IQE is the ratio of electrons extracted from the device to the number of photons absorbed in the active layer $IQE\left(\lambda\right) = \eta\left(\lambda\right)_{generation} \cdot \eta_{transport} = EQE\left(\lambda\right) / \eta\left(\lambda\right)_{absorption}$.

The result, as calculated from the EQE (Figure 5.12) and the absorption (Figure 5.11), is shown in Figure 5.13. The IQE shows like the EQE a sharp spectrum. The maximum value is 100% within the measurement accuracy of 10%. This value of 100% IQE shows, that both efficiencies, the charge generation efficiency and the charge transport and extraction efficiency can be as high as 100%. The efficiency of the charge transportation is not wavelength dependent, so this efficiency is 100% for every wavelength, which is in good

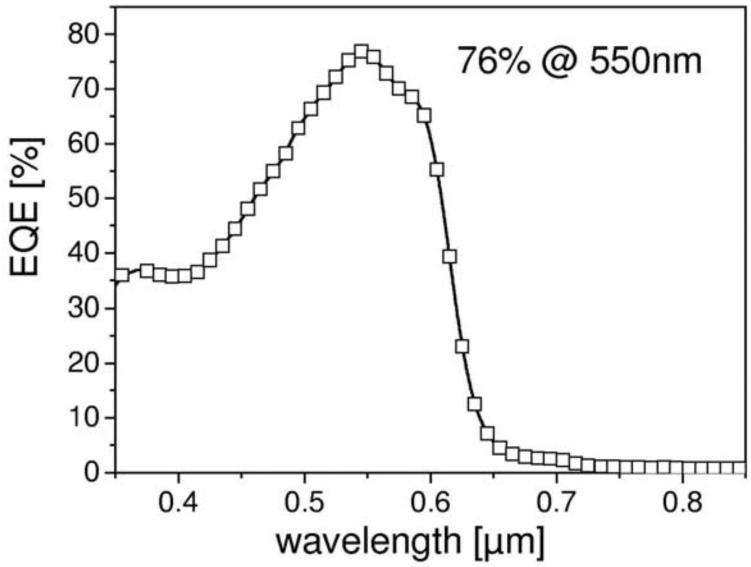

Figure 5.12: External quantum efficiency (EQE) for a bulk heterojunction solar cell (process#1, according to Table 2.1).

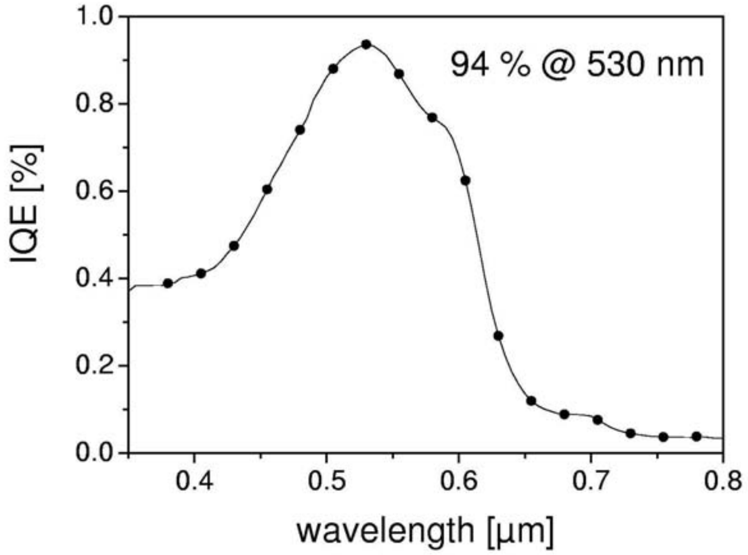

Figure 5.13: Internal quantum efficiency (IQE) spectrum for a bulk heterojunction solar cell (process#1, according to Table 2.1).

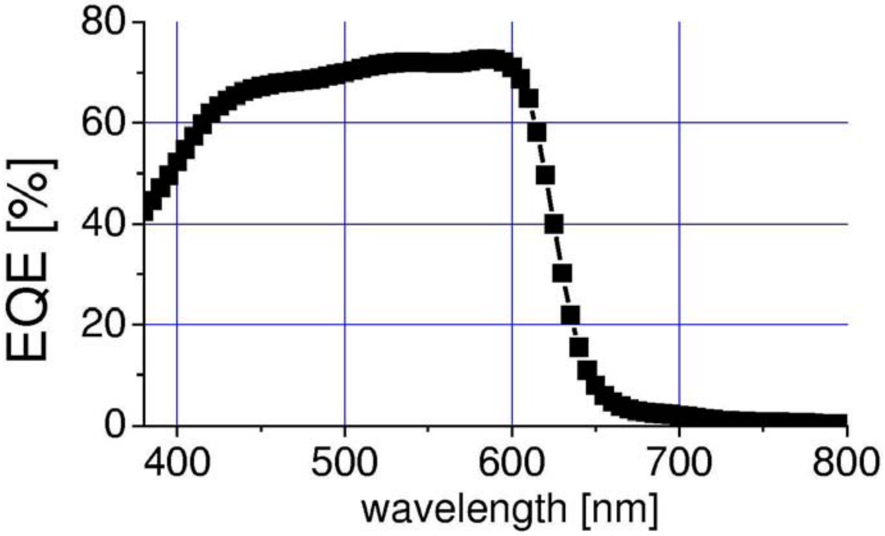

Figure 5.14: EQE spectrum of a bulk heterojunction with optimized morphology (process 2, according to Table 2.1).

agreement with the measurements of section 5.1.1. The drop in the IQE for shorter wavelengths is due to a decrease of the efficiency of charge generation $\eta_{generation}$.

This can be explained, because the two components have different absorption bands. At $\lambda = 500..650nm$ the absorption of the polymer is dominant, whereas for shorter wavelength both components attribute to the absorption and charge generation. Electron hole pairs generated at the polymer can be split without any loss. The generation efficiency is 1. Electron hole pairs generated at the electron acceptor are not separated with such high efficiency. They partly recombine before they are split. These measurement suggest that the size of the acceptor domains is larger than the diffusion length of electron hole pairs, which is for the used organic semiconductors in the order of $\approx 10nm$. An unfavorable morphology for the bulk heterojunction is formed.

If so, the charge generation efficiency should be influenced by the morphology of the bulk heterojunction. A variation in the production process, is known to change the morphology [10, 12]. A process variation is also tested in this thesis. A different morphology is also visible for the two processes (process #1 and #2, according to Table 2.1) and will be discussed in chapter 5.2.2. In Figure 5.14 the EQE spectrum for the changed process (process #2) is given. The EQE is flat for the whole absorption spectra $(\lambda \lesssim 650nm)$. The drop for $\lambda \lesssim 400nm$ is due to the measurement setup. Both components contribute efficient to the charge generation.

5.1.4 Summary of the Photon to Electron Conversion Analysis

In this section, the efficiencies and losses of the single steps of the photon to electron conversion were investigated. This efficiency is the product of the single efficiencies of the photon absorption, charge generation, charge transport and extraction. These efficiencies are particle-efficiencies, not taking in to account any energy loss of the single steps.

Losses due to reflection or absorption of the substrate are each in the order of 10% for the visible light. The spectrum of the ratio of in the active layer absorbed photons to incident photons is broad with a value of about 80% for wavelengths $\lambda \lesssim 650nm$. About 20% of the photons, with sufficiently high photon energy, are not absorbed in the active layer.

The charge transport is loss free within the measurement accuracy. The drift length is about 0.5μm and larger than the sample thickness. The majority of the carriers are able to cover a larger distance than the active layer, before they recombine. The charge transport has an efficiency of 1.

The transport mechanism, which is supposed to be either hopping or trapping-de-trapping, could not be revealed with the transient photocurrent decay measurements.

In case of loss-free charge carrier transport, the IQE directly represents the spectrally resolved charge generation efficiency. The generation of free charge carriers is found to be wavelength dependent: charges generated on the polymer are split with an high efficiency; charges generated on the electron acceptor are separated less efficient. The latter partly recombine before they reach the interface, where they can be separated. The diffusion length of electron hole pairs is lower than the average size of the acceptor domains.

Two different losses could be distinguished. The optical losses due to absorption and reflection of the device substrate and the losses due to insufficient charge separation of charges generated on the acceptor. The optical losses could be reduced by light harvesting, e.g. antireflection coatings, but no tests were done for reducing these losses. The charge generation efficiency is influenced by the morphology of the bulk heterojunction. By variation in the process, the EQE can be improved in the absorption range of the bulk heterojunction, as shown in Figure 5.14. Both components contribute efficiently to the charge generation.

With this set of measurements, discussed in this section 5.1, it is possible to detect the efficiencies and losses in the single steps of the photon to electron conversion. For this material combination, the efficiency of the photon to electron conversion could be enhanced.

5.2 The Open Circuit Voltage V_{OC}

The open circuit voltage V_{OC} is one of the efficiency controlling parameters for solar cells. The maximum limit for the V_{OC} is the difference of the LUMO of the electron acceptor and the HOMO of the electron donor. However, the measured values for V_{OC} are always lower. The origin of lower V_{OC} values will be examined in this section.

Under illumination the quasi Fermi levels for electrons and holes are split. The extend of this splitting is dependent of the illumination intensity [48], the higher the light intensity, the larger the carrier density, the higher the difference of the quasi Fermi levels, approaching the maximum of the energy gap between the LUMO to the HOMO level. The difference of the quasi Fermi levels determines the built-in voltage V_{bi}. The flat-band voltage V_{FB}, the voltage where the driving field is zero, can be lower than the built in voltage V_{bi}. As shown before, the driving force for the carriers is the field $E = \frac{V_{FB}}{L}$ and a bending of the bands can be neglected. So the voltage for the driving field V_{FB} should be close to the built-in voltage.

A lowering of the V_{OC} in respect to the V_{bi} can be understood by analyses of the shape of the curve, due to the diode behavior and losses due the parallel and serial resistance R_P and R_S, respectively.

In this section the influence of the diode parameters, on the V_{OC} will be examined and tested.

5.2.1 Influence of the Parameters of the Macroscopic Model on the V_{OC}

The influence of the single parameters of the macroscopic simulation on the V_{OC} and the maximum power point will be discussed in this subsection. For this discussion the macroscopic simulation is used and the expected V_{OC} and efficiency are calculated for a variation of pairs of simulation parameters, keeping the other simulation parameters fixed.

The field dependent carrier extraction of the macroscopic simulation is one crucial prerequisite, which makes the fitting of IV-curves for different illumination intensities, with one set of parameters possible. The parameters for the current source added to the one-diode equation (equation (4.4)) are the flat-band voltage V_{FB}, the carrier mobility and carrier lifetime (equation (4.6)). These parameters are material parameters and not easy changeable. Also the potential of these parameters on increasing the V_{OC} is small (Figure 5.15).

The largest impact is from the dark diode itself. The V_{OC} is the point, where the current of the dark diode I_{dark} is equal to the added light generated current $I_{photogenerated}$. The influence of the resistances R_s and R_p is small, because around V_{OC} just low currents are flowing. Just for extreme unfavorable values for R_S and R_P their influence may become important. In contrast, the influence of the diode parameters ideality n and saturation current I_0 is large. The smaller I_0, or the larger n, the higher is V_{OC} (Figure 5.15). By varying these parameters, the flat-band voltage used in the simulation can be nearly reached, which was not possible with a variation of μ, V_{FB}, R_S or R_P.

5.2.2 Influence of the Macroscopic Model on the V_{OC}

The macroscopic simulation predicts a strong influence of the parameters n and I_0 on the open circuit voltage V_{OC}, which will be tested in this subsection. First, possible relations of these parameters to physical attributes of the bulk heterojunction will be explained. Based on these links between the model parameters and process parameters, experiments on intentional changing of n and I_0 will be shown and the resulting dependence of V_{OC} will be discussed.

The saturation current I_0 is discussed in classical semiconductor literature, where it is expressed in terms of the barrier height, diffusion length or carrier and doping concentration, depending on the type of junction [48]. As the bulk heterojunction is no classical junction, no defined dependence of the saturation current on these parameters can be given.

The only properties of I_0 taken from the classical semiconductor literature is its dependence on the charge carrier concentration. With doping or de-doping it may be possible to change I_0, and if this assumption is correct also the V_{OC}.

The ideality n is understood as representing the morphology of the bulk heterojunction. An ideality of $n = 1$ represents an ideal flat pn-junction. As the bulk heterojunction is by definition a distributed pn-junction, this distribution is expected to be represented by the ideality of the diode. An ideality of $n > 2$ could, for example, mean, that there are two or more diodes in series. An ideality of $n = 2$ is also discussed as a Shockley-Read-Hall-recombination. The interpretation of the ideality factor is difficult and an exact correlation of a given value of the ideality factor with the morphology is not possible, but changes

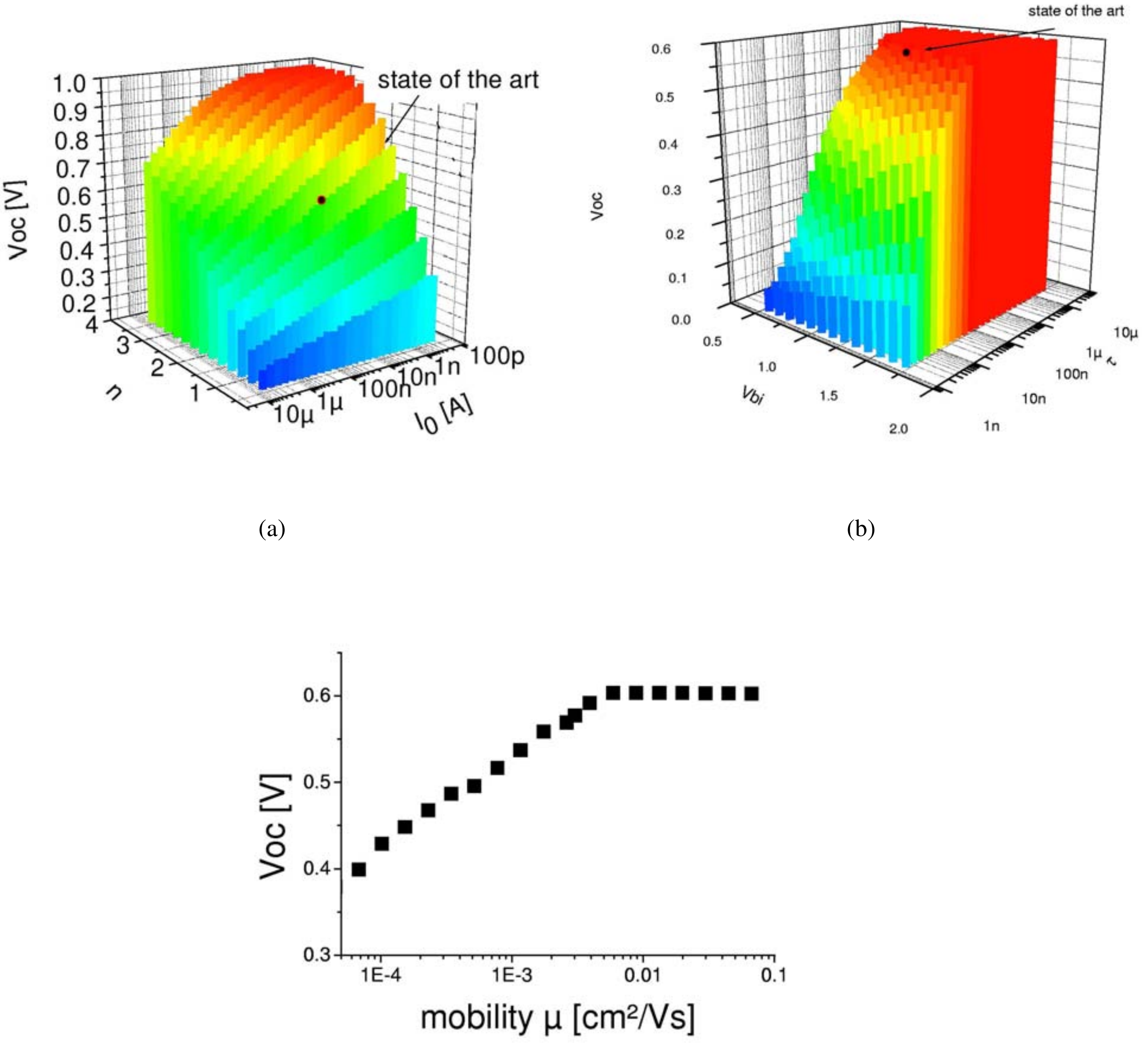

(a) (b)

(c)

Figure 5.15: V_{OC} vs. a) n and I_0, b) τ and V_{bi}, c) μ as calculated out of the macroscopic simulation. The color in a) and b) is correlated with the value of each measurement point as a guide for the eye. The simulation started with the fitted parameters $n = 1.7$, $I_0 = 1.8{\cdot}10^{-8}A$, $\mu\tau = 5.5 \cdot 10^{-10}cm^2V^{-1}$, $V_{bi} = 1.1V$, $R_s = 1.6\Omega$, $R_{p,dark} = 230M\Omega$, active area: $4mm^2$, $L = 200nm$.

Dopant concentration	Process #	Conductivity	I_0 [nA]	V_{OC} [V]
0	#1		47	0.55
0	#3	$4.5 \cdot 10^{-3} \frac{S}{m}$	4	0.62
0.0001%	#3	$1.1 \cdot 10^{-3} \frac{S}{m}$	6	0.61
0.001%	#3		10	0.59
0.01%	#3	$0.9 \frac{S}{m}$	19	0.52

Table 5.1: Overview on the doping concentration and results for the experiment with doped and purified polymers.

in the ideality factor are expected to refer to a different morphology and a change in the morphology should change the ideality factor. An influence of the morphology on the open circuit voltage is also discussed in [24].

5.2.2.1 The Saturation Current I_0

The intentional changing of I_0 was done by comparing the reference system (process#1, according to Table 2.1), with samples made from a cleaned polymer (process#3) and with samples made from the cleaned polymer, in which a dopant $2,3-dichloro-5,6-dicyano-1,4-benzoquinone$ - (DDQ) was added to the solution, during the solution preparation. The dopant was reported to dope poly-alky-thiophene (PAT) via a charge transfer, where the dopant acts as an electron acceptor. The creation of free charges, polarons and bipolarons is reported [71]. With the addition of $FeCl_3$ or DDQ to the polymer solution two additional absorption bands occur at $\approx 0.5eV$ and $\approx 1.5eV$. The conductivity of doped films is increasing with increasing dopant concentration [72]. However, doping with $FeCl_3$ is reported to lead to degradation of PAT-films [73] and was therfore not investigated here.

The saturation current was investigated in samples made of the reference process#1, the purified polymer (process#3) and in samples made of the purified polymer with the dopant DDQ added to the polymer solution in various concentrations (process#3 + dopant). The cleaned polymer should have a significant lower I_0 than the reference polymer, as discussed above in the introduction of this subsection 5.2.2.

Polymer solutions without the dopant and with various dopant concentrations were produced (Table 5.1). From this solutions films were prepared and the conductivity of these films are measured. The conductivity is rising over 3 orders of magnitude, by variation of the dopant concentration from 0% over 0.0001% to 0.01% in the solution.

With these polymer solutions bulk heterojunction solar cells were produced and the saturation current and open circuit voltage analyzed (Figure 5.16 (a) and Table 5.1). The cells made of the purified polymer show the lowest I_0. The I_0 is increasing with increasing dopant concentration in the polymer solution. The highest saturation current is measured for the reference polymer. The open circuit voltage is decreasing with the increase of the doping concentration (Figure 5.16 b). And the V_{OC} is increasing with decreasing I_0, for all samples beside the reference sample. The origin of the higher V_{OC} for the reference polymer is due to a change of the ideality factor and a higher I_{SC} at the same time.

By doping or de-doping (purifying) of the polymer it is possible to intentionally increase the open circuit voltage or decrease the V_{OC} of the bulk heterojunction solar cells, respec-

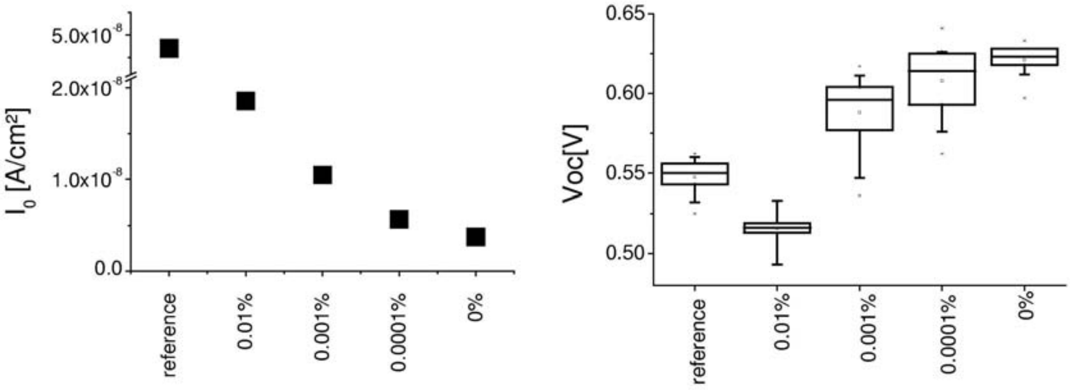

(a) (b)

Figure 5.16: (a) The saturation current I_0 vs. dopant concentration in the solution and (b) V_{OC} vs. dopant concentration inside the solution. The dopant is added to the solution of a purified polymer. Bulk heterojunction solar cells are made of these solutions and the values for V_{OC} and I_0 are evaluated. As comparison the values for samples made by the reference polymer are shown. In (b) the data are presented in box plots, which are a statistical evaluation of about 15 measurements on single samples. The horizontal lines in the box denote the 25th, 50th and the 75th percentile values. The error bars denote the 5th and the 95th percentile values. The open square in the box is the mean value of the measurement series. The two symbols below and above the 5th / 95th percentile error bar denote the highest and the lowest observed values, respectively. For (a) and (b), the reference process#1 is shown as comparison.

tively. The dependence of the open circuit voltage on the saturation current is shown for this sample series with purified and intentional doped polymer. Unfortunately, for the purified polymers used here, the overall efficiency is lower than for the reference polymer. This is mainly due to a lower I_{SC} for solar cells made of the de-doped polymer. This is regarded to be due to a change of the morphology for the de-doped polymer. The complete I_{SC} - analysis was not done for cells made of the purified polymer.

5.2.2.2 The Diode Ideality Factor n

A change in the process, e.g. a variation of the solvent, is reported to have a large influence on the morphology of the bulk heterojunction [10, 12]. Hence, it should also have an influence on the ideality of the dark diode n, if the assumption stated above is correct. This will be tested in here.

First the influence of the process on the morphology is tested. Films made by two different processes (process#1 and process#2, according to table 2.1) were tested and measured with the atomic force microscope (AFM) (Figure 5.17), as well as in a device. The AFM-measurements show a different grain size as well as a different height scale for these two processes. A change in morphology of the surface is visible.

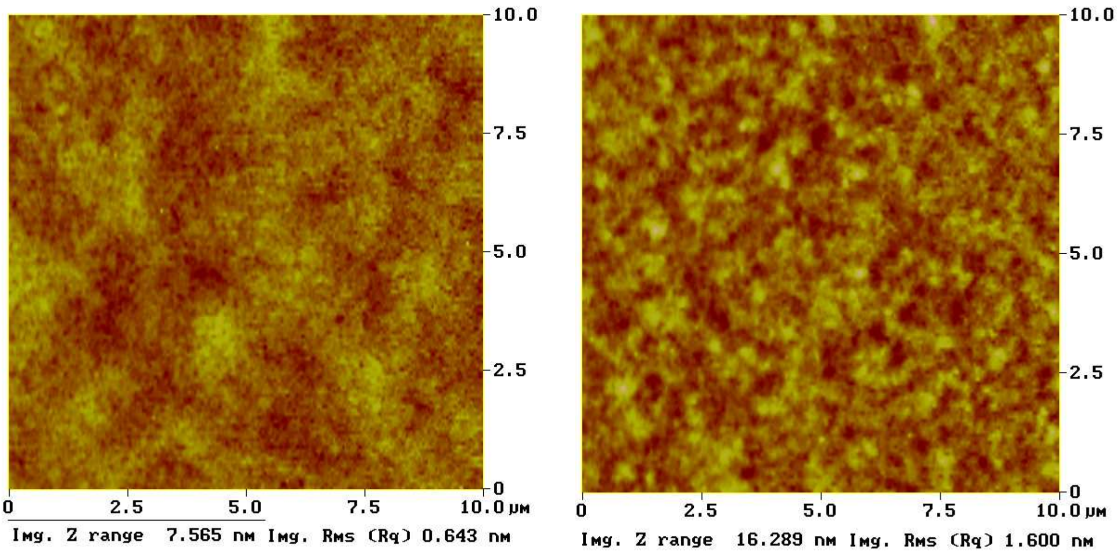

(a) (b)

Figure 5.17: Comparison of AFM-measurements on films made by two different processes with the z-range and the RMS-roughness analysis for each measurements. (a) shows the reference process (process#1) and (b) the optimized process (process#2).

The influence of the process on the ideality is visible when comparing the ideality of samples prepared by these processes (Figure 5.18). Comparing the first and the second process, n is increased from $n \approx 1.8$ to $n \approx 2.0$. At the same time, the saturation current I_0 is lowered from $I_0 \approx 55nAcm^{-2}$ to $I_0 \approx 2nAcm^{-2}$, a larger variation than that with changing the polymer from the reference to the de-doped polymer. The correlation of n and I_0 with the V_{OC} can be seen in Figure 5.18(b), but not as pronounced as predicted by the macroscopic simulation. The simulation predicted a larger increase of V_{OC}, because n is increased and I_0 is decrease at the same time.

For the variation in the process the diode parameters n and I_0 are changed and the V_{OC} can be increased by this change. The correlation of the morphology with the ideality could be verified. With this morphology change it was possible to obtain a higher I_{SC} at the same time (Figure 5.14 in section 5.1.4).

5.2.3 Discussion

In this section the relevant parameters influencing the open circuit voltage V_{OC} were determined to be n and I_0. This influence can be verified by controlled doping and de-doping of the polymer solution and by changing the morphology via the process. It was not possible to change only one of the diode parameters.

The morphology has the larger impact on the V_{OC} and on the efficiency enhancement than the background doping concentration. The macroscopic simulation shows that the values n and I_0 of the optimized process are nearly the optimum values for the power conversion efficiency (Figure 5.19) and no further enhancement of the efficiency is possible.

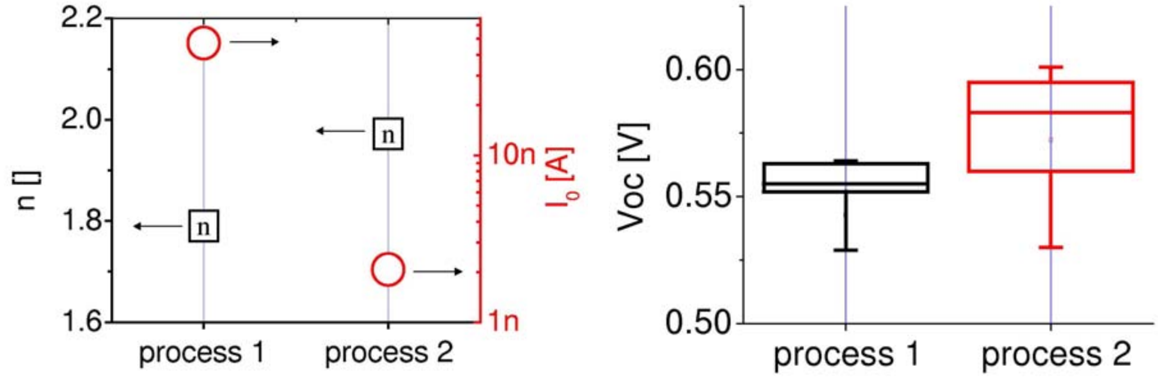

Figure 5.18: a) The values for n (black boxes with n) and I_0 (red, open circles) for solar cells, made by two different processes (number 1 and 2, as given in Table 2.1), changes with the variation in the process. b) The open circuit voltage V_{OC} increases when changing from process 1 to 2. In b) the data are presented in box plots, which are a statistical evaluation of about 15 measurements on single samples. The horizontal lines in the box denote the 25th, 50th and the 75th percentile values. The error bars denote the 5th and the 95th percentile values. The open square in the box is the mean value of the measurement series.

Losses originating from the difference of the built-in voltage to the flat-band voltage are not analyzed here, because the uncertainty of the values for the HOMO and LUMO of the polymer and fullerene are large (see chapter 2.2), so that the extent of this loss is not clear.

5.3 The Fill Factor ff and the Photoshunt

In this section, the influence of the parameters of the macroscopic simulation on the fill factor ff will be investigated. Based on these findings, the relevant parameter will be examined and tests for improvements are done.

5.3.1 The Relevance of the Single Parameters of the Macroscopic Simulation on the Fill Factor

In contrast to the I_{SC} and the V_{OC}, the fill factor is an artificial factor, representing the diode parameters n, I_0 and the resistances. The macroscopic simulation is used for calculating the expected fill factor and efficiency. The relevance of the simulation parameters (n, I_0, V_{bi}, $\mu\tau$, R_p and R_s) will be evaluated by varying pairs of simulation parameters, keeping the other simulation parameters fixed.

The results are shown in Figure 5.20. The fill factor as a function of n and I_0 forms a saddle. The influence of the diode parameters n and I_0 on the fill factor is opposite to the dependence of the V_{OC} on the same parameters. Therefore the efficiency can nearly not be further increased (Figure 5.19), even if the fill factor could be higher.

The two resistances R_s and R_p show an expected influence on the fill factor: the higher the parallel resistance R_p and the lower the series resistance R_s the higher the fill factor.

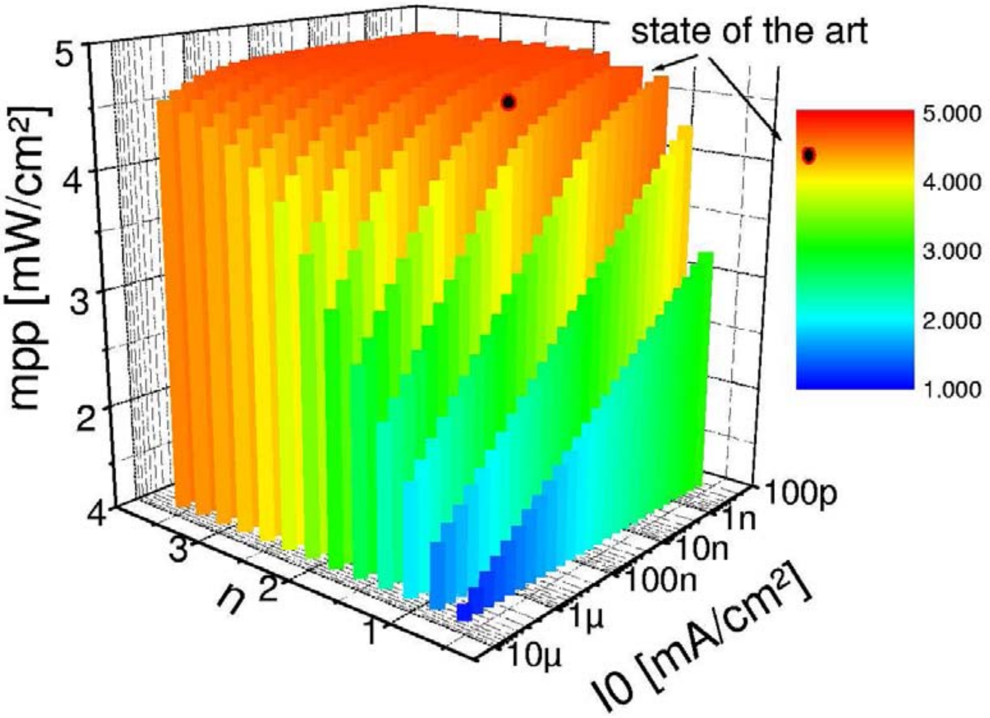

Figure 5.19: The maximum power point mpp vs. n and I_0 as calculated from the macroscopic simulation. The color is correlated with the value, as a guide for the eye and shown in the legend. The black circle marks the coordinates for the optimized process#2.

The series resistance is already on the limit and has no potential for further optimization of the fill factor. The parallel resistance still has a huge potential for a fill factor and efficiency optimization, as shown in Figure 5.20 (a) and (b).

The influence of the $\mu\tau$ - product on the fill factor is only visible for unfavorable values of the $\mu\tau$ - product (Figure 5.20 d). It is possible to decrease the fill factor with too low values of the $\mu\tau$ - product, but it has no potential for further optimization of the fill factor.

Hence, we conclude, the parameter, with the highest potential for an optimization of the fill factor and efficiency is the parallel resistance. Optimization and investigation of the R_p will be done in the next paragraph.

5.3.2 Variation of the Shunt with the Illumination Intensity: the Photoshunt and its Origin

In this subsection, the origin of the shunt under illumination is investigated and experiments for reducing the shunt are discussed.

When comparing the values for the shunt R_p in the dark and under illumination, a decrease of the shunt with illumination can be seen. A test series with different bottom electrodes, where the shunt in the dark was varied over 3 orders of magnitude, showed, that the

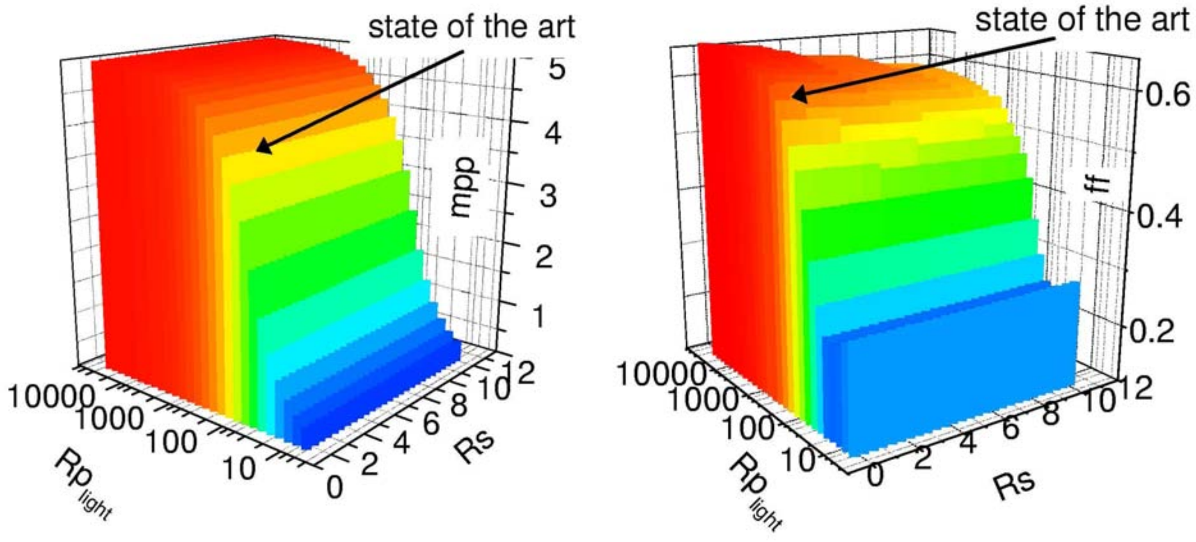
state of the art
mpp
5
4
3
2
1
10000
1000
100
10
Rp light
0
2
4
6
8
10
12
Rs
state of the art
ff
0.6
0.4
0.2
10000
1000
100
10
Rp light
0
2
4
6
8
10
12
Rs

(a) (b)

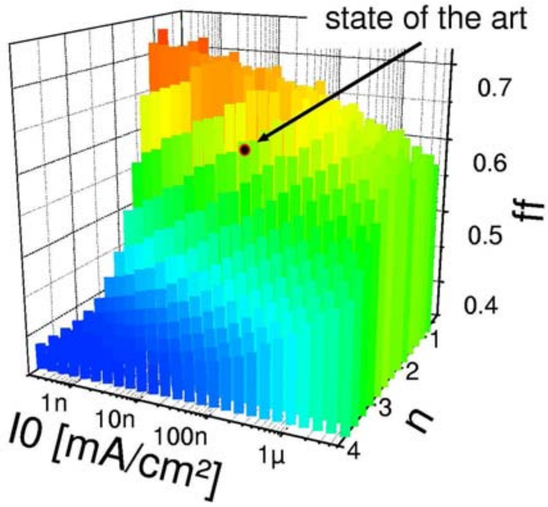
state of the art
0.7
0.6
0.5
0.4
ff
1
2
3
4
n
1n
10n
100n
1µ
I0 [mA/cm²]

(c)

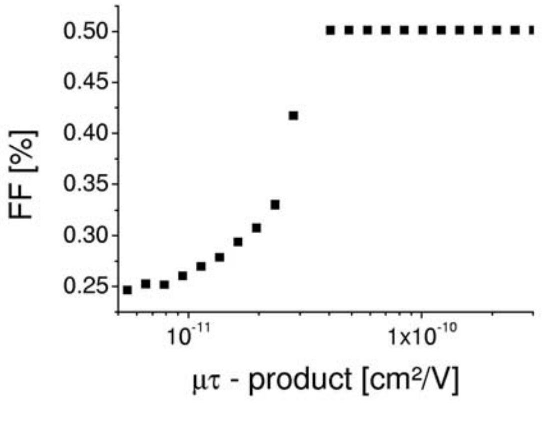
0.50
0.45
0.40
0.35
0.30
0.25
FF [%]
10-11
1x10-10
µτ - product [cm²/V]

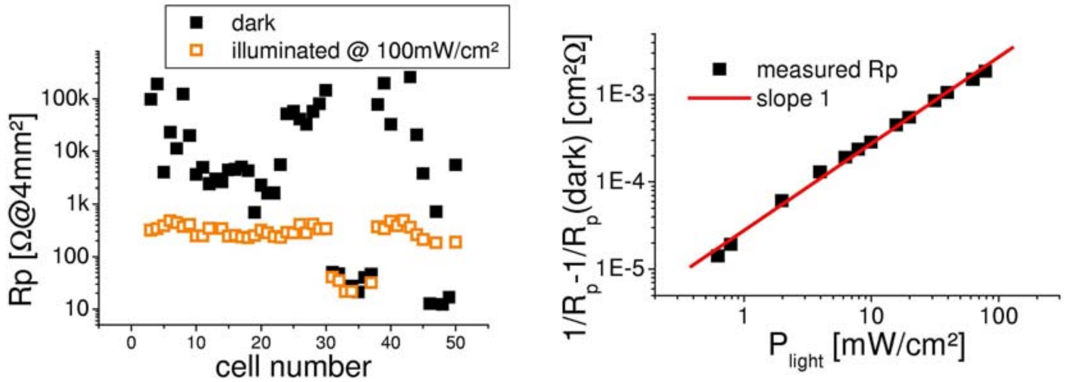

(a) (b)

Figure 5.21: Dependence of R_P on light intensity. a) Given is the value for the R_p in the dark (closed squares) and under illumination with $100mWcm^{-2}$ (open squares) for an experiment series with different bottom electrodes. This variation of the bottom electrodes gives a large variation of the R_p in the dark. This variation of dark R_p has nearly no influence on R_p under illumination. b) The value of the photoconductivity vs. the light intensity (boxes) in a double logarithmic representation and a line with slope 1. The photoconductivity is proportional to the illumination intensity.

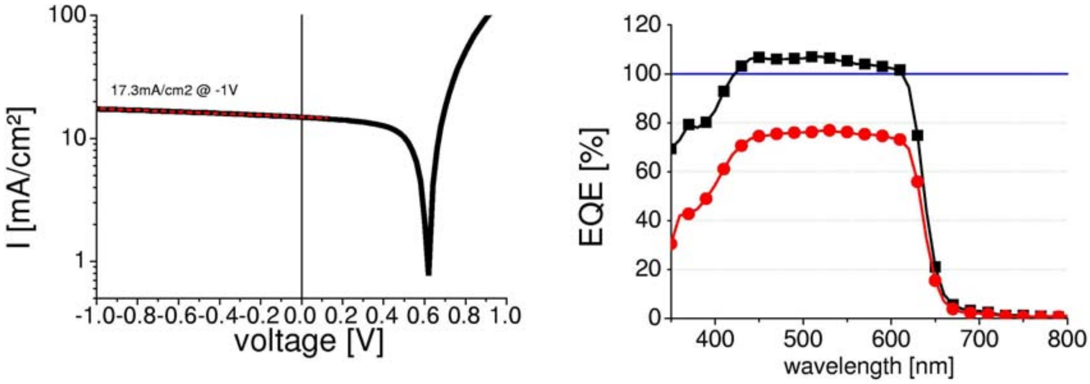

(a) (b)

Figure 5.22: a) IV curve, measured until $-1V$. The slope, representing the photoshunt, can be seen up to high voltages and current (red line). If the slope would be due to a field dependent charge extraction, the maximum light generated current would reach about $17mA/cm^2$. For this current an EQE above 100% would be necessary which is also measured (b) when going from $0V$ (circles) to $-4.8V$ reverse bias (squares) .

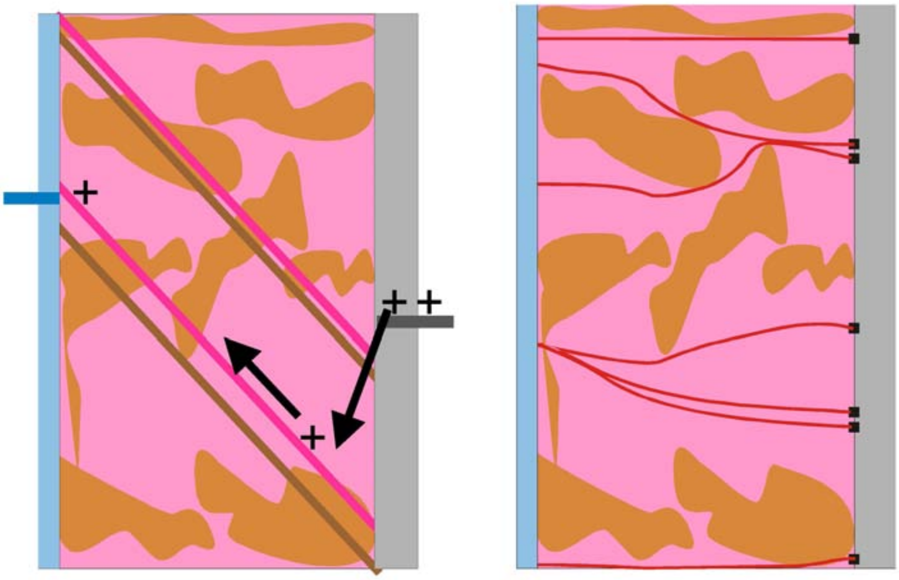

(a) (b)

Figure 5.23: Two possible scenarios for explaining the photoshunt in the bulk heterojunction, as shown in Figure 1.1: (a) The band diagram is given for reverse bias. One contact has a non zero probability to inject carriers in both materials, e.g. the metal injects holes into the polymer (additionally to injecting into the PCBM, which is allowed). (b) Conduction paths are contacting the top and bottom electrodes. A part of the area of the contact is failing and forms an ohmic contact with the both materials. In both scenarios conductive paths from one electrode to the other are formed.

shunt under illumination is always at one level (Figure 5.21). The shunt under illumination is independent of the value of the shunt in the dark. Therefore the value of the shunt under illumination, which is the important one for solar cell efficiency, can not be due to the typical shunting mechanism, due to imperfections in the semiconductor layer leading to direct connection of one electrode to the other.

A reduction of the shunt is equivalent to an increase of the conductivity in reverse direction. The additional contribution to conductivity in reverse direction is proportional to the light intensity (Figure 5.21) and because the carrier density is proportional to the light intensity, the conductivity is proportional to the carrier density. This is the normal characteristic of photoconductivity of a single material, according to equation (5.7)

$$\sigma_{light} = n \cdot \mu \cdot E\,. \tag{5.7}$$

The change of the slope in reverse direction under illumination can not be the field driven charge extraction, where the additional current is due to an increase of the extracted photogenerated current. Figure 5.22(a) shows that at $-1V$ bias the current is already $17mAcm^{-2}$ which is a too high current to be explained by the absorption of the used materials. An EQE above 100% was measured under reverse bias (Figure 5.22b). The EQE is measured using lock-in-technique, therefore this value is corrected for the dark current due to the dark shunt. Such high value of the EQE can be only explained with the extraction of primarily photo-generated carriers additional to injected and conducted carriers, where either the injection or the conduction has to be light dependent. The conductivity in reverse is linear with the light intensity, which can not be easy explained with a light dependence of the injection, but with the simple model of photoconduction in one material.

The interpretation of the reduction of the shunt resistivity is a photoconductivity in the reverse direction. This means, that one of the electrodes is failing. Therefore one material can form an ohmic contact with both electrodes and conductive paths are formed between both electrodes via one of the bulk materials (polymer or fullerene). This failure of the electrode can be explained with two scenarios (Figure 5.23), where the assumption is made, that the top electrode is the failing electrode: First scenario is an injection of holes from the top electrode into the HOMO of the polymer under reverse bias. There is a non-zero-probability for this injection and the injected carriers can than be transported via the polymer to the bottom electrode. The second scenario is, that a part of the top electrode fails and forms an ohmic contact to the polymer. From this parts the carriers are conducted via paths to the other electrode.

Both scenarios have the prerequisite of interpenetrating paths of one material, from one electrode to the other. Both scenarios have a probability factor for the failure of the electrode. With an insertion of a hole blocking layer at the top electrode or an electron blocking layer at the bottom electrode, it should be possible to reduce this probability factor and to increase the R_p under illumination. Such tests are performed and the results (Figure 5.24) show that the slope in reverse direction is lowered with the insertion of the extra blocking layers and the value of the shunt R_p is doubled for samples with blocking layer in comparison to the reference samples.

The fill factor can only be increased for samples with the top hole-blocking layer and not for the electron blocking layer (Figure 5.24c). This is a hint that the top electrode partly fails and the polymer is the photo-conducting material.

The shunt, which is the parameter with the highest optimization potential for the fill factor, is light dependent. The IV-curves in reverse direction show a photo-conductivity, beside the extraction of photo generated carriers. This could be explained by continuous paths of one electrode material to the other via one of the absorber materials. With the insertion of hole blocking layers the shunt resistance and the fill factor could be increased.

5.4 Discussion

In this chapter a set of experiments and evaluation methods were shown, which allowed an analysis of loss mechanisms and efficiencies of the processes of the energy conversion.

The zero bias experiments, allows to probe the efficiencies of the single steps of the photon to electron conversion process: charge generation, separation and transport. For the analyzed system, a loss in the charge separation was observed. Excitons generated on the electron acceptor were not separated without loss. This could be explained by too large domain size of the electron acceptor and by changing the morphology the loss could be reduced. Further deficiencies are due to the material combination used for the bulk hetero-junction: the absorption spectra of the polythiophene and the fullerene allow no absorption for photons with energies below $h\nu < 1.9eV$, due to the bandgap of the polymer.

The extended one-diode equivalent circuit allowed to determine losses in fill factor and

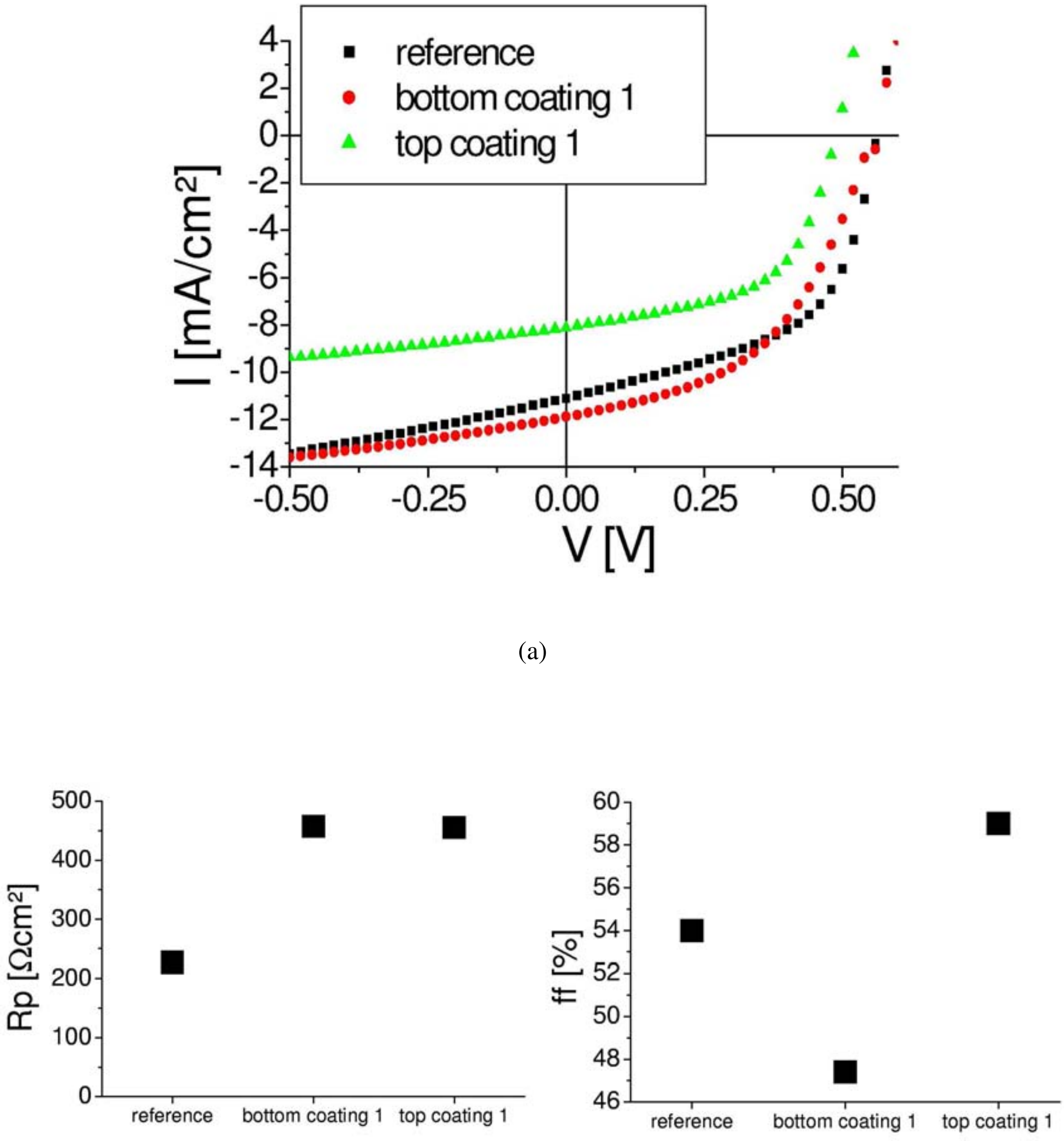

(a)

(b)

(c)

Figure 5.24: (a) IV-curve for the reference cell (black) and for the cell with inserted hole blocking top (green) and electron blocking bottom layer (red) . (b) The value for the R_p for the reference and the additional top and bottom coatings. (c) The fill factor for the reference samples and for samples with additional bottom and top coating.

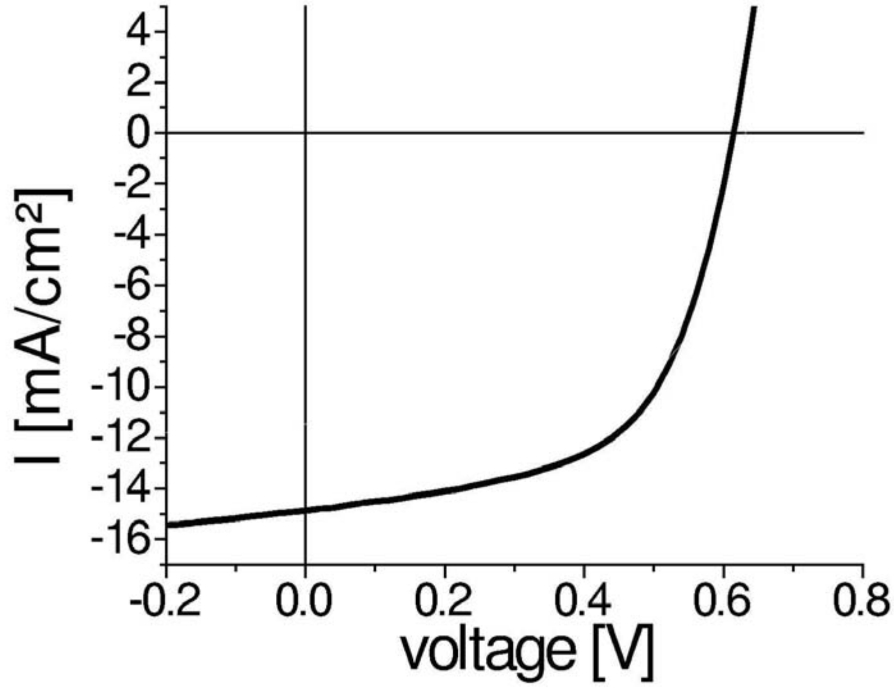

Figure 5.25: IV-curve, measured on optimized sample. The efficiency parameter of these optimized cells are in the range of: $I_{SC} = 11..15 mAcm^{-2}$, $V_{OC} = 610..630 mV$, $ff = 58..65\%$, $\eta = 4.7..5.2\%$. These parameters are for illumination with $100 mWcm^{-2}$ $AM1.5$ simulated light, without correction for the spectral mismatch.

in the V_{OC} in comparison to the flat-band voltage V_{FB}. Losses in V_{FB} in respect to the built-in voltage V_{bi} could be due to the contacts, but were not investigated here. Losses in the V_{bi} due to the energetic levels of $LUMO - HOMO$ are due to the used material combination. No tests and investigation regarding these losses were done. The open circuit voltage is influenced by the diode parameters $n,\ I_0$. The saturation current density I_0 could be influenced by the impurity density and the morphology. The ideality was shown to vary with the morphology. The morphology has larger influence on the reference system than a change of the impurity density. The expected dependence of the open circuit voltage with the diode parameters could be verified. With the change of the morphology an increase in both the V_{OC} and the I_{SC} was demonstrated.

The fill factor is limited by the photoshunt. The photoshunt is the effect of a decrease of the shunt resistance with the illumination intensity. Measurements regarding the photoshunt led to the interpretation of the photoshunt as a photoconductivity in the reverse direction. This photoconductivity is due to conductive paths in one material from one electrode to the other, where one of the electrodes is partially failing and injecting carriers into the wrong material. With the insertion of a hole blocking layer between the active layer and the top contact, the photoshunt can be reduced and the fill factor increased. The expected dependence of the fill factor with the shunt resistance could be verified.

With this loss analysis it was possible to determine the relevant loss mechanisms. The losses for the efficiency parameters I_{SC}, V_{OC} and fill factor are determined. The loss in the I_{SC}, representing the product of the single conversion steps, charge absorption, separation, transport and extraction, is determined to be in the charge separation. The open circuit voltage can be increased by improving the morphology, which led to a more favorable diode ideality n and saturation current density I_0. The fill factor is limited by the photoshunt. By reducing these losses the overall efficiency can be increased to white light efficiency of over 5% (Figure 5.25), the highest value for polymeric bulk heterojunction solar cells reported so far.

Chapter 6

Degradation

In this chapter the loss evaluation procedure introduced in chapter 5 is used for analyzing ageing effects of solar cells performed under different test conditions[1]. First, possible parameters for accelerating the degradation are evaluated. In the second section, the accelerated degradation is analyzed with the methods introduced in chapter 5 to determine the degradation mechanisms.

Organic based solar cells have the potential to be significantly cheaper produced than conventional semiconductor solar cells, while offering at the same time high environmental compatibility of the production process. However, experience gained during the development of comparable organic technologies like the OLED (organic light emitting diodes) technology shows that lifetime and stability is a major issue for all organic opto-electronic devices. High quality semiconductor processing, packaging and sealing is required for stable devices, and in the meantime lifetimes exceeding by far the required 25.000 hours have been achieved for the OLED technology.

Operational stability is one of the key parameters for solar cells, being decisive for the rentability. A simple rule is that the produced $W \cdot h$ (operational hours) multiplied by the energy costs must match the production costs of the device. Under the assumption that the EURO/Wp costs of organic solar cells will be less than 1/4 of inorganic solar cells, lifetimes in the order of at least 5 years are required for organic solar cells.

Better control and understanding of the parameters limiting the lifetime is necessary. Thus, it is of importance to establish a fast and reliable routine for the lifetime analysis of organic solar cells, allowing evaluating and predicting the quality and stability of novel semiconductors, electrodes and packaging materials.

As method to study the lifetime of polymeric solar cells we discuss the suitability of temperature accelerated lifetime analysis and current accelerated lifetime analysis to determine the opto-electrical stability of the conjugated polymers. In the first section, the acceleration constants $K(T)$, $K(P_{light})$ are determined. In the second section, the degradation mechanisms are analyzed.

---

[1] Part of this work is published in [74]

6.1 Accelerated Life Time Analysis

6.1.1 Introduction to Accelerated Life Time Analysis

Accelerated life time analysis is a traditional tool to predict failure correlated to specifically selected stress. Normal life time testing involves analyzing times-to-failure data (of a product, system or component) obtained under normal operating conditions in order to quantify the life time characteristics of the product, system or component. In many situations, and for many reasons, such life data (or time-to-failure) are very difficult, if not impossible, to obtain. Another limiting factor is the time required for testing, which can, in the case of solar cells, exceed 20 years, and finally, the complexity of selective component testing in an integrated product motivates the need for a fast and selective life time analysis and prediction. Due to these reasons and due to better understanding of single component as well as complete product failure modes, accelerated life testing has become popular over the years.

ALT is used to quantify the life characteristics of the product, component or system under overstress conditions. Products like an organic solar cell are expected to perform their functions successfully for long periods of time, typically for years. Obviously, for a producer to remain competitive, the time required to obtain times-to-failure data must be considerably less than the expected life of the product. Further, ALT is used to analyze failure of components under overstress conditions. Overstress acceleration is also used in degradation measurements presented in this work. The most common accelerated tests conditions are:

- High temperature and/or temperature cycling and/or temperature gradients
- Power cycling / voltage cycling / power extremes / voltage extremes
- Humidity
- Radiation
- Mechanical shock and stress/ vibrational tests / creep-stress relaxation tests.

Some of the accelerated test equipment enables to carry out a combination of these tests. For instance, temperature/humidity test (typically $85°C$ / $85\%\, RH$) are frequently used for electronic components and products, while illumination/temperature is a popular couple for material testing. As the accelerated test conditions for the organic solar cells discussed in this work, temperature and illumination is selected, aiming to investigate material stability of the semiconductor and the electrodes respectively. Acceleration or stimulation of the failure mechanism is performed at various temperatures ($40..95°C$) and under constant illumination of approximate 1/3 sun, and under constant temperature $T = 85°C$ and various illumination. Illumination was provided by standard halogen lamps, no additional measurements were taken to block the UV part.

6.1.2 Determination of Degradation Constants

6.1.2.1 Accelerated Life Test Models

Qualitative ALT demands a life test model to correlate the specific accelerated stress to a device or material parameter. It is expected that an accelerated life test model is simple enough, yet meaningful, to investigate the specific device in question. A good life test model should be suitable to account for the role of materials, structures, environmental conditions, etc. Some major ALT models frequently used for electronic components are the Arrhenius Equation, the Eyring Equation and the Power Law. The single models are introduced in more details below.

One of the most frequently used models is the Arrhenius-Model, which is derived for processes with first order kinetics. The degradation constant for this model is defined by Equation (6.1)

$$k_{deg} = A \cdot exp\left(\frac{-E_a}{k_B T}\right) \tag{6.1}$$

Here, E_a is the activation energy in eV, k_B the Boltzmann constant $8.62 \cdot 10^{-5} eVK^{-1}$, T the temperature and A is a constant dependent on the degradation mechanisms and the experimental conditions. Typical processes properly described by the Arrhenius model are material related, like the trapping behavior of charge carriers or structural and chemical changes of polymers. All these processes have in common that a certain activation energy E_a has to be overcome. Thus, the kinetics of these processes is strongly temperature dependent.

An extension of the Arrhenius model is the Eyring model, which takes into account different influences than temperature. In the case of solar cell or photodetector degradation, this could be for instance the light intensity or the applied bias. The acceleration factor is given by equation (6.2)

$$k_{deg} = A \cdot T^{\alpha} exp\left[\left(\frac{-E_a}{k_B T}\right) + S_1\left(B + \frac{C}{T}\right)\right] \tag{6.2}$$

The additional stress S_1, influencing the device property via the parameters α, B, and C is additive to the Arrhenius part in the exponential term, k_B and T are as defined above. In the case of multiple stressing and variation of parameters, the model can be extended to stresses S_1, S_2, S_3.... and parameters (B_1, C_1), (B_2, C_2), (B_3, C_3) etc. The Eyring model certainly is better dedicated to describe more complex degradation behavior. In the case that careful control of the experimental methods prevents additional stress factors S_1, S_2... and, if α is negligible, the Eyring model collapses into the Arrhenius model. For the analysis presented here, additional stress variables have been carefully prevented; all measurements have been performed under constant illumination and in the photovoltaic mode.

A third popular accelerated life test model is the inverse-power-model, which is frequently used for electronic or dielectric products (equation (6.3)).

$$k_{deg} = A \cdot V^{\gamma} \tag{6.3}$$

Here, V is the stress (typically applied voltage or current) and A and γ are product (component, material) specific parameters. Acceleration models of this type are more relevant for organic light emitting diodes, transistors or photodetectors operated under constant temperature stressed by different bias or current levels.

6.1.2.2 Selection of Monitored Parameters

The essential photovoltaic parameters are the photo-induced current density I_{SC}, the open circuit voltage V_{OC}, the fill factor ff and the maximum power point m_{pp}, representing the

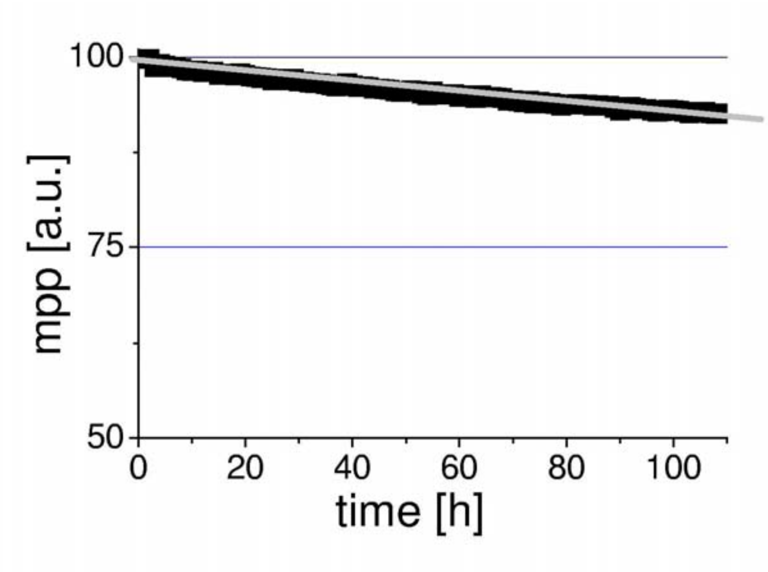

Figure 6.1: Transient behavior of m_{pp} versus time (full squares). The line is a fit according to equation (6.4).

power conversion efficiency. The temperature acceleration of the maximum power point m_{pp} is evaluated, as this is the most decisive parameter with respect to degradation of the whole device. The other parameters, like the serial and parallel resistivity, the fill factor and the photogenerated current will be discussed in the second section.

It is important to note that during the experiments no real life time is measured, but, only the change of a property of the device due to degradation over time. Subsequently this change has to be described by a mathematical model, and extrapolation will allow to predict the life time of the device [75, 76].

6.1.2.3 Determination of the Degradation Kinetics

Figure 6.1 shows a typical transient behavior of the m_{pp} of a reference device (process #1) over time, measured under illumination with approximate 1/3 sun and at 40 °C.

In order to determine a degradation constant k_{deg} from experimental data, a mathematical model for the time dependence has to be assumed. Both, a linear (equation (6.4)) and an exponential model (equation (6.5)) were applied to the experimental data. It can be seen, the linear model describe the data received significantly better.

$$m_{pp} = m_{pp}(0) * (1 - k_{deg} \cdot t) \tag{6.4}$$

$$m_{pp} = m_{pp}(0) * exp^{(-k_{deg} \cdot t)} \tag{6.5}$$

In order to calculate an acceleration factor, we have to describe the temperature dependence of the degradation constant. The Arrhenius type degradation model (equation (6.1)) is applied for evaluation of the temperature dependence. Please note that this is an assumption, which has to be justified by the quality of the model to describe the experimental data.

Four different temperatures were chosen as acceleration factors, ranging from $T = 40..95°C$. All devices were encapsulated between glass plates and illuminated by halo-

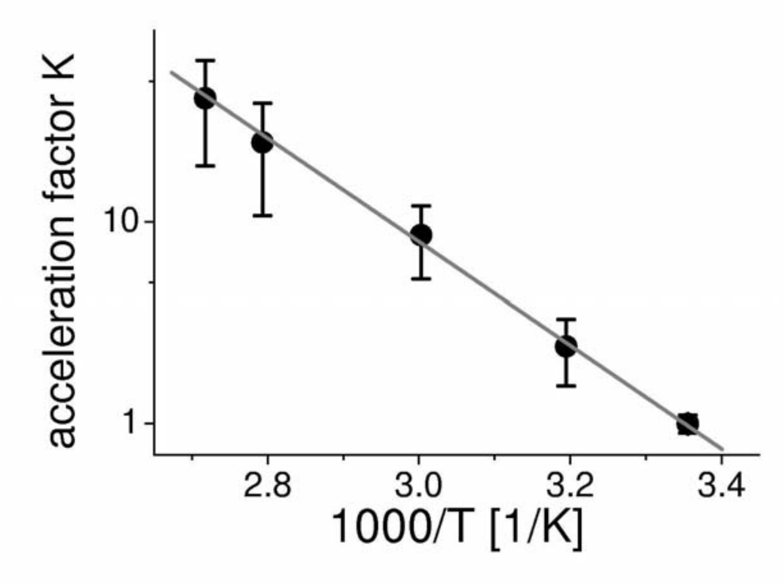

Figure 6.2: Temperature dependence of the acceleration factor K (full circles) and prediction of the Arrhenius model according to equation (6.6) with an activation energy of $220\,meV$ (line). The reference temperature is 298 K.

gen lamps, with approximate $30mWcm^{-2}$ illumination intensity. At least 16 devices were tested for each condition to allow statistical evaluation.

For each temperature a new set of devices entered the degradation. Devices were characterized before degradation under 1 sun to guarantee initial performance at an comparable level. The treatment was performed until m_{pp} dropped below 50 % of the initial m_{pp} value. For each device, m_{pp} was evaluated as depicted in Figure 6.1 and k_{deg} was determined according to equation (6.4). The acceleration factor K for the single temperatures was determined under the assumption of an Arrhenius model according to equation (6.6)

$$K = \frac{k_{deg}\left(T'\right)}{k_{deg}\left(T\right)} = exp\left[\frac{E_a}{k_B}\left(\frac{1}{T} - \frac{1}{T'}\right)\right] . \tag{6.6}$$

Figure 6.2 shows the acceleration factor K for the different temperatures. The excellent agreement of the experimental data to an Arrhenius dependence of the degradation constant justifies the applicability of this model. The slope of the Arrhenius plot represents the activation energy E_a for the accelerated degradation. An activation energy E_a of $E_a = 220 \pm 30\,meV$ is determined.

Degradation measurements at a constant temperature of $T = 85°C$ and under various illumination intensity were done. As the exact illumination intensity could not be measured for each single cell, the starting value of the short circuit current $I_{SC}(t = 0)$ is taken as the stress parameter. The short circuit current represents the illumination intensity, because the photogenerated current is proportional to the light intensity. Reference measurements for the cells were done to make sure all samples were starting from a comparable efficiency level. The degradation constant was evaluated for every sample according to equation (6.4).

Figure 6.3 shows the dependence of the degradation constant with the short circuit current. No correlation of the degradation constant K_{deg} with the I_{SC} can be detected. The

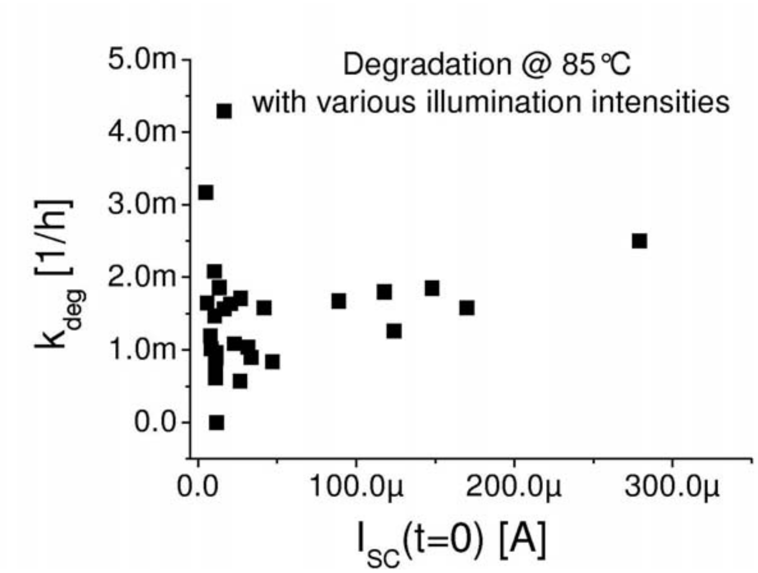

Figure 6.3: Illumination intensity dependence of the degradation constant k_{deg} (full squares). The illumination intensity is represented by the short circuit current density I_{SC}.

statistical variation is larger than any visible trend.

6.1.2.4 Discussion

ALT is a proper tool to predict lifetimes of organic solar cells. Ambient temperature has been proven as a powerful acceleration factor. For solar cells made by process#1, the evaluation of acceleration shows a 25 times faster degradation at $85°C$ compared to $25°C$. The acceleration of degradation by enhanced temperature can be described by an Arrhenius model, yielding an activation energy of $E_a = 190..250\,meV$.

With this acceleration factor the accelerated lifetime measurement can be evaluated to predict the lifetime of the samples at room temperature or at $50°C$, which is expected to be the temperature under constant illumination with 1 sun. Figure 6.4 shows the ALT measurement of a sample (process#1), measured at $85°C$. The time until the performance drops below the 50% level is about $2400h$. This corresponds to a lifetime of about $58000h$ at room-temperature ($25°C$) and of nearly $12000h$ at $50°C$. With expected 2000h of sun shine per year (Germany - upper limit) [60], this corresponds to a lifetime of about 6 years.

Morphology changes of the blend or of single components as well as the formation of electronical defects (e.g. formation of shunts) may be responsible for the temperature acceleration. However, the origin for the temperature acceleration is not fully understood and will be further discussed in the next section.

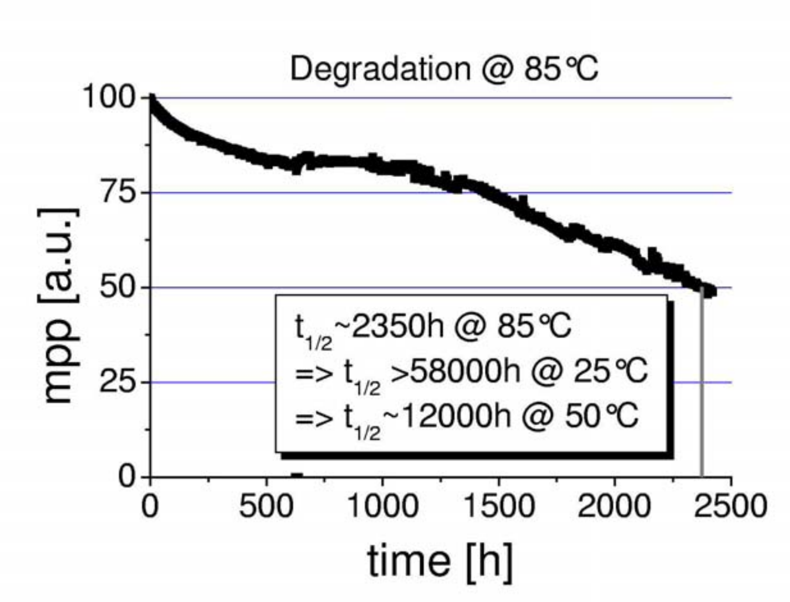

Figure 6.4: m_{pp} vs. time for an ALT measurement at $85°C$. The predicted lifetime (see inset) at 25°C and 50°C is calculated by using the acceleration constant $K = exp\left[\frac{E_a}{k_B}\left(\frac{1}{T} - \frac{1}{T'}\right)\right]$ and the activation energy $E_a = 190..250meV$.

6.2 Degradation Mechanism

In this section the mechanism of degradation will be investigated in more details. The IV-curve is analyzed for samples in different states of degradation. The analysis will be done with the extended equivalent circuit.

For the degradation many mechanisms are possible. The following are discussed in more detail:

- the change of the organic material itself, e.g. due to oxidation
- oxidation of the electrode
- delamination of the electrode
- change of the morphology
- formation of shunts

These mechanisms are expected to show different fingerprints in the cell performance, which allows to differentiate between these mechanisms. The analysis is done for samples made by process#2.

6.2.1 Measurements and Results

A change of the organic material is expected to show up in the absorption spectra of the sample. With the oxidation, the conjugation length of the polymer is decreased and should therefore change the absorption. If it gets too short, the polymer is bleached. A change in the absorption is not visible for the samples investigated, if analyzed by the eye. Therefore a degradation of the material itself does not seem to be the reason for degradation of the samples, although it can not be ruled out completely and will be discussed later on.

The other degradation parameters can be analyzed in terms of electrical properties of the devices under test. In Figure 6.5, 6.6, 6.7, 6.8 and 6.9 the analysis of electrical parameters of the solar cells extracted from the current - voltage characteristics are shown, according to the IV-curve discussion (chapter 3.1) and the extended equivalent circuit (chapter 4.2). The IV-curves were measured during the degradation of samples kept at $85°C$ and under illumination with white light ($30mWcm^{-2}$).

The degradation analysis shows a change of the degradation mechanism after about $t_{change} \approx 1000h$. Nearly all parameters show a different behavior until t_{change} compared to times $t > t_{change}$. The m_{pp} and I_{SC} (Figure 6.5) are nearly constant until t_{change} and show a fast decrease for $t > t_{change}$. The parallel resistance is increasing within 20-30 hours and remains constant for the rest of the measurement, as seen in Figure 6.7(a). The series resistance shows a slight increase for times $t < t_{change}$ and is increasing fast for $t > t_{change}$ (Figure 6.7b). The open circuit voltage (Figure 6.6b) is decreasing in 20-30 hours and shows a slight decrease for the rest of the measurement. The fill factor (Figure 6.6a) shows an increase within 20-30 hours and a steady decrease for times $t < t_{change}$. For times $t > t_{change}$ the fill factor is decreasing faster. The diode parameter n and I_0 are constant for times $t < t_{change}$ and increase fast for time $t > t_{change}$ (Figure 6.9). The flat-band voltage V_{FB} and mobility-lifetime product $\mu\tau$ were measured under the solar simulator condition at $25°C$, interrupting the degradation measurement. The V_{FB} shows a large drop from the first to the second measurement and stays nearly constant for the rest of the measurement. The $\mu\tau$ - product stays nearly constant for times $t < t_{change}$ and is then decreasing.

6.2.2 Discussion

First the region of nearly constant m_{pp} for times smaller $t < t_{change}$ is discussed. The slight decrease of the m_{pp} is due to a steady decrease of the fill factor and the open-circuit voltage (Figure 6.6). The lowering of the fill factor can be either due to the resistances or due to the diode parameter, as discussed in chapter 5.3. The series resistance R_S is increasing, as shown in Figure 6.7(b). The parallel resistance is increasing in the first 20-30 hours, leading to an small increase of the fill factor and stays constant over the time for the rest of the degradation. Hence, the degradation is not due to the formation of shunts. The diode ideality n and the saturation current I_0 are not changing until t_{change} significantly. The morphology is not changed until t_{change}. Also the $\mu\tau$ - product is unchanged until t_{change}. Therefore the slight decrease of the fill factor can only be due to an increase of the series resistance. This could be explained by a change of the contact. Both, an oxidization or a delamination of the contact may lead to a decrease of the conductivity in forward direction and, thus, lead to a change of the work function of the electrode. This can be seen in the drop of the flat-band voltage. This lowering of V_{FB} also explains the temporal decrease of the V_{OC}. The decrease of the open circuit voltage at the beginning of the measurement is unclear, as this effect is faster, than the measurement periods of n, I_0, V_{FB} and the $\mu\tau$ - product.

For times $t < t_{change}$, a slight degradation of the solar cell can be seen (Figure 6.5). The

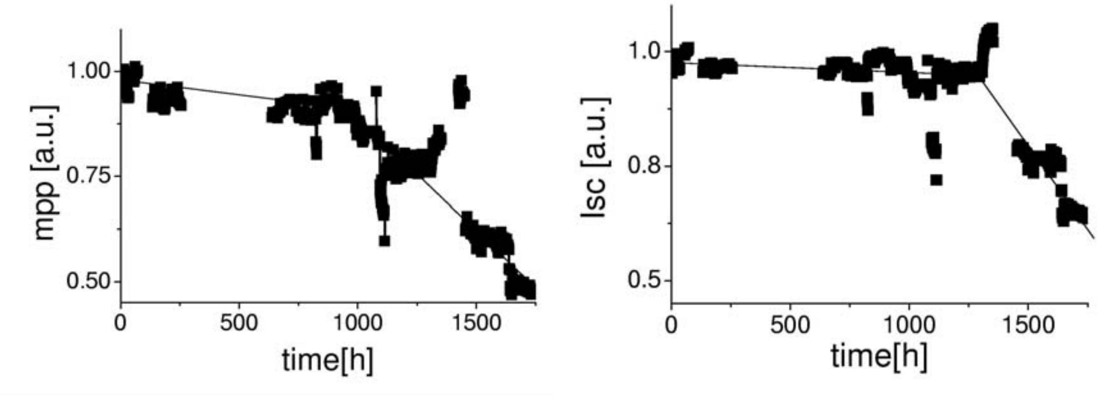

(a)

(b)

Figure 6.5: (a) The maximum power point and (b) the short circuit current vs. the time for samples, made by process#2. Given are the relative values, with respect to the starting values. Lines are drawn as a guide for the eye.

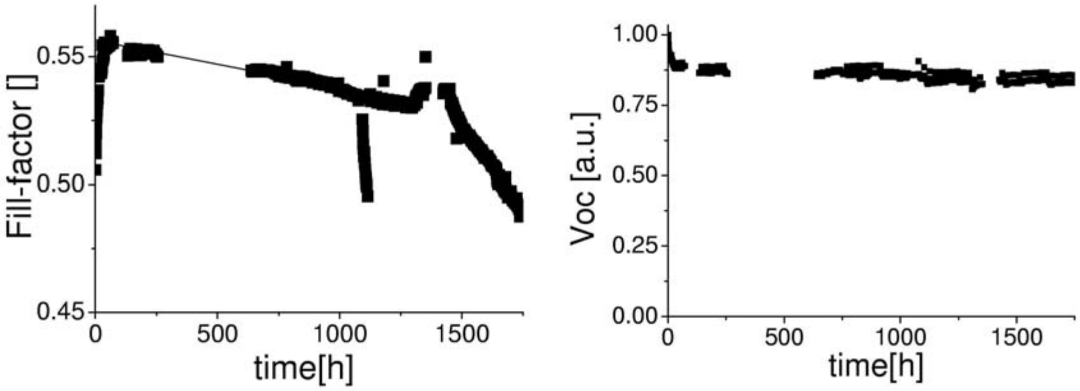

(a)

(b)

Figure 6.6: (a) The fill factor and (b) the open circuit voltage V_{OC} vs. the time. For the V_{OC} the relative values are given, with respect to the starting value. Line is drawn in (a) as a guide for the eye.

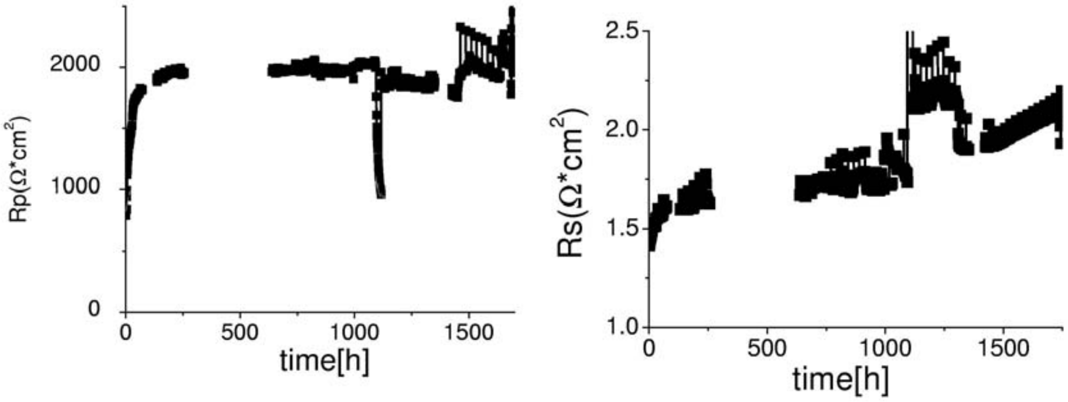

(a) (b)

Figure 6.7: (a) The parallel resistance and (b) the serial resistance vs. the time for samples, made by process#2.

origin of this degradation seems to be a change of one of the contacts, leading to an increase of the R_S with the time. Further tests were done with the variation of both contacts, in order to determine the failing contact and mechanism of contact failure, but no clear results could be obtained. If this change is due to oxidation or delamination and which of the two contacts is responsible for the degradation is unclear.

For times $t > t_{change}$, more parameters are changing in a larger scale. Only the open circuit voltage, the flat-band voltage and the parallel resistance stay unchanged with time. The fill factor and the short-circuit current are decreasing and therefore the m_{pp} is decreasing. This degradation does not seem to be due to the formation of shunts, because the R_P stays constant. The R_s is increasing faster than before.

The mechanism of this fast degradation is unclear. The morphology seems to be changed, because the diode parameters n and I_0 increase. This change of the diode can also have an influence on the transport of charge carriers, indicated by a lowering of the $\mu\tau$ - product and a rise of the series resistance.

The change of the diode is inducing the drop in the fill factor. The fill factor is also lowered by the increasing series resistance, which can be a hint of a deterioration of the electrodes. This degradation of one of the electrodes, could explain the decrease of the short circuit current, e.g. due to an increase of surface recombination. The rapid degradation could also be due to a degradation of the material itself, e.g. decomposition of the polymer.

To determine the degradation mechanism, additional measurements have to be be done: absorption and EQE on the degraded samples, chemical analysis, trap-spectroscopy, just to name a few of them.

The origin of the turn over of the slow to the more rapid degradation, with a change of the degradation mechanism at a time $t = t_{change}$ is unclear. Such change can be seen more often (e.g. Figure 6.4) and the origin of this turn over would be interesting therefore. It could be due to a failure of sealing, e.g. due to cracking of the glue under the elevated temperature with the time, but no measurements were done to prove this.

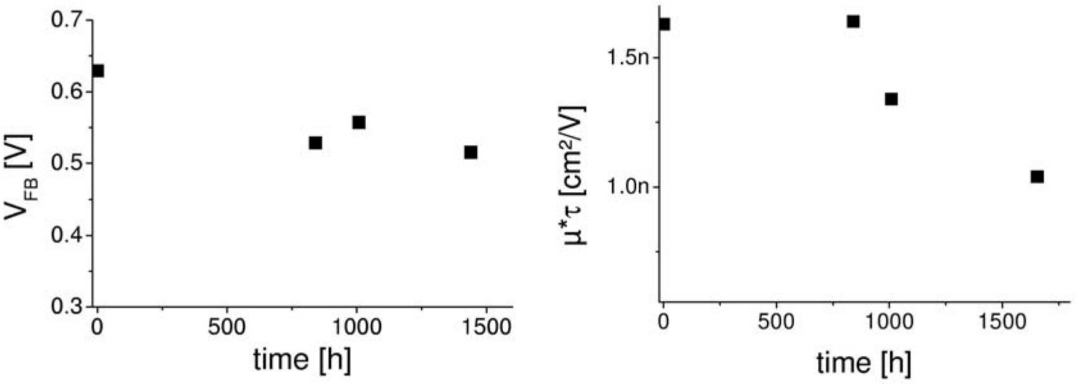

(a)

(b)

Figure 6.8: (a) The flat-band voltage V_{FB} and (b) the $\mu\tau$ - product vs. the time. The values are calculated according to chapter 4.2 and 5.1.1.3.

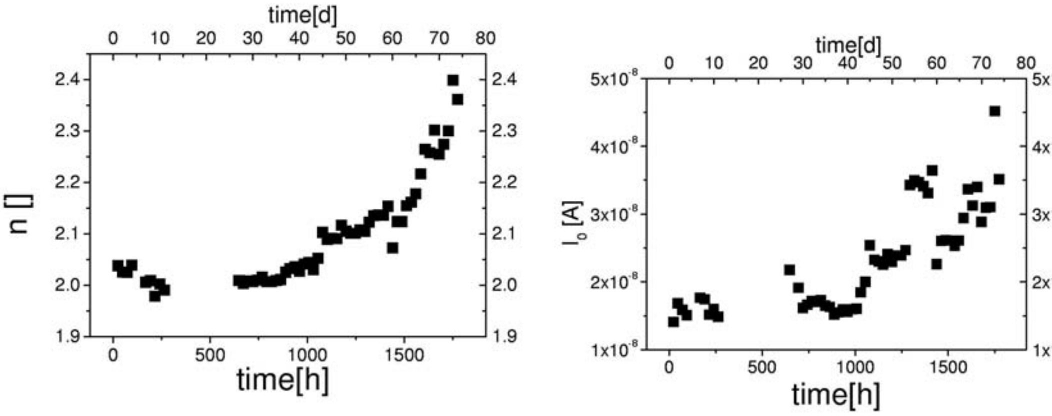

(a)

(b)

Figure 6.9: (a) The diode ideality and (b) the saturation current vs. the time for samples, calculated according to equation (4.4) of chapter 4.2.

6.3 Conclusion

In this chapter, the temperature accelerated lifetime analysis is proven to be a proper tool for predicting lifetimes of organic bulk heterojunction solar cells. The illumination intensity is not suitable as an acceleration factor for the lifetime testing of organic bulk heterojunction solar cells.

The degradation mechanism can be analyzed with the temperature accelerated lifetime analysis. Three degradation mechanism are evaluated. First, the degradation of contacts may cause a slow decrease of the fill factor. The internal flat-band voltage is lowered, causing a decrease of the open circuit voltage. These two effects lead to a slow decrease of the efficiency. After about 1000h the degradation mechanism changes toward a faster degradation. The mechanism of this fast degradation is unclear and more measurements have to be done in order to reveal the degradation mechanism.

Chapter 7

Conclusion and Outlook

7.1 Summary

In this thesis, the losses in the power conversion efficiency of organic bulk heterojunction solar cells are discussed. The power conversion efficiency is the product of three IV-characteristic parameters, such as short circuit current, open circuit voltage and fill factor, which are analyzed separately. Further, the degradation is analyzed with the temperature accelerated lifetime testing. These evaluations are done on one model material combination of a conjugated polymer and a fullerene as the electron donor and acceptor, respectively.

The efficiency and degradation analysis was done by using two models describing the bulk heterojunction. The first model is a microscopic description of the bulk heterojunction with the transport, Poisson, rate and the electron continuity equations. The second model is an extended equivalent circuit (macroscopic) model, where the standard 1-diode equation is extended with a field driven photo-current-source, as suggested by the microscopic model.

The efficiency parameters I_{SC}, V_{OC} and ff can be analyzed by different techniques. For each efficiency parameter suggestions for an improvement are done and tested.

The short circuit current I_{SC} summarizes the single particle conversion efficiencies of the photon to electron conversion. These conversion steps are the photon absorption and charge generation, the charge separation and the charge transportation and extraction. A set of measurements allows to distinguish between the efficiencies in the particular conversion steps and to detect relevant losses in the conversion efficiency.

The optical measurements show absorption of the substrate and the interfacial layer of about 10%. The substrate reflects about 10% of the incident light. The transport measurements indicate, that the charge transport takes place without losses for thicknesses of the active layer up to the drift length $d_{drift} \approx 0.4..0.5\mu m.$ The EQE and IQE measurements prove this loss free charge transportation and extraction. The latter measurements also show a loss in the charge separation for charges generated at the fullerene.

The loss in the charge separation is interpreted, to be due to too large domains of the fullerene in respect to the exciton diffusion length. Charges generated on the fullerene do not always reach the separating interface to the polymer, but recombine before. With a change in the morphology, the fullerene domain size can be reduced and the loss in the charge separation is reduced. Further improvements should be possible by introducing an anti-reflection coating or by exchanging the used material combination by polymers with a absorption shifted more to longer wavelengths, in order to absorb more effectively in the red part of the solar spectrum.

Losses in the open circuit voltage were satisfyingly explained by the macroscopic model. The photogenerated carriers are field driven, therefore the field dependence of the photocurrent has to be taken into account. The driving field is the sum of the internal field and the applied voltage. The internal field is limited by the splitting of the quasi-Fermi-levels and can be reduced by non-ohmic contacts and carrier accumulation.

The IV-characteristics of the organic bulk heterojunction solar cells are analyzed with this model and the model parameters are extracted. Simulations are done, with changing pairs of these model parameters, to predict the dependence of the open circuit voltage of these parameters. The most pronounced dependence is observed for the diode parameter ideality n and saturation current density I_0. The saturation current density could be influenced by the doping of the polymer solution. Also the dependence of the open circuit voltage with the saturation current density was observed, which supports the extended equivalent circuit model. The total efficiency is not improved by this variation of the doping level. Both the ideality n and the saturation current density I_0 can be changed by a modification in the morphology. With this change, the open circuit voltage can be increased. The predicted dependence of the open circuit voltage with the diode parameters, by the macroscopic model, is verified.

The fill factor was analyzed within the macroscopic model. The mostly limiting parameter for the bulk-heterojunction solar cells, investigated in this thesis, is the shunt resistance. Further analysis of the shunt resistance shows, that the shunt resistance under illumination is a photoconduction of carriers on one material from one electrode to the other, called photoshunt. This photoshunt is due to a partly failure of one of the electrodes, most probably the metal electrode. With the insertion of a hole blocking layer in between the bulk heterojunction and the metal electrode, the shunt resistance under illumination and the fill factor were improved.

With these measurements and evaluation, based on the extended equivalent circuit, the limiting parameters in the power conversion efficiency could be determined. Experiments, done for reducing the limitations, which are due to the processing, were successful and led to a power conversion efficiency of 5% under simulated white light illumination.

The accelerated lifetime analysis is evaluated for the bulk heterojunction solar cells. The ambient temperature was found to accelerate the degradation of bulk heterojunction very effectively. The acceleration factor follows the Arrhenius-law with an activation energy of $220meV$. The illumination intensity is no stress factor. The predicted lifetime of the bulk heterojunction solar cells is estimated to be 50000h at room-temperature or 12000h at 50°C.

Three different degradation mechanisms are detected. A fast degradation of the open circuit voltage within the first couple of 10h is of unclear origin. This degradation is compensated by an increase of the fill factor in the same time period.

For the first approximate $\frac{2}{3}$ of the degradation, a slight decrease of the fill factor and the open circuit voltage can be seen. This is interpreted as a degradation of the contact, either due to oxidation or delamination.

For the rest of the degradation a faster decrease of the fill factor and photogenerated current was found. The mechanism of this fast degradation is unclear. It may be due to a change of the morphology, however the degradation of one of the used electrodes and materials is possible, too.

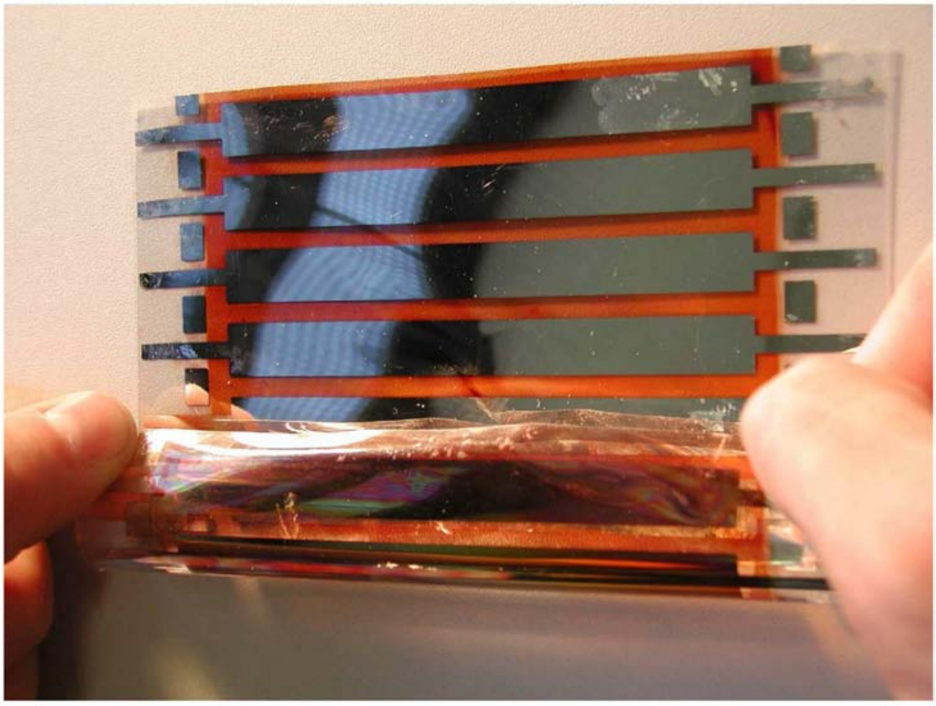

Figure 7.1: Example of a large, flexible module. Picture taken from [77].

7.2 Outlook

The efficiency of the organic bulk heterojunction solar cells can be increased to 5% and the predicted lifetime of these cells is larger than 6 years. The next steps would be to transfer this to a flexible, large area device (Figure 7.1), produced by a cheap process. The up-scaling will cause limitations due to the series resistance, which will increase as the feed-resistance will increase. Also the shunt may become a larger problem, when the parallel resistance in the dark is decreasing due to film inhomogeneities. There will be a loss due to the ratio of used area to the total area of the substrate.

This may lead to a drop from the 5% to a lower value. As this 5% is an aim for commercializing the organic solar cells, such value of the efficiency in the module is at least needed and therefore the efficiency has to be increased.

For the next efficiency enhancement there are two possibilities. With this material combination only the fill factor and the open circuit voltage may be increased a bit. For an increase of the photocurrent or a significant increase of the open circuit voltage other material combinations have to be used.

Bibliography

[1] D.M. Chapin, C.S. Fuller, and G.L Pearson. *J. Appl. Phys.*, 25:676, 1954.

[2] M.B. Prince. *J. Appl. Phys*, 26:534, 1955.

[3] H. Shirakawa, E.J. Louis, A.G. MacDiarmid, and A.J. Heeger. *J. Chem. Soc. Chem. Com.*, 16:578, 1977.

[4] M. Knupfer. *Appl. Phys. A*, 77:623, 2003.

[5] T. Stubinger and W Brütting. *J. Appl. Phys.*, 90:3632, 2001.

[6] H.R. Kerp, H. Donker, R.B.M. Koehorst, T.J. Schaafsma, and E.E. Van Faassen. *Chem. Phys. Lett.*, 298:302, 1998.

[7] A. Haugeneder, M. Neges, C. Kallinger, W. Spirkel, U. Lemmer, J. Feldmann, U. Scherf, E. Harth, A. Gugel, and K. Mullen. *Phys. Rev. B*, 59:15346, 1999.

[8] N.S. Sariciftci, L. Smilowitz, A.J. Heeger, and F. Wudl. *Science*, 258:1474, 1992.

[9] C.J. Brabec, G. Zerza, G. Cerullo, S. De Silvestri, S. Luzatti, J.C. Hummelen, and N.S. Sariciftci. *Chem. Phys. Lett.*, 340:232, 2001.

[10] S. E. Shaheen, C. J. Brabec, N. S. Sariciftci, F. Padinger, T. Fromherz, and J. C. Hummelen. *Appl. Phys. Lett.*, 78:841, 2001.

[11] T. Munters, T. Martens, L. Goris, V. Vrindts, J. Manca, L. Lutsen, W. De Ceuninck, D. Vanderzande, L. De Schepper, J. Gelan, N. S. Sariciftci, and C. J. Brabec. *Thin Solid Films*, 403-404:247, 2002.

[12] H.J. Snaith, A.C. Arias, A.C. Morteani, and R.H. Friend. *Nano Lett.*, 2:1353, 2002.

[13] M. Liess, S. Jeglinski, Z.V. Verdeny, M. Ozaki, K. Yoshino, Y. Ding, and T. Barton. *Phys. Rev. B*, 56:15712, 1997.

[14] P.A. Brühwiler, A.J. Maxwell, A. Nilsson, N. Martensson, and O. Gunnarsson. *Phys. Rev. B*, 48:18296, 1993.

[15] I. Montanari, A.F. Nogueira, J. Nelson, J.R. Durrant, J. Winder, M.A. Loi, N.S. Sariciftci, and C.J. Brabec. *Appl. Phys. Lett.*, 81:3001, 2002.

[16] A.F. Nogueira, I. Montanari, J. Nelson, J.R. Durrant, C. Winder, N.S. Sariciftci, and C.J. Brabec. *Appl. Phys. Lett.*, 81:3001, 2002.

[17] R. Pacios, J. Nelson, J.R. Durrant, D.D.C. Bradley, M. Westerling, R. Österbacke, and C.J. Brabec. *Proc. SPIE*, 5215:264, 2004.

[18] R. N. Hall. *Phys. Rev.*, 87:387, 1952.

[19] W. Shockley and W. T. Read. *Phys. Rev.*, 87:835, 1952.

[20] V.D. Mihailetchi, P.W.M. Blom, J.C. Hummelen, and M.T. Rispens. *J. Appl. Phys.*, 94:6849, 2003.

[21] S. Spiekermann, G. Smestad, J. Kowalik, L. M. Tolbert, and M. Gratzel. *Synth. Met.*, 121:1603, 2001.

[22] Z. Zhijing, R. G. Reddy, and P. R. Taylor (eds.). *Fundamentals of Advanced Materials for Energy Conversion. Proceedings*, page 33, 2002.

[23] H. Frohne, S. Shaheen, J.C. Brabec, D.C. Muller, N.S. Sariciftci, and K. Meerholz. *Chem. Phys. Chem.*, 9:795, 2002.

[24] L. He, S. Yijian, and Y. Yang. *Adv. Funct. Mater.*, 11:420, 2001.

[25] K. Tada, K. Hosoda, M. Hirohata, T. Kawai, M. Onoda, M. Teraguchi, T. Masuda, A.A. Zakhidov, and K. Yoshino. *Synth. Met.*, 85:1305, 1997.

[26] Y. Kim, S. Cook, S.A. Choulis, J. Nelson, J.R. Durrant, and D.D.C. Bradley. *SCell - virtual Presentation*, 2004. www.todowebextremadura.com/abstractscell2004/112.pdf.

[27] D. Schmeisser. *Synth. Met.*, 138:135, 2003.

[28] M. Onoda, K. Tada, A.A. Zakhidov, and K. Yoshino. *Thin Solid Films*, 331:76, 1998.

[29] H. Sirringhaus, P. J. Brown, R. H. Friend, M. M. Nielsen, K. Bechaard, B. M. W. Langeveld-Voss, A. J. H. Spiering, R. A. J. Janssen, E. W. Meijer, P. Herwig, and D. M. de Leeuw. *Nature*, 401:685, 1999.

[30] A. Ullmann, J. Ficker, W. Fix, H. Rost, McCulloch; I., M. Giles, G.E. ed. Jabbour, and N.S. Sariciftci. *Mater. Res. Soc. Symposium Proc.*, 665, 2002.

[31] R. Lazzaroni, M. Logdlund, S. Stafström, and W.R. Salaneck. *J. Chem. Phys.*, 93:4433, 1990.

[32] V.M. Aroutiounian and H. Tributsch. *Proc. SPIE*, 4465:43, 2002.

[33] V.D. Mihailetchi, P.W.M. Blom, J.C. Hummelen, and M.T. Rispens. *J. Appl. Phys.*, 94:6849, 2003.

[34] J.K.J. van Duren, V.D. Mihailetchi, P.W.M. Blom, and T. van Woudenbergh. *J. Appl. Phys.*, 94:4477, 2003.

[35] V.D Mihailetchi, J.K.J. van Duren, P.W.M. Blom, J. C. Hummelen, R. A. J. Janssen, J. M. Kroon, M. T. Rispens, W. J. H. Verhees, and M. M. Wienk. *Adv. Funct. Mater.*, 13:43, 2003.

[36] M. Cha, N.S. Sariciftci, A.J. Heeger, J.C. Hummelen, and F. Wudl. *Proc. of the SPIE*, 2530:205, 1995.

[37] K. Tada, R. Hidayat, M. Hirohata, T. Kawai, Lee. S.B., I.U. Bakhadirov, A.A. Zakhidov, and K. Yoshino. *Synth. Met.*, 85:1349, 1997.

[38] S. Hotta, S.D.D.V. Rughooputh, and A.J. Heeger. *Synth. Met*, 22:79, 1987.

[39] A.J. Heeger. *Trends Polym. Sci*, 3:39, 1995.

[40] A. Aharony and D. Stauffer. *Introduction to Percolation Theory*. Taylor and Francis, London, 1993.

[41] R. Pacios, J. Nelson, Bradley. D.C., and C.J. Brabec. *Appl. Phys. Lett.*, 83:4764, 2003.

[42] D.J. Milliron, I.G. Hill, C. Shen, A. Kahn, and J. Schwartz. *J. Appl. Phys.*, 87:572, 200ß.

[43] H. Frohne, D.C. Muller, N. Reckefuss, P. Rudati, and K. Meerholz. *Proc. of the SPIE*, 4800:172, 2003.

[44] D Pestotnik. Influence of processing parameters on performance of polymer solar cells. *BSc thesis, Hogeschool van Utrecht*, 2002.

[45] P. Schilinsky, C. Waldauf, J. Hauch, and C.J. Brabec. *J. Appl. Phys.*, 95:2816, 2004.

[46] C. Waldauf, P. Schilinsky, J. Hauch, and C.J. Brabec. *Thin Solid Films*, 451-452:503, 2003.

[47] C. Brabec, J. Hauch, P. Schilinsky, and C. Waldauf. *Appl. Phys. Lett.*, to be bublished, 2004.

[48] S.M. Sze. *Physics of Semiconductor Devices*. Wiley, New York, 1981.

[49] C Waldauf. Requirements for materials in organic bulk heterojunction solar cells. *PhD thesis, University of Oldenburg*.

[50] R. S. Crandall, K. Sadlon, J. Kalina, A. E. Delahoy, A. ed. Madan, M. J. Thompson, P. C. Taylor, Y. Hamakawa, and P. G. LeComber. *Amorphous Silicon Technology-1989 Symposium*, page 423, 1989.

[51] J. Merten, J. M. Asensi, C. Voz, A. V. Shah, R. Platz, and J. Andreu. *IEEE Trans. Electr. Dev.*, 45:423, 1998.

[52] P. Schilinsky, C. Waldauf, and C. Brabec. *Appl. Phys. Lett.*, 81:3885, 2002.

[53] J Nelson. *Current Opinion in Solid State and Materials Science*, 6:87, 2002.

[54] T. Martens, J. D'Haen, T. Munters, L. Goris, Z. Beelen, J. Manca, M. D'Olieslaeger, D. Vanderzande, L. De Schepper, and R. Andriessen. *Mater. Res. Soc. Symposium - Proceedings*, 725:169–175, 2002.

[55] I. Montanari, A. F. Nogueira, J. Nelson, J. R. Durrant, C. Winder, M. A. Loi, N. S. Sariciftci, and C. Brabec. *Appl. Phys. Lett.*, 2002.

[56] P Schilinsky, I. Riedel, C. Waldauf, V. Dyakonov, and C. Brabec. *Appl. Phys. Lett.*, 2004. submitted.

[57] P. Schilinsky, C. Waldauf, J. Hauch, and C.J. Brabec. *Thin Solid Films*, 451:105, 2004.

[58] P.W.M. Blom, M.J.M. de Jong, and M.G. van Munster. *Phys. Rev.B*, 55:656, 1997.

[59] W. van Roosbroek and W. Shockley. *Phys. Rev.*, 94:1558, 1954.

[60] P Würfel. *Physik der Solarzellen.* Spektrum, Hdg, 1995.

[61] P.M.W. Blom, M.J.M. de Jong, and J.J.M. Vleggaar. *Appl. Phys. Lett.*, 68:3308, 1996.

[62] P.M.W. Blom, M.J.M. de Jong, and S Breedijk. *Appl. Phys. Lett.*, 71:930, 1997.

[63] I. Riedel. *PhD thesis, University of Oldenburg*, 2004.

[64] M Hoheisel and W Fuhs. *Phil. Mag.*, 57:411, 1988.

[65] J.C. Balland, J.P. Zielinger, C. Noguet, and M. Tapiero. *J. Phys. D.*, 19:57, 1986.

[66] H. Wieczorek and W. Fuhs. *Phys. Stat. Sol. A*, 114:413, 1989.

[67] A. F. Nogueira, I. Montanari, J. Nelson, J. R. Durrant, C. Winder, N. S. Sariciftci, and C. Brabec. *J. Phys. Chem. B*, 107:1567, 2003.

[68] J. Nelson. *Phys. Rev. B*, 67:155209, 2003.

[69] D. Poplavskyy and J. Nelson. *J. Appl. Phys.*, 93:341, 2003.

[70] H. Scher, M. F. Shlesinger, and J. T. Bendler. *Phys. Today*, 44:26, 1991.

[71] R. L. Lidberg, K. Goswami, M. R. Lovato, R. Venkatasubramanian, and W. H. Engelmann. *Proc. SPIE*, 2397:633, 1995.

[72] D. M. de Leeuw and E. J. Lous. *Synth. Met.*, 65:45, 1994.

[73] M.V. Lauritzen, S. Holdcroft, J.R. ed Reynolds, A.K. Jen, M.F. Rubner, L.Y. Chiang, and L.R. Dalton. *Proc. Mater. Res. Soc.*, 488:341, 1998.

[74] S. Schuller, P. Schilinsky, J. Hauch, and C.J. Brabec. *Appl. Phys. A*, 79:37, 2004.

[75] D. Blaese. *Methodische Ansaetze zur Abschätzung der Lebensdauer bei Kunststoffbauteilen bei komplexer Belastung.* Shaker, Aachen, 2000.

[76] W. Nelson. *Accelerated Testing: Statistical Models, Test Plans and Data Analyses.* Wiley, New York, 1990.

[77] *Siemens Press Release*, 2004.

Curriculum Vitae

Pavel Schilinsky, geboren am 28.05.1974 in Hamburg
Staatsangehörigkeit: deutsch

Schulbildung

1981-1985	Grundschule an der Lessingstraße, Bremen
1985-1987	Orientierungsstufe an der Brokstaße, Bremen
1987-1991	Schulzentrum an der Hamburgerstraße, Bremen
1991-1994	Gymnasium an der Kurt-Schumacher-Allee, Bremen

Zivildienst

1994-1995	Wiedereingliederungshilfe von psychisch erkrankten Menschen, Werkstatt Bremen

Studium

1995-1997	Physik (Diplom) an der Universität Bremen; Vordiplom
1997-2001	Physik (Diplom) an der Universiät Oldenburg, Diplom

Promotion

seit 2001	Promotion an der Universität Oldenburg bei Vladimir Dyakonov Thema: Loss Analysis of the Power Conversion Efficiency of Organic Bulk Heterojunction Solar Cells

Danksagung / Acknowledgement

Ich möchte mich an dieser Stelle bei all denjenigen bedanken, die maßgeblich zum Gelingen der Arbeit beigetragen haben. Mein Dank gilt:

- Christoph Brabec, Vladimir Dyakonov und Jürgen Parisi, für die Ermöglichung der Arbeit und die intensive Betreuung
- Christoph Waldauf für viele interessante und leidenschaftliche Diskussionen, die wir selten zum Abschluß bringen konnten und für vieles mehr
- Mauro Morana für vieles, unter anderem die moralische Unterstützung bei den Diskussionen mit Christoph Waldauf
- Jens Hauch für die vielfältige Unterstützung und die Diskussionen
- den besten Azubis Julia Wirsing und Markus Biele für die praktische Unterstützung, wie dem Schneiden von über 1000 Glassubstraten
- Ingo Riedel, Martin Knipper und Michael Pientka für die gute Zusammenarbeit, langen Diskussionen und manches mehr
- Roberto Pacios für die fruchtbaren Diskussionen, Anregungen und für die Hoffnung auf den Kellnerjob in Jamaika
- Arkadius Gronek für die gute Umsetzung der Meßprogramme und zusammen mit Beata für die leckere Einführung in die polnische Küche
- Dusan Pestotnik für diverse Hilfen und die slowenischen Barbeques am See
- den Diplomanden, Praktikanten und Werkstudenten (u.a. Stephan Schuller, Johannes Kiesel, Christian Martin, Thomas Höfner, Chen Xu, Pia Krieger, Thomas Tscherner, Antonio Nevado, Antonio Castellano) für die vielen großen und kleinen Hilfen und Diskussionen
- allen oben genannten für die einzigartige Arbeitsatmosphäre, die vielen Kuchen und für die diversen Aktivitäten außerhalb der Arbeit, wie Bergkirchweih, Kneipe oder Wanderungen. Es hat echt Spaß gemacht, mit Euch zusammen zu arbeiten
- der Siemens AG für die finanzielle Unterstützung
- nicht zuletzt meinen Eltern, Schwestern, Freunden und meiner Freundin Melanie für die große Unterstützung

Erklärungen gemäß §10 der Promotionsordnung

Hiermit erkläre ich, daß ich diese Arbeit selbständig verfaßt und nur die angegebenen Hilfsmittel benutzt habe.

Erlangen,

(Pavel Schilinsky)

Hiermit erkläre ich, daß die vorliegende Dissertation weder in ihrer Gesamtheit noch in Teilen einer anderen wissenschaftlichen Hochschule zur Begutachtung in einem Promotionsverfahren vorliegt oder vorgelegen hat.

Erlangen,

(Pavel Schilinsky)

Hiermit erkläre ich, daß die vorliegende Arbeit bereits in Teilen veröffentlicht wurde

Erlangen,

(Pavel Schilinsky)

Publikationsliste

- Schilinsky, P. and Waldauf, C. and Brabec, C., RECOMBINATION AND LOSS ANALYSIS IN POLYTHIOPHENE BASED BULK HETEROJUNCTION PHOTODETECTORS, Applied Physics Letters, 81:3885, **2002**
- S. Schuller, P. Schilinsky, J. Hauch, C.J. Brabec, DETERMINATION OF THE DEGRADATION CONSTANT OF BULK HETEROJUNCTION SOLAR CELLS BY ACCELERATED LIFETIME MEASUREMENTS, Appl. Phys. A, 79:37, **2004**
- P. Schilinsky, C. Waldauf, J. Hauch, C.J. Brabec, SIMULATION OF LIGHT INTENSITY DEPENDENT CURRENT CHARACTERISTICS, J. Appl. Phys., 95:2816, **2004**
- P. Schilinsky, C. Waldauf, J. Hauch, C.J. Brabec, POLYMER PHOTOVOLTAIC DETECTORS: PROGRESS AND RECENT DEVELOPMENT, Thin Solid Films,451:105, **2004**
- T. Erb, U. Zhokhavets, G. Gobsch, S. Ralevy, B. Strühn, P. Schilinsky, C. Waldauf, C.J. Brabec, , Adv. Funct. Mater. (submitted), **2004**
- C. Waldauf, P. Schilinsky, J. Hauch, C.J. Brabec, MATERIAL & DEVCIE CONCEPTS FOR ORANIC PHOTOVOLTAICS: TOWARDS COMPETIVE EFFICIENCIES, Thin Solid Films, 451-452:503, **2004**
- P. Schilinsky, I. Riedel, C. Waldauf, V. Dyakonov, C.J. Brabec, HIGHLY EFFICIENT GENERATION AND RECOMBINATION FREE TRANSPORTATION OF CHARGE CARRIERS IN POLYMER-FULLERENE BULK HETEROJUNCTION DEVICES, (in preparation), **2004**